2016

Bridging The Materials Gap In Catalysis: Reactivity Studies Of Nanostructured Titania

David Alan Bennett
University of Pennsylvania, dbe@seas.upenn.edu

Bridging The Materials Gap In Catalysis: Reactivity Studies Of Nanostructured Titania

Abstract
ABSTRACT

BRIDGING THE MATERIALS GAP IN CATALYSIS:

REACTIVITY STUDIES OF NANOSTRUCTURED TITANIA

David A. Bennett

John M. Vohs

Surface science studies of defect-free, single-crystal model catalysts have provided vital knowledge in the form of structure-activity relationships and elementary reaction mechanisms. However, there is some difficultly in extending this understanding to more complex systems, since these model catalysts typically lack the range of features that occur on the high surface area catalysts used in industry. This project seeks to bridge the gap between these two classes of materials by studying thin films of well-defined TiO2 nanocrystals with tunable size and morphology using traditional surface science techniques. This enables the controlled introduction of features lacking in single-crystal model catalysts, allowing for the formulation of more complex structure-activity relationships. The thermal- and photocatalytic reactions of methanol to produce methane, formaldehyde, dimethyl ether, and methyl formate on these TiO2 nanoparticles were investigated using temperature programmed desorption in ultra high vacuum. Results show clear effects of nanocrystal size and shape on the activity and selectivity of these reactions. This demonstrates the value of studying nanostructured metal-oxide catalysts to better understand the relationship between fundamental catalytic knowledge and the behavior of complex heterogeneous catalysts.

Degree Type
Dissertation

Degree Name
Doctor of Philosophy (PhD)

Graduate Group
Chemical and Biomolecular Engineering

First Advisor
John M. Vohs

Keywords
anatase, catalysis, surface science, titanium dioxide

BRIDGING THE MATERIALS GAP IN CATALYSIS:

REACTIVITY STUDIES OF NANOSTRUCTURED TITANIA

David A. Bennett

A DISSERTATION

in

Chemical and Biomolecular Engineering

Presented to the Faculties of the University of Pennsylvania

in

Partial Fulfillment of the Requirements for the

Degree of Doctor of Philosophy

2016

Supervisor of Dissertation

_____

Dr. John M. Vohs, Professor, Chemical and Biomolecular Engineering

Graduate Group Chairperson

_____

Dr. John C. Crocker, Professor, Chemical and Biomolecular Engineering

Dissertation Committee

Raymond J. Gorte, Professor, CBE

Talid R. Sinno, Professor, CBE

Christopher B. Murray, Professor, Chemistry

ACKNOWLEDGEMENTS

First and foremost, I want to thank my thesis advisor, John Vohs, for the guidance, advice, and patience he has shown me throughout the past five years. It goes without saying this project owes a large part of its success to his expertise and judgement. But beyond that, the balance he struck between mentorship and independence was exactly what I needed to develop as a scientist. I hope to learn from this example. I am also indebted to my collaborators, Matteo Cargnello, Thomas Gordon, and Benjamin Diroll, for providing the materials used in these studies. Without their proficiency in synthesis of nanostructured materials, this project would not have been possible. I also need to thank my co-workers in the Vohs and Gorte labs, in particular Eddie Martono and Jesse McManus for teaching me all about surface science. Lastly, I am extremely grateful for the support I have had from my family and from all the friends I have made in Philadelphia, in the chemical engineering department and elsewhere at Penn, at my church, and on our (seven-time champion) ultimate frisbee team.

ABSTRACT

BRIDGING THE MATERIALS GAP IN CATALYSIS:

REACTIVITY STUDIES OF NANOSTRUCTURED TITANIA

David A. Bennett

John M. Vohs

Surface science studies of defect-free, single-crystal model catalysts have provided vital knowledge in the form of structure-activity relationships and elementary reaction mechanisms. However, there is some difficultly in extending this understanding to more complex systems, since these model catalysts typically lack the range of features that occur on the high surface area catalysts used in industry. This project seeks to bridge the gap between these two classes of materials by studying thin films of well-defined TiO_2 nanocrystals with tunable size and morphology using traditional surface science techniques. This enables the controlled introduction of features lacking in single-crystal model catalysts, allowing for the formulation of more complex structure-activity relationships. The thermal- and photocatalytic reactions of methanol to produce methane, formaldehyde, dimethyl ether, and methyl formate on these TiO_2 nanoparticles were investigated using temperature programmed desorption in ultra high vacuum. Results show clear effects of nanocrystal size and shape on the activity and selectivity of these reactions. This demonstrates the value of studying nanostructured metal-oxide catalysts to better understand the relationship between fundamental catalytic knowledge and the behavior of complex heterogeneous catalysts.

TABLE OF CONTENTS

LIST OF TABLES

LIST OF FIGURES

Chapter 1. Introduction

Catalysis is vital to a productive and sustainable society, from the chemical and energy industries to environmental protection. Catalysts are involved in 90% of petrochemical processes [1] and 90% of commercially-produced chemicals involve catalysis at some point in the manufacturing process [2]. Metal-oxides typically serve as catalytic supports but are sometimes used as the active catalytic phase on their own [3], such as in the production of nearly 200 million tons of sulfuric acid per year (V_2O_5), the water-gas shift reaction for H_2 production (oxides of Cu, Zn, Al, Fe, and Cr), and the synthesis of methanol, which is of the chemical industry's most important feedstocks, from syngas (Cu/ZnO). CeO_2 is a key component in emissions control systems. These systems are designed to eliminate NO_x (which produces smog and acid rain), CO, and carcinogenic hydrocarbon particulates from exhaust streams. However, optimal conversion of these pollutants requires a very narrow range of fuel-to-air ratios. The role of CeO_2 as a reservoir of oxygen allows the emissions control to continue functioning in a wider range of conditions. TiO_2, a photocatalyst, can oxidize organic molecules when exposed to UV light [4]. This property has uses in environmental applications as diverse as self-cleaning windows, wastewater treatment, destruction of volatile organic compounds, hazardous waste remediation, dye-sensitized solar cells, and hydrogen production from photocatalytic water splitting.

Despite its great importance, catalysis was rarely understood on a mechanistic level at first. For instance, the Haber-Bosch process for ammonia production was

developed in the early 20th century, with BASF beginning the first production-scale process in 1913. Yet despite its wide use for the better part of a century, it was not until Gerhard Ertl's investigations in the 1980s that this vital process was understood at a mechanistic level. This lack of understanding was a major hindrance to the development of new catalysts.

The surface science approach to heterogenous catalysis revolutionized the field. These experiments use idealized conditions, surfaces, and reagents. In practice, this means studying the reactions of simple reagents with well-defined chemistry over defect-free, single-crystal model catalysts in an ultra-high vacuum chamber. This allows for direct investigation into the interactions between reagents and catalysts using surface-sensitive spectroscopic techniques, which in turn enables the development of structure-activity relationships. These relationships are statements linking the catalytic activity of a certain surface to its chemical and physical structure.

One such structure-activity relationship is the discovery of the role of K promoters in the Haber-Bosch process. Ertl et al. [5] observed that the presence of K on a Fe(100) surface increased the adsorption energy of N_2. This effectively lowers the activation energy of N-N dissociation, which is the rate-limiting step in ammonia synthesis. Another structure-activity relationship, uncovered by Kim and Barteau [6], was that the etherification of methanol to produce dimethyl ether on single-crystal TiO_2 occurs only on Ti^{4+} cations with two coordination vacancies. This knowledge guides the development of more active and selective catalysts.

While the surface science approach has produced invaluable contributions to the field of catalysis, it still has limitations. One of its greatest strengths, the high level of control afforded by idealized materials and conditions, is also a major weakness: how applicable is the knowledge derived from such idealized conditions? These conditions are necessary since the development of structure-activity relationships depends on the ability to precisely control and accurately characterize the structure of catalyst. However, the catalysts used in industrial processes differ markedly from the defect-free, single-crystal model catalysts. In surface science terminology, industrial catalysts tend to be highly defective. In other words, these catalysts have a high density of irregularities, such as oxygen vacancies, under-coordinated cations, step-edges, etc. The disparity between these two classes of materials is referred to as the materials gap.

The materials gap is only a problem if significant catalytic activity is associated with these defect features. Unfortunately defect sites are often are often most active sites on the surface, or they may introduce additional reaction pathways. For instance, a study of CO oxidation on Pt nanoparticles in solution by Mayrhofer et al. [7] observed that defects on the Pt surface are the active sites for water dissociation, which is a necessary step in the CO oxidation mechanism. The overall rate of CO_2 production was found to scale with the number of defects. As an example of unique reactivity at defect sites, a study by Kim and Barteau [6] suggested that methanol deoxygenation to methane occurs at oxygen vacancy sites. It is clear that surface science studies of single-crystal materials alone are insufficient to capture the full range of behavior of real-world catalysts.

The goal of this project is to bridge this materials gap using well-defined TiO_2 nanocrystals with tunable size and shape. This enables the controlled introduction of features not present in single-crystal materials, which opens the door for more complex structure-activity relationships. For instance, this project found that the activity and selectivity of the various reactions of methanol depend on the nanocrystal size and shape. These observations were only possible using a material with variable nanostructure, so they would not have been possible in a single-crystal study. Neither would they have been possible in a study using 'real-world' catalysts, for which structural characterization and control are difficult. It is the combination of structural complexity and control that allow the TiO_2 nanocrystals used in this project to bridge the materials gap.

TiO_2 is the prototypical photo-oxidation catalyst as well as having uses as a selective-oxidation catalyst and as a catalytic support. The activity of single-crystalline TiO_2 has been widely studied for both thermally- [8] and photochemically-driven reactions [9]. This makes TiO_2 the logical choice for attempting to bridge the metal-oxide materials gap. Additionally, TiO_2 lends itself to highly-precise and tunable nanocrystal synthesis. These nanocrystals are dispersed into thin films to make them compatible with traditional surface science techniques such as temperature programmed desorption and x-ray photoelectron spectroscopy. Methanol is able to undergo a wide array of conventional- and photo-reactions that TiO_2 is known to catalyze. The complex chemistry and simple structure of methanol make it an ideal probe molecule for surface science studies.

1.1 Thesis Outline

This dissertation includes two chapters aimed at providing a thorough background knowledge through which the rest of the thesis may be better understood. Chapter 2 reviews the current body of knowledge of reactivity of small oxygenates on various forms of TiO_2. It also contains a section describing the structure of the most important TiO_2 surfaces (section 2.1.2) and an overview of the basic principles of heterogeneous catalysis (section 2.3.1). 0 details the theory behind the various experimental techniques used in this project and the related equipment, with a brief explanation of the synthesis of the TiO_2 nanocrystals in section 3.2.1.

Chapter 4 and Chapter 5 present the two publications produced by the TiO_2 studies. The first features several sizes of nanocrystals with a common aspect ratio. The second introduces a second nanocrystal geometry and compares the methanol reactivity between the two. Chapter 6 is a publication from an earlier collaboration with a different catalyst material and different chemistry. While this study was not directly related to the TiO_2 project, it highlights the utility of using nanostructured catalysts to bridge the materials gap.

Chapter 2. Background

The majority of this thesis involves catalytic studies of TiO_2 nanocrystals. In order to bridge the gap between academic studies of model systems and the 'real life' catalysts used in industry, we must first understand the current state of knowledge in TiO_2 catalysis. TiO_2 is one of the most studied metal-oxide surfaces in heterogeneous catalysis [8]. This is in part to the due to the ease of producing and working with single crystals (especially for the rutile phase), and also to the wide range of applications of this material. TiO_2 is used as a support for metal and metal oxide catalysts, such as V_2O_5/TiO_2 which is used in selective catalytic reduction of NO_x and selective oxidation of methanol [10], and as a photocatalyst for decomposition of organic species and for water splitting, either on its own or with a co-catalyst such as Pt [9, 11]. It also has a range of uses outside the realm of catalysis, including in paint pigments, electrochromic, gas sensors, and as a potential gate material in next-generation MOSFETs [8]. This chapter provides a review of the structure and catalytic activity TiO_2 surfaces.

2.1 Structure of TiO_2

2.1.1 Bulk structure

TiO_2 is a lattice of Ti^{4+} cations and O^{2-} anions. In the bulk, each Ti cation is neighbored by six O anions forming a distorted octahedron with the Ti cation at the center. This cation is said to be sixfold coordinated. Each O anion in the bulk is threefold

coordinated. Within this framework, the lattice can take on several different arrangements which are realized macroscopically as distinct phases of TiO_2. The two most common phases (and also most relevant to this thesis) are rutile (R) and anatase (A). The structure of each is shown in Figure 2.1. Under standard conditions, rutile has slightly lower bulk energy, making it the thermodynamically-stable phase, although anatase is metastable below ~ 850 K [12]. This means that rutile single crystals are easier to produce and maintain, and consequently that vast majority of surface science work has focused on rutile [3, 8].

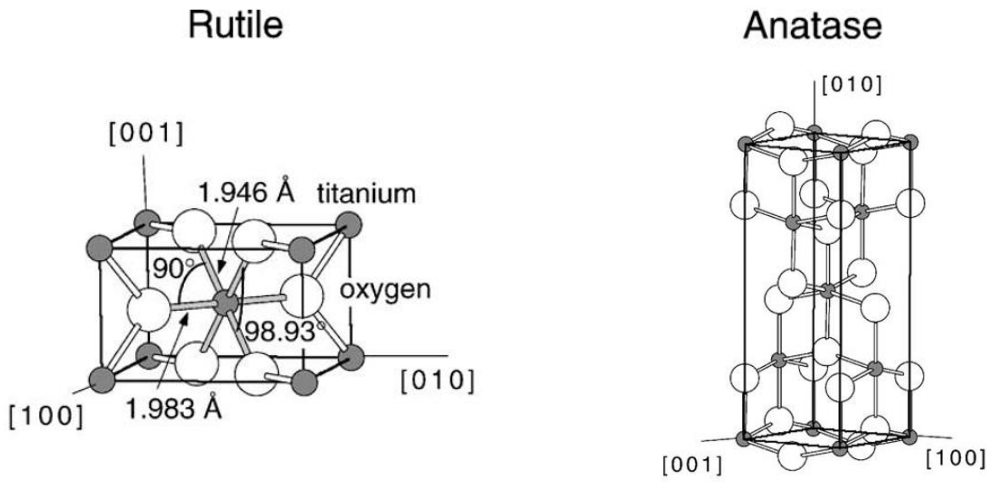

Figure 2.1 Rutile and anatase unit cells. In both structures, each (grey) Ti cation is surrouned by six (white) oxygen anions. Redrawn from [8].

When discussing nanocrystals, on the other hand, one must consider the surface energy in addition to the bulk energy, as a given volume of powder will have significantly higher surface area than the corresponding single crystal. In fact, anatase

tends to have slightly lower surface energy than rutile [8, 13]. For nanocrystals on the order of ~ 10 - 50 nm, the bulk energy penalty for anatase is roughly offset by the surface energy penalty for rutile [12]. Thus the anatase phase is often present in high-surface-area industrial TiO_2 catalysts [3]. This is one of several aspects of the materials gap as it applies to TiO_2 catalysis: fundamental studies of rutile single crystals are inadequate to fully describe the behavior of anatase or mixed-phase industrial catalysts.

Adsorbate chemistry is primarily a function of the surface structure, which will be discussed in section 2.1.2, and is more-or-less independent of bulk structure [14]. But the bulk structure still plays an important role in photocatalysis, since photon absorption generally occurs in the bulk [9]. For instance, rutile has a direct bandgap of 3.0 eV, while anatase has an indirect bandgap of 3.2 eV (with the transition to direct bandgap occurring near 4.0 eV) [9]. Other steps in the photocatalytic process (discussed in section 2.3.1) are also dependent on the bulk structure. Migration of photo-excited charge-carriers to the surface is also a bulk process. The dynamics and anisotropy of this process depend on the specific crystal structure [15, 16]. The degree of bulk crystallinity also influences the likelihood that the charge-carriers reach the surface [17, 18]. Since anatase is often the preferred form for TiO_2 photocatalysis [11, 19], fundamental study of this phase is once again key to bridging the TiO_2 materials gap.

2.1.2 Surface structure

As mentioned above, surface chemistry is determined, unsurprisingly, by the surface structure. Reactions on metal-oxide surfaces are often described within the

framework of acid-base interactions, oxidation-reduction reactions, or coordination events [20]. These paradigms are not rigidly defined nor are they mutually exclusive; they are simply helpful tools for categorizing and describing the complex interactions between an adsorbate and a surface. For instance, the dissociative adsorption of an alcohol molecule can be described as a deprotonation of the alcohol by a lattice oxygen anion acting as Brønsted base, while simultaneously complexing of the resultant conjugate base (i.e. alkoxide) with a metal cation acting as a Lewis acid. Alternatively, this event can be viewed as a fivefold coordinate metal cation filling its lone coordination vacancy with an adsorbate.

The metal-oxide surface also plays a role in the subsequent reactions. For instance, a reducible metal-oxide may facilitate an oxidation-reduction reaction between two adsorbates by 'lending' a lattice oxygen, thereby increasing the concentration of available oxidant species (and therefore the reaction rate) above that of the uncatalyzed reaction [1]. Oxidation and reduction can also occur via photo-generated holes and electrons, respectively. While charge carrier generation and migration is largely a bulk process, their lifetime on the surface and likelihood of transferring to an adsorbate is determined by the nature of particular surface sites on which they are localized. Catalytic surfaces can also electronically or sterically stabilize reaction intermediates, which reduces the energy penalty associated with breaking bonds in the reactant molecules [1]. For instance, it has been shown that the rate of oxidation of methoxide to formaldehyde on two similar rutile surfaces is determined by the proximity of the nearest oxygen anion to the methyl hydrogens [21]. That this distance is 0.3 Å less on one surface is credited

with mitigating the penalty associated with hydride abstraction, which results in an order of magnitude improvement in the reaction rate. Additionally, adsorbates may gather at specific surface features, such as step edges [ref] or multiply-undercoordinated cations, which effectively raises the local concentration and consequently the likelihood of reaction. As mentioned in the Introduction, fourfold coordinate Ti cations have been identified as the active sites for the coupling of acetic acid to produce acetone [6]. Presumably the two coordination vacancies accommodate two acetate molecules on a single surface site and this forced proximity greatly increases the chances of coupling. In each of these examples, it is clear that the physical and chemical structure (i.e. reducibility, electronic structure, coordination environment, etc.) play a key role in determine the activity and selectivity of a catalytic surface.

The remainder of this chapter deals with the reactivity of small oxygenates on four crystal planes: R-(110), R-(001), A-(101), and A-(001). R-(110) and A-(101) are the most stable surfaces of rutile and anatase, respectively, suggesting that they (along with equivalent planes[1]) would account for a large fraction of the exposed surface area in their respective nanocrystalline or powder forms [22]. The R-(110) surface consists of a plane of fivefold and sixfold coordinate Ti cations and threefold coordinate O anions, with parallel rows of twofold coordinate O anions protruding from the plane (see Figure 2.2a). These latter O anions are often referred to as bridge-bonded oxygen. Up to 5-10% of these O anions can be removed from R-(110) by annealing in vacuum [8]. Excessive

[1] Technically (110) refers only to the plane normal to the [110] vector. For any given plane, there is generally a family of structurally-equivalent planes, denoted in this case by {110}. Since most surface science studies involve macroscopic single crystals, using the single-plane designation, e.g. (110), is proper, but of course all statements also apply to the equivalent planes.

annealing can also cause this surface to reconstruct, most commonly in a (1 x 2) pattern. This reconstruction has been extensively studied [8, 23-25], but is beyond the scope of this review. The R-(110) surface unit cell is a rectangle of 6.50 Å x 2.96 Å (in the [1$\bar{1}$ 0] and [001] directions, respectively) and contains a single fivefold Ti cation, for a surface density of 5.2 x 10^{14} cm^{-2} of Ti surface sites.

The A-(101) surface, being the lowest-energy surface of anatase, accounts for roughly 95% of exposed surface area on the equilibrium crystal shape [26]. This surface has saw-tooth-like structure, shown in Figure 2.2b. The Ti cations are fivefold or sixfold coordinate, while the O anions are either twofold (along the points of the 'teeth') or threefold coordinate [27]. This surface is slightly more stable than R-(110), which in part explains why A-(101) does not appear to reconstruct. This surface is also apparently harder to reduce than R-(110) [8]. In other words, this surface is not amenable to the formation of oxygen vacancies and multiply-undercoordinated cations, which is consistent with the idea of relatively low catalytic activity. This surface has a 10.24 Å x 3.78 Å rectangular unit cell. With two fivefold Ti cations per surface unit cell, this surface has 5.16 x 10^{14} sites per cm^2, which is comparable to R-(110).

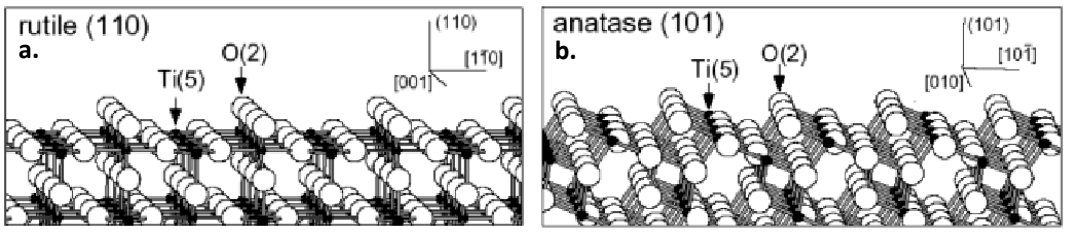

Figure 2.2 Schematic of the (a) unreconstructed rutile (110) and (b) anatase (101) terminations. Redrawn from [27].

The remaining two surfaces, R-(001) and A-(001), are less stable than the R-(110) and A-(101) surfaces described above. Accordingly, both of these surfaces reconstruct. The native R-(001) surface is especially unstable: all Ti cations are fourfold coordinate and all O anions are twofold coordinate. At low temperatures, the surface reconstructs into a series of {011} facets with (2 x 1) periodicity [28]. The Ti cations in this surface are fivefold coordinate. At higher temperatures (~ 950 K [29]), the reconstruction takes on a different form, although the precise structure has not been determined. It appears that it includes {114} facets, which contain fourfold coordinate Ti cations.

The A-(001) surface, on the other hand, appears at first to be stable: all Ti cations are fivefold coordinate and O anions are twofold and threefold coordinate (see Figure 2.3a). It is somewhat surprising, therefore, that this surface readily reconstructs [30, 31]. Aside from the (1 x 4) periodicity, not much is known for certain about this structure. As with the high-temperature reconstruction of R-(001), the precise structure of this reconstruction is still subject to debate. Herman et al. [30] first reported evidence of a reconstruction with (1 x 4) periodicity and presented several models. Stability arguments[2] pointed to a model consisting of {103} microfacets (Figure 2.3b) and exposing both fourfold and fivefold coordinate Ti cations as the most likely. Hengerer et al. [32] tentatively favored a model based on missing rows of bridge-bonded oxygens (Figure 2.3c) based on the observation that the native surface may be recovered in the presence of

[2] The principle of autocompensation is often used to predict stability of metal-oxide surfaces. Briefly, a surface is expected to be stable when the cations' 'dangling' bonds are vacant and those of the anions are filled.

oxygen. Liang et al. [33] found the {103} microfacet model to be inconsistent with positive-bias STM results and the missing-row model to be unlikely based on XPS studies. They instead proposed a model which effectively comprises {014} microfacets (Figure 2.2d). This model would also include some fourfold coordinate Ti cations. Reactivity studies by Tanner et al. [31] appear to rule out any models exposing fourfold coordinate Ti cations. A model consisting of {101} microfacets (Figure 2.3e) was suggested which contains only fivefold coordinate Ti cations but which is not entirely consistent with STM results. Around that same time, Lazzeri and Selloni [34] developed an 'ad-molecule' model (Figure 2.3f) in which TiO_3 groups form in rows on the surface. This surface would technically contain fourfold coordinate Ti cations, but the electronic geometry is expected to be closer to a distorted tetrahedron rather than an octahedron (as in bulk TiO_2), and one of the two coordination vacancies is expected to be located under the cation and thus inaccessible to adsorbates. Such Ti cations may not serve as suitable active sites for the probe reaction used by Tanner et al., and therefore this model is not necessarily inconsistent with that group's reactivity studies. However, Liang et al. [33] expressed reservations about any reconstructions involving non-anatase structures, since high-quality anatase films may be grown on top of the reconstructed A-(001) surface. In summary, an impressive array of models has been proposed for this reconstruction, but those without multiply-undercoordinated Ti cations appear to be more likely based on reactivity studies.

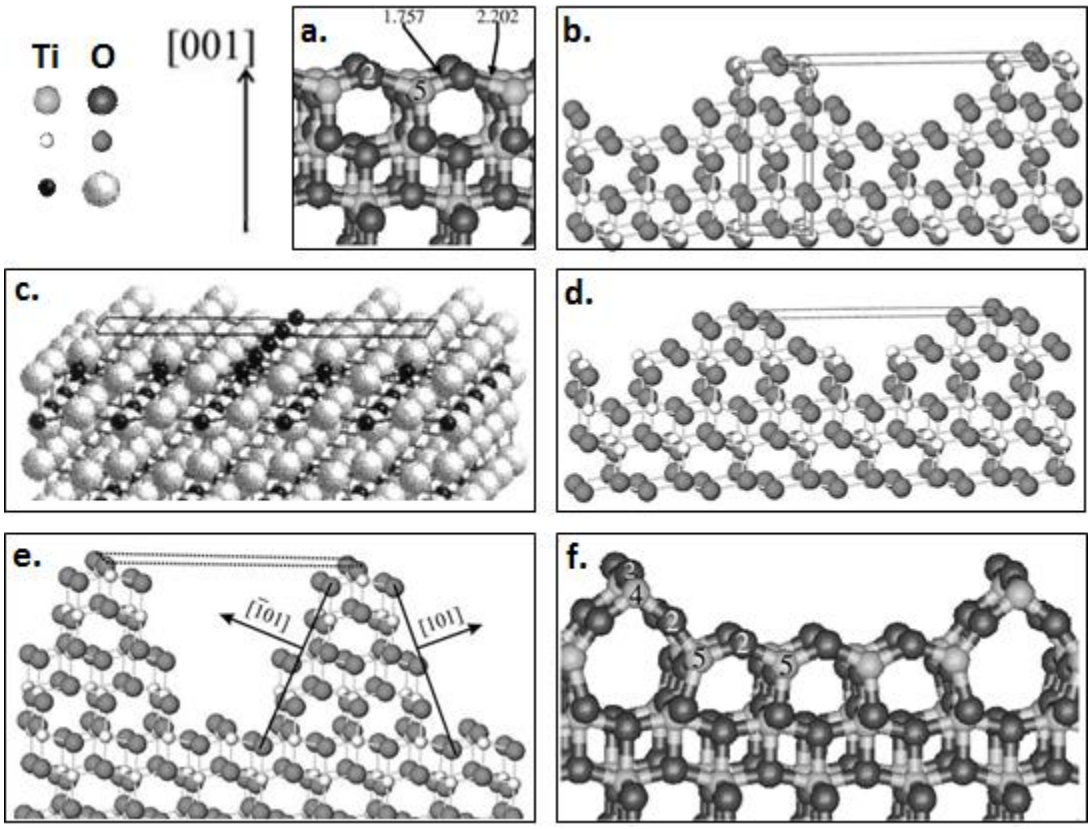

Figure 2.3 Schematic of the (a) native A-(001) surface and several proposed models for the (1 x 4) reconstruction: (b) {103} microfacet, (c) missing row, (d) {014} microfacet, (e) {101} microfacet, and (f) ad-molecule. Note the various color schemes. All panels are drawn with the [001] vector pointing downwards. Redrawn from [30, 31, 34].

2.2 Thermally-driven reactions of oxygenates on TiO_2

There is a vast body of literature concerning the adsorption and reaction of a wide range of organic and inorganic species on TiO_2. Water-TiO_2 interactions have been a particularly popular subject due to the promising photo-catalytic water-splitting capabilities demonstrated by TiO_2. However, understanding the behavior of low-molecular-weight alcohol and carboxylic acids provides a sufficient background for the

rest of this thesis. Therefore this summary will focus primarily on methanol, and to a lesser extent, other short-chain aliphatic alcohols and carboxylic acids.

2.2.1 Single crystal studies

The adsorption of both methanol [35, 36] and acetic acid have been studied extensively on the R-(110) surface. Methanol adsorbs both molecularly (i.e. without breaking intramolecular bonds) and dissociatively on this surface. Dissociative adsorption is typically associated with adsorption onto bridging oxygen vacancies (5-10% of sites on vacuum-annealed surfaces[8]), but it appears that methanol dissociates to a significant extent on non-vacancy sites as well. This latter dissociated species is bound less tightly to the surface than the former. This is reflected in the desorption temperatures associated with each adsorption state: molecular methanol on fivefold coordinate Ti, methoxide on non-vacancy sites, and methoxide on oxygen vacancy sites desorb at 295 K, 350 K, and 480 K, respectively (see Figure 2.4). There is also a smaller feature at 165 K representing molecular methanol H-bonded to bridging O which is not evident in Figure 2.4 [35]. The molecular and non-vacancy species adsorb in rows parallel to and between the bridging oxygen rows (see Figure 2.2a), with a spacing of two methanol/methoxide species per three R-(110) surface Ti cations [36]. This suggests a saturation coverage of 0.66 ML (~3.4 x 10^{14} cm^{-2}). The measured value of 0.59 ML (~3.2 x 10^{14} cm^{-2}) was attributed to imperfect packing, due in part to adsorption at oxygen vacancies. Acetic acid dissociates much more easily on this surface, which may be attributed in part to the relative acidity of the hydroxyl and carboxyl protons. The resulting acetate group binds in a bidentate

configuration (via the two O atoms) to adjacent Ti cations [37-40]. This leads to a density of one acetate group per two surface unit cells at saturation coverage. Near edge x-ray absorption fine structure [40] and non-contact atomic force microscopy [37, 38] studies have shown that the acetate species are oriented nearly completely normal to the surface. Adsorbate orientation plays a role in determining the likelihood of various reaction pathways [41].

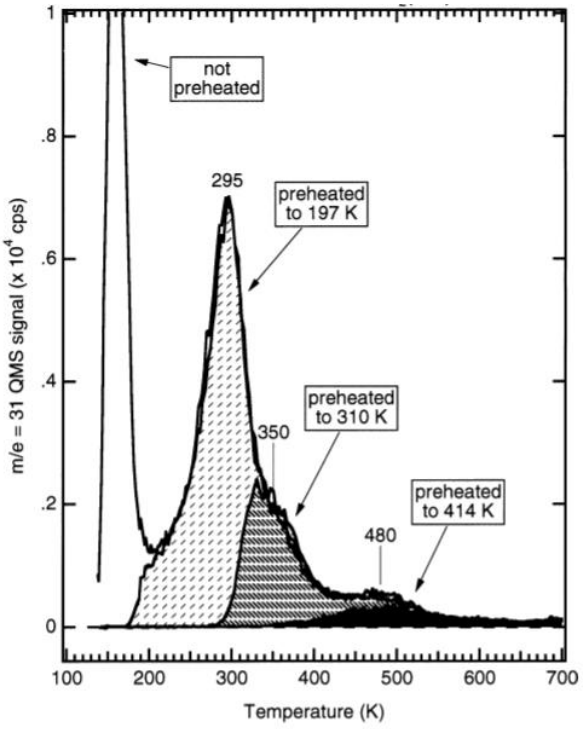

Figure 2.4 Methanol desorption from the methanol-covered R-(110) surface. From left to right, the peaks represent multilayer methanol, molecular methanol, methoxide on non-vacancy sites, and methoxide on bridge-bonded oxygen vacancies. Reproduced from [36].

As mentioned in section 2.1.2, the (110) surface is the lowest-energy surface of rutile. This suggests (1) that R-(110) makes up a large fraction of exposed surface area on

rutile nanocrystals and powders and (2) that this surface is relatively less-reactive than other rutile surfaces [42, 43]. Indeed, no reaction products are detected during methanol TPD on this surface. As shown in Figure 2.4, molecularly adsorbed methanol desorbs near room temperature, followed by recombinative methoxide desorption at 350 K and 480 K [35, 36]. However, co-adsorbed oxygen introduces two new reaction pathways. O_2 exposure at room temperature led to dissociation at O vacancies, leaving unpaired O atoms on the surface. These O adatoms were credited with facilitating O-H bond dissociation, increasing the fraction of methoxide species on the surface. This opens a new pathway for removal of methoxide from the surface: disproportionation of two methoxide groups to produce one molecule each of methanol and formaldehyde at 625 K. Interestingly, O_2 exposure at 150 K also results promotes formaldehyde production, but through a completely different pathway. It appears that O_2^- surface species attack the C-H bond of a methoxide group, creating adsorbed formaldehyde which desorbs at 250 K [35]. Acetic acid is slightly more reactive on this surface, undergoing unimolecular dehydration to produce ketene near 520 K [44].

The higher-energy R-(001) surface catalyzes a much richer range of reactions than the relatively-stable R-(110) surface. Kim and Barteau have conducted a series of studies [6, 29, 45, 46] on sputtered (i.e. oxygen-deficient) R-(001) and on both reconstructions described in section 2.1.2. On all surfaces, methanol [6, 45] adsorbs both molecularly and dissociatively, with the molecular state desorbing below 300 K. Methoxide groups are located on fivefold coordinate Ti cations, with their corresponding protons abstracted by nearby bridging oxygen atoms, forming surface hydroxyl groups.

These groups react in one of two competing pathways near 365 K: reaction with another hydroxyl group to produce water and a single oxygen vacancy, or recombination with methoxide to produce methanol. On all surfaces, roughly half of the methoxide groups desorb recombinatively via the second pathway, with the remaining undergoing one of several reactions with differing selectivity depending on the surface conditions. Table 2.1 summarizes the distribution of products from dissociated species still on the surface at 300 K (i.e. molecularly adsorbed species are not included in the yield calculations). Methoxide groups may react at an oxygen vacancy site, some of which are produced by the coupling of surface hydroxyls to produce water, to produce a surface methyl group [43]. This methyl group can either further decompose to atomic C and H, or combine with an adsorbed H to produce methane. H produced in the former reaction may combine with a surface methoxide to produce molecular methanol around 600 K. Molecular methanol and methane are the first and second most likely fates for methoxide not removed from the surface at 365 K. Other products include formaldehyde, which was produced on both reconstructions and which was attributed to unimolecular dehydrogenation in this study [6] (although a similar reaction on R-(110) has been attributed to disproportionation of methoxide [35]), and bimolecular coupling of methoxide to produce dimethyl ether, which was only produced on the high temperature reconstruction. This last observation enabled Kim and Barteau to assign fourfold coordinate cations as the active site for this coupling reaction [6].

Table 2.1 Product selectivity during methanol TPD on R-(001) for several surface conditions. Redrawn from [6].

Product	Sputtered	{011}-faceted	{114}-faceted
CH_3OH (~365 K)	0.52	0.56	0.51
CH_3OH (~600 K)	0.26	0.22	0.17
CH_4	0.17	0.18	0.07
CO	0.06	–	–
CH_2O	–	0.04	0.07
CH_3OCH_3	–	–	0.08

Kim and Barteau also investigated the reactivity of other alcohols on the low temperature reconstruction of R-(001) [45]. Product selectivity was not a strong function of the parent alcohol identity (see Table 2.2), with two major exceptions: (1) the deoxygenation pathway that produces methane from methanol was supplanted by a dehydration pathway to produce alkenes and (2) the corresponding dehydrogenation reaction was not observed for 2-propanol (i.e. no acetone was detected). The dehydration pathway is understood in terms of β-H elimination (whereas α-H abstraction produces the corresponding aldehyde). Obviously methanol cannot undergo β-H elimination, but it is interesting that deoxygenation, which was the dominant reaction pathway for methanol on this surface [6], was not observed for larger alcohols. While the product distribution was quite similar across the various parent molecules, the high-temperature desorption products showed a clear trend of lower desorption temperature with increasing alcohol complexity (see Figure 2.5). This can be interpreted in terms of decreasing alkoxide stability [45].

Table 2.2 Product selectivity during aliphatic alcohol TPD on {011}-faceted R-(001) for various parent alcohols. Numbers represent fractional yields. Based on [6, 45].

Product	CH_3OH	C_2H_5OH	C_3H_7OH	$CH_3CH(OH)CH_3$
alcohol (low temp)	0.56	0.52	0.44	0.46
alcohol (high temp)	0.22	0.25	0.24	0.25
Alkane	0.18	–	–	–
Alkene	–	0.19	0.29	0.29
Aldehyde	0.04	0.04	0.03	–

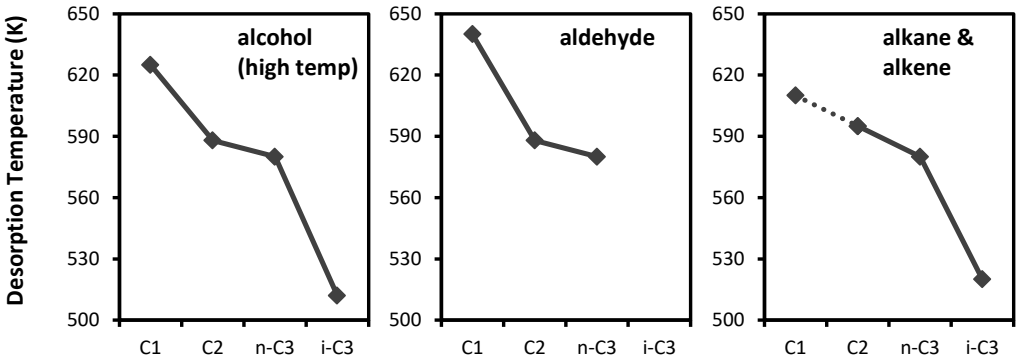

Figure 2.5 Trends in product desoption temperatures during aliphatic aclohol TPD on {011}-faceted R-(001) for various parent alcohols. Based on [6, 45].

Analogous studies of carboxylic acid reactivity were conducted by Kim and Barteau [29, 46]. As with the alcohols discussed previously, formic acid, acetic acid, and propionic acid adsorb both molecularly and dissociatively on these surfaces, with the molecular species desorbing below 300 K. The intensity of the C(1s) XPS peak on surfaces annealed to various temperatures indicated that acetate coverage was nearly

identical on both the sputtered and {011}-faceted surfaces, but roughly 20% lower on the {114}-faceted surface. These acids are generally more reactive than the alcohols; of the alkoxides adsorbed at 300 K, half reformed the parent alcohol at 365 K, while only ~15% of the carboxylates recombined and desorbed at 390 K. Trends in the three major reaction pathways for acetic acid (unselective decomposition, dehydration, and bimolecular ketonization) as a function of surface treatment are shown in Figure 2.6. Table 2.3 quantifies the analogous products for formic acid and propionic acid as well. Note that it is possible for a single acetate molecule to produce two CO species, which explains the surprising yield for this product on the sputtered surface. Dehydration was typically the dominant pathway on the oxidized (i.e. not sputtered) surfaces. Dehydration of acetate and propionate produces ketene and methyl ketene, respectively. The corresponding C_1 species, formate, cannot undergo dehydration, as was the case with methoxide. Instead, the unselective decomposition to CO and CO_2, which occurs for all molecules, was the dominant pathway for this molecule. The dehydration products are highlighted in orange in Table 2.3. A coupling reaction was also observed only on the high temperature reconstruction, as was the case with the coupling of alkoxides to produce symmetric ethers discussed above. In the case acetate and propionate, this coupling took the form of bimolecular ketonization to produce acetone and 3-petanone, respectively. The former reaction has been proposed to involve a ketene intermediate reacting with an acetate co-adsorbed to the same Ti cation [47], although alternative mechanisms have been put forward [48].

The apparent lack of bimolecular coupling products (etherification of alkoxides and ketonization of carboxylates) on the sputtered R-(001) surface raises questions about the assignment of fourfold coordinate Ti cations. This surface is severely oxygen-deficient (see top panel of Figure 2.6), thus multiply-undercoordinated Ti cations are certainly present. Kim and Barteau [29] suggested that the highly-reduced state of this surface promoted deoxygenation over coupling, and that the site requirements for coupling reactions may in fact be twofold: (1) two coordination vacancies to accommodate two adsorbates and (2) a 4+ oxidation state to discourage deoxygenation.

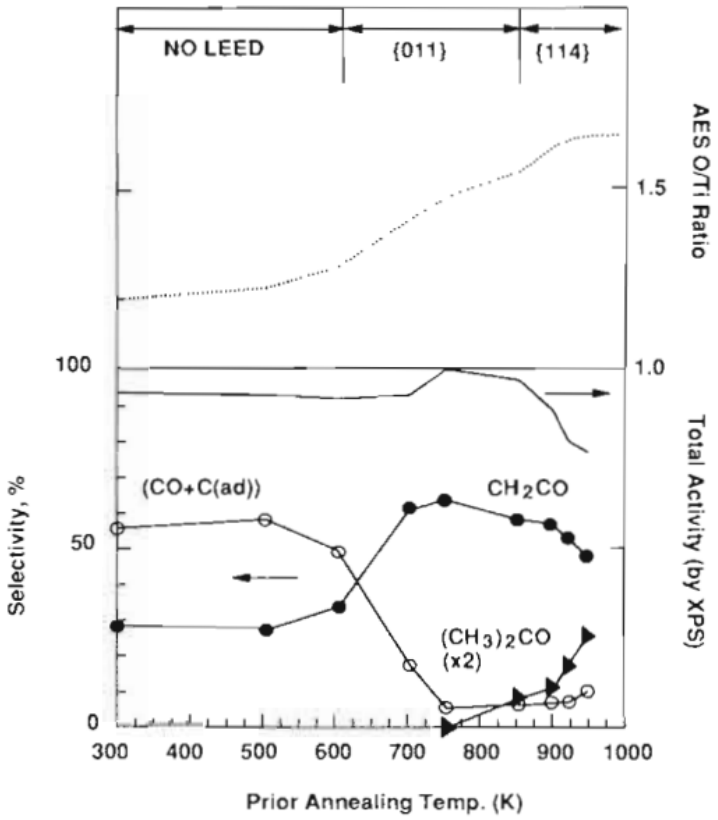

Figure 2.6 Extent of surface oxidation (top panel) and product distribution (bottom panel) as a function of surface pre-treatment. Reproduced from [29].

Table 2.3 Product distribution during carboxylic acid TPD from R-(001) for several surface conditions and parent acids. Numbers represent moles of product per mole of the adsorbed parent acid. The corresponding dehydration and bimolecular reaction products are highlighted in cyan and orange, respectively. Based on [29, 46].

Parent acid	Product	Sputtered	{011}-faceted	{114}-faceted
HCOOH	HCOOH (390 K)	No data	0.13	0.13
	HCOOH (560 K)		0.19	0.13
	CO		0.50	0.44
	CO_2		0.18	0.21
	CH_2O		–	0.10
CH_3COOH	CH_3COOH (390 K)	0.09	0.15	0.13
	CH_3COOH (~590 K)	0.07	0.16	0.16
	CO	1.10	0.11	0.20
	CH_4	0.01	–	–
	CH_2CO	0.28	0.64	0.47
	$CH_3(CO)CH_3$	–	–	0.09
C_2H_5COOH	C_2H_5COOH (390 K)	No data	0.14	No data
	C_2H_5COOH (580 K)		0.04	
	CO		0.09	
	CH_3CHCO		0.67	0.59
	$C_2H_5(CO)C_2H_5$		–	0.05

The availability and stability of rutile single crystals has encouraged a vast array of research on these surfaces, of which only a small part has been presented here. The opposite is true of the anatase phase: investigations into reactivity on single crystalline anatase are quite limited. The difficulty of working with anatase single crystals is

highlighted by the fact that many of the extant anatase single crystal studies have actually employed epitaxial anatase thin films.

A study of water and methanol adsorption and reaction on the A-(101) surface was carried out by Herman at al. [27]. The absence of the dissociative adsorption of water (which occurs at O vacancies) confirms the assertion made in section 2.1.2 that A-(101) is harder to reduce than R-(110). Methanol, on the other hand, undergoes detectible, but very limited, dissociative adsorption. Methanol TPD (Figure 2.7) identified five desorption states: multilayer (desorbs at 135 K), molecular methanol adsorbed on bridging oxygen via hydrogen bonding (170 K), molecular methanol adsorbed on fivefold coordinate Ti (260 K), methoxide adsorbed on fivefold coordinate Ti (410 K), and methoxide adsorbed on step edges (610 K). This surface has higher overall methanol coverage than R-(110), but with fewer dissociated species. Capacities for each adsorption state on the two surfaces are quantified in Table 2.4. Despite the presence of methoxide groups on this A-(101) surface, no formaldehyde desorption was observed. In fact, no reaction products were observed at all during methanol TPD. Comparison of the Ti($2p_{3/2}$) and C(1s) XPS peak centers on the methanol-covered surface confirmed the finding that methanol adsorption is almost entirely molecular. Furthermore, the observation that the C(1s) peak center was relatively insensitive to methanol coverage, while the small O(1s) peak near 530 eV (corresponding to O atoms in adsorbate species, rather than lattice O) shifted significantly upon increasing methanol adsorption is consistent with methanol/methoxide interacting via its O atom rather than its methyl group. As on R-(110), acetic acid dissociated more readily than methanol. Acetate groups bind in a

bidentate configuration on this surface as well, which leads to a saturation coverage of nearly 0.5 ML (1 monolayer = 5.16 x 10^{14} cm^{-2} on this surface, i.e. one adsorbate per fivefold Ti surface site) [49], as would be expected if each acetate occupies two adjacent surface sites. Molecular, monodentate adsorption was observed at higher coverages. Heating to 570 K removed 90% of adsorbates, with the remaining species clustered near step-edges (perhaps analogous to the 610 K desorption state for methanol).

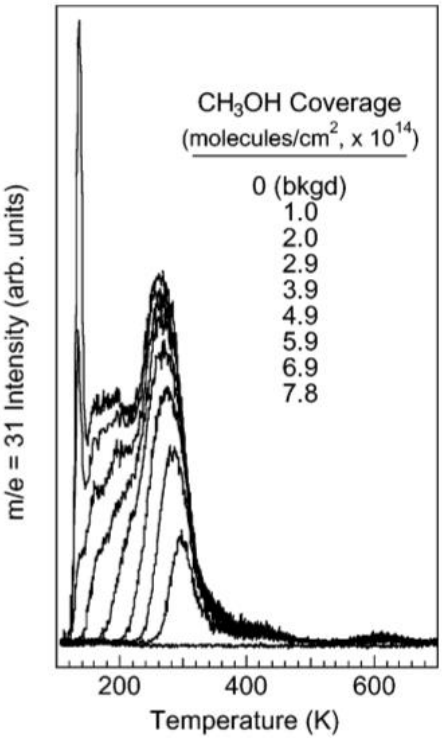

Figure 2.7 Methanol desorption from the methanol-covered A-(101) surface. Identification of the desorption features may be found in Table 2.4. Reproduced from [27].

Table 2.4 Methanol adsorption states on A-(101) and R-(110). Based on [27, 35, 36].

Adsorption Mode	Desorption Temperature (K)		Approximate Coverage [Cumulative] (10^{14} cm^{-2})	
	A-(101)	R-(110)	A-(101)	R-(110)
Multilayer	135	145	[6.0+]	[4.5+]
Molecular - twofold O	170	165	2 [6.0]	1.3 [4.5]
Molecular - fivefold Ti	260	295	3.7 [4.0]	2.0 [3.2]
Dissociative - fivefold Ti	410	350	0.2 [0.3]	0.8 [1.2]
Dissociative – step edges (A) or O vacancy (R)	610	480	0.1 [0.1]	0.4 [0.4]

Tanner et al. [31, 50] have carried out a series of structural and reactivity studies of the A-(001) surface. As discussed in section 2.1.2, this surface reconstructs with (1 x 4) periodicity. STM of the reconstructed surface exposed to a saturation dose of formic acid revealed that formate only adsorbs along the bright rows which have (1 x 4) spacing (see Figure 2.8). These rows are generally interpreted to be Ti cations along the ridges in the reconstructed surface. Furthermore, formate groups were packed along these rows with a density of one adsorbate for every two surface unit cells (consistent with a bidentate, bridging adsorption mode), for an overall packing geometry of (2 x 4). Thus the surface saturates at ⅛ ML, compared to nearly ½ ML for carboxylic acids on A-(101) [49] and R-(110) [37, 38]. Both formic acid and acetic acid were remarkably unreactive on this surface, with no evidence of either the dehydration or bimolecular pathways observed on R-(001) [29, 46]. The lack of biomolecular coupling suggests the reconstruction of the A-(101) surface does not contain fourfold coordinate Ti cations. The

lack of dehydration activity was explained in terms of surface geometry. Dehydration requires abstraction of one of the carboxylate's H by a surface O. On the R-(110) surface, rows of bridging O are raised above the Ti adsorption sites (see Figure 2.2a), which decreases the distance between surface O and H. On the reconstructed A-(001) surface, if carboxylate do in fact adsorb along the tops of the ridges, the corresponding H-O distance is much further, which lowers the likelihood of reaction. Sputtering introduced two new reaction pathways: reduction of formate to formaldehyde and acetate to CO and a surface methyl group; and dehydration of formate to CO and acetate to ketene. The reduction pathway is unsurprising, as sputtering creates surface Ti^{3+} cations which may act as reduction sites. Explanation of the dehydration pathway requires a little more subtlety. Recall that the dehydration pathway on other TiO_2 surfaces is thought to occur on fivefold coordinate Ti adsorption sites. It was suggested that sputtering creates such sites (e.g. by ejecting a lattice O from above a sixfold coordinate Ti). Some of these sites will undoubtedly have nearby O within reach of the carboxylate's H, as opposed to the Ti adsorption sites along the tops of the ridges on the unsputtered surface.

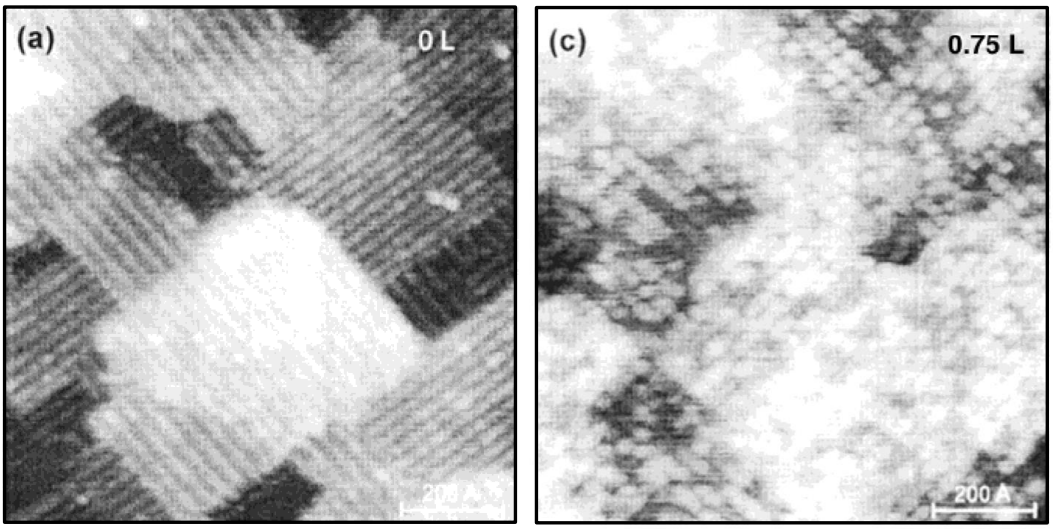

Figure 2.8 STM showing the adsorption sites for acetic acid on the reconstructed A-(001) surface. The left panel shows the clean surface and the right panel shows the surface after exposure to 0.75 L acetic acid. Redrawn from [50].

One of the proposed benefits of studying well-defined, nanocrystalline model catalysts is filling in the gaps in the single-crystal literature. For instance, at the outset of this thesis, no study had been undertaken on the reactivity of methanol on the A-(001) surface. Therefore the reactivity of nanocrystals partially exposing well-defined A-(001) facets may indicate the type of chemistry occurring on this surface. However, very recently a study of methanol reactivity on single-crystalline A-(001) appeared in the literature [51]. This study observed both formaldehyde (via disproportionation) and dimethyl ether production, although no mention was made of methane. It is unclear how to reconcile these results with those of Tanner et al. [31], since the latter ruled out fourfold coordinate cations (or at least those with two coordination vacancies accessible to adsorbates) on this surface with a high degree of certainty.

2.2.2 Studies of TiO_2 powder

Reactivity studies of high-surface-area powder catalysts rarely result in novel structure-activity relationships, thus they do not add much to what has been reviewed above. Nevertheless, a high-level summary of such studies has been provided in the interest of illustrating the materials gap between these two classes of materials. The effect of surface structure on catalytic activity is illustrated in Figure 2.9, which summarizes the product distribution during methanol TPD the various TiO_2 surfaces discussed in this and previous sections.

Kim and Barteau investigated the reactivity of various low-molecular-weight alcohols [14, 43, 52] and carboxylic acids [53] on anatase powder. Results were qualitatively similar to what has been seen on the various single-crystal surfaces. Once again, all reagents adsorbed both molecularly and dissociatively. Dissociated species underwent either recombinative desorption near 400 K or one of the reaction pathways introduced earlier, with a few minor changes. For instance, methyl ketene, which results from dehydration of propionic acid, was not observed directly, instead having isomerized to acrolein upon readsorption.[3] Interestingly, a follow-up study comparing the reactivity of small alcohols over anatase and rutile powder found almost no differences in product selectivity, but there was a small difference in overall alcohol conversion which was attributed to the density of surface sites on each sample [14]. This suggests that (1) bulk

[3] The use of single-crystal surfaces in an ultra-high vacuum environment in the previously-described studies precludes readsorption.

properties do not meaningfully impact surface activity and (2) the surface environment is not significantly distinct between anatase and rutile powders.

While pure anatase and rutile powders are excellent models of industrial TiO_2 catalysts, they are still somewhat idealized. One particularly-common form of TiO_2 catalyst, Degussa P25, is actually a mixture of the two phases. Methanol TPD [10] on P25 revealed higher selectivity towards the coupling product, dimethyl ether, and higher overall methanol conversion (see right-most column of Figure 2.9). The origins of this effect are not clear, but it is perhaps related to the concentration of adsorption sites. For instance, Luo and Falconer observed increased aldolization selectivity on P25 [54, 55] relative to those on single-crystalline TiO_2 [56, 57], and they suggested that the higher density of surface sites may promote coupling-type reactions.

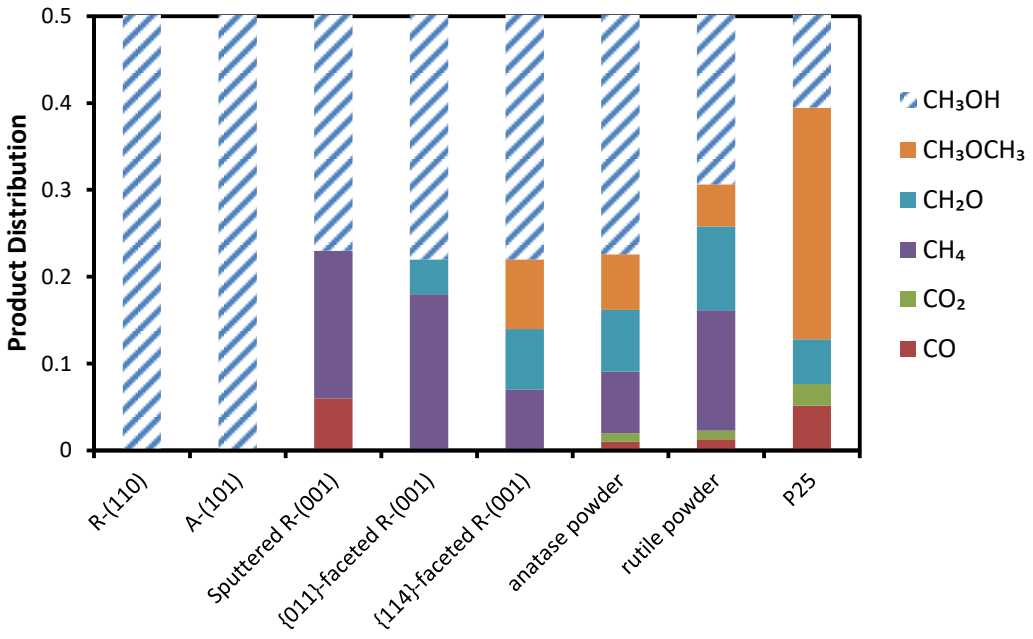

Figure 2.9 Product distribution during methanol TPD on various TiO_2 surfaces. Based on [6, 10, 14, 27, 35].

2.3 Photo-induced reactions of oxygenates on TiO_2

This thesis is primarily concerned with the reactivity and photoactivity of methanol. The thermally-driven reactions of methanol on TiO_2 have many analogs with those of carboxylic acids, thus reviewing the reactivity of organic acids in addition to alcohols in section 2.2 was intended to provide a deeper understanding into the reactivity of methanol specifically. While carboxylic acids are known to undergo photocatalytic reactions on TiO_2 [9, 58], these reactions have little in common with the photocatalytic reactions of methanol. Therefore this section will be limited to the review of methanol photochemistry, except where studies of other reagents provide insight into the photocatalytic properties of the TiO_2 itself.

2.3.1 Overview of photocatalysis

All photocatalytic processes begin with the absorption of a photon. But understanding this event requires understanding the electronic band structure. In isolated atoms, each electron resides in one of many discrete orbitals. Each orbital has a specific, narrowly-defined energy. Only photons with energy corresponding to transitions between orbitals may interact with individual atoms, which gives rise to sharp lines seen in atomic absorption spectra. However, bulk materials do not share this property. For instance, glass does not absorb any wavelengths of visible light, while metals reflect all wavelengths quite well.

When two atoms combine to form a molecule, the individual atomic orbitals overlap and form molecular orbitals. In-phase overlap results in a bonding orbital with lower energy than the original atomic orbitals, and out-of-phase overlap creates an anti-bonding orbital with higher energy (N=2 portion of Figure 2.10). When more atoms come together, more molecular orbitals are formed. Eventually the orbitals are so closely spaced that they can be treated as a continuous band of valid energy states, as depicted in Figure 2.10.

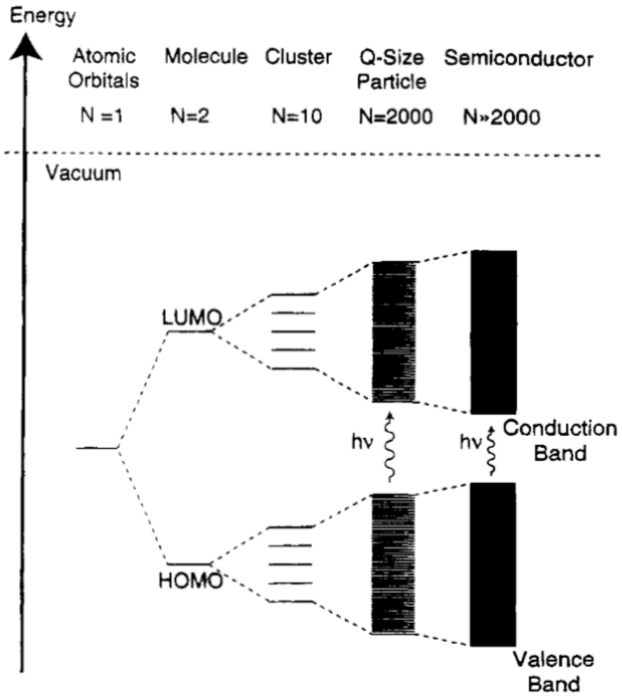

Figure 2.10 Origins of the electronic band structure of semiconductors. Reproduced from [4].

Electrons tend to populate the available energy states from lowest energy to highest energy. The highest-energy band which is still occupied is called the valance

band, while the conduction band is the lowest-energy unoccupied band. (These are the two bands shown on the right side of Figure 2.10, but keep in mind that there will be additional bands above and below these two.) The conduction band is responsible for electrical conductivity in solids. In metals, a single band satisfies both of these definitions, which is why metals are highly conductive. Insulators feature a large gap, called the band gap, of forbidden energy states between the top of the valence band and the bottom of the valance band, which makes the conduction band virtually inaccessible to electrons. However, there is a third category of solids, called semiconductors, in which the band gap is small enough that a small fraction of electrons can be excited into the conduction band. These electrons may be excited thermally, by an applied voltage (i.e. solid-state transistors), or by the absorption of a high-energy photon.

Figure 2.11 gives a qualitative overview of the major steps in semiconductor photocatalysis. The first step is the absorption of an energetic photon, which boosts an electron from the valence band to the conduction band. The vacancy left behind in the valence band is referred to as a hole. The excited electron may relax back into the vacancy, which may generate heat or another photon (i.e. fluorescence), or they may diffuse throughout the solid. If the conduction-band electron reaches the surface, it may reduce an adsorbed molecule. Likewise, a valence-band hole may oxidize an adsorbate. Thus photocatalysis is a form of oxidation-reduction chemistry. However, in photocatalysis the reducing power of the electron is derived from the energy of the photon and not a strong reducing agent (likewise for the oxidation potential of the hole).

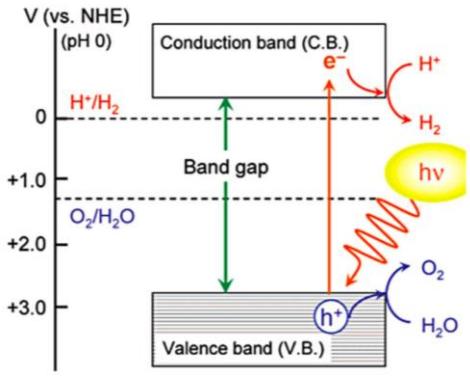

Figure 2.11 General photocatalytic process. The water splitting reaction is depicted here, but this same scheme can be used for any oxidation-reduction reaction. Reproduced from [59].

Of course, like any oxidation-reduction reaction, one half-reaction cannot occur without the other. This means that photo-oxidation reactions require an electron scavenger, usually adsorbed O_2, to facilitate the reduction half-reaction. There are two mechanisms by which a hole can oxidize a surface species. The direct oxidation mechanism involves the transfer of an adsorbate electron directly to a hole in the semiconductor. There is also an indirect oxidation mechanism, where an intermediate OH● radical oxidizes the adsorbate after being oxidized by the semiconductor [9]. It has also been proposed that certain intermediates such as O_2 may drive oxidation reactions on the surface after accepting an electron from the conduction band [9, 60-62].

The size of the band gap determines the reducing and oxidizing power of the electrons and holes, respectively. For instance, the water splitting reaction has a standard potential of -1.23 V [63]. Therefore no semiconductor with a band gap smaller than 1.23 V (ignoring overpotentials) can photocatalytically split water on its own. Even if such a semiconductor were illuminated with photons with energy greater than 1.23 V, the extra-

energetic electrons will thermalize (i.e. relax to the bottom of the conduction band) within femtoseconds [11], long before they could reach the surface and participate in a reaction. Thus the band gap sets an upper limit on the reduction potential of photo-excited electrons. In addition to band gap size, the position of the bands further limits the range of reactions which may be driven by any particular photocatalyst. In other words, a reduction reaction can only be driven if the conduction band lies above the reaction's reduction potential (and vice versa for oxidation). Figure 2.12 shows the band positions of several semiconductors relative to relevant potentials for water splitting. Note that several materials have band gaps with more than enough energy to carry out both half-reactions, but they are limited to one or the other based on band position. However, the band position can change in response to factors such as pH and applied voltage.

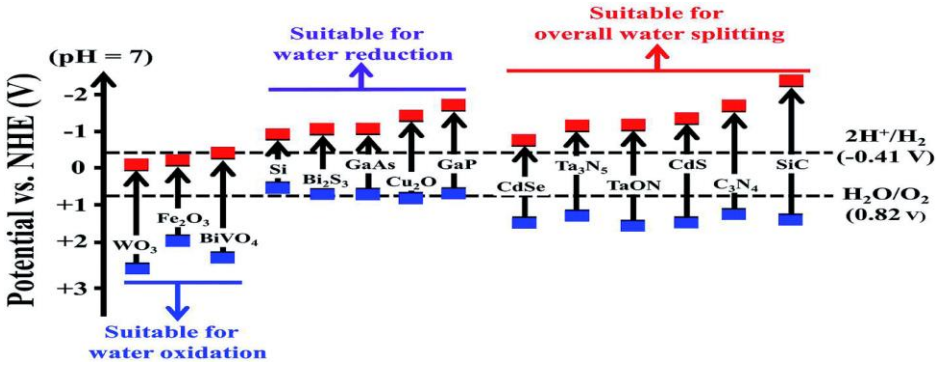

Figure 2.12 Role of band position in determining valid reactions. Reproduced from [64].

The activity of a photocatalyzed reaction also depends on the relative alignment of electronic states in the adsorbed reactant molecules. For instance, as will be discussed later, methoxide is photo-oxidized on TiO_2 much faster than molecular methanol [65]. It

appears that the highest occupied molecular orbital of methoxide is much closer in energy to the top of the TiO_2 valence band than that of methanol [59, 66], which facilitates the electron transfer process.

Finally, each electronic state possesses a specific crystal momentum. In general, the bottom edge of the conduction band will reach a minimum energy for a single momentum value, and likewise the top edge of the valence band reaches a maximum at a single value for momentum. If these two momenta are the same, then momentum conservation holds for each excitation event. This is called a direct band gap. If, however, the two extrema occur at separate momentum values, then the excitation event involves a change in momentum. Since photons carry very little momentum, the balancing momentum must come from another source. In materials with such a band gap, called an indirect band gap, the photon absorption event must coincide with the absorption or generation of a phonon.[4] This presents an additional barrier to the absorption of a photon, but it has an advantage as well. Recombination of the electron and hole in an indirect band gap semiconductor also must coincide with the appropriate phonon in order for momentum conservation to hold. This reduces the rate of recombination, increasing charge carrier lifetimes and thus increasing the chances that photo-generated electrons and holes will participate in surface reactions. TiO_2 anatase has an indirect band gap while TiO_2 rutile has a direct band gap [9].

[4] Phonons are collective, periodic oscillations of a crystal lattice. Technically they do not carry momentum in the conventional sense, but they play a role in momentum conservation when transitioning between states with differing crystal momentum (which in turn is not proper momentum either).

2.3.2 Single crystal studies

The photochemistry of methanol on the R-(110) surface has been investigated extensively by two groups in particular, those of Michael Henderson [35, 36, 65, 67, 68] and Xueming Yang [21, 69-74]. In general, UV irradiation may lead to dissociation of adsorbed methanol (in addition to the thermally-induced dissociation discussed in section 2.2), oxidation of methoxide to formaldehyde, and coupling of methoxide and formaldehyde to produce methyl formate.

Methanol photo-dissociation occurs on fivefold coordinate Ti cations with neighboring bridge-bonded O to accept the H [69, 74]. There is some level of disagreement in the literature over the importance of photochemical methanol dissociation versus thermal dissociation. Yuan et al. [75] measured changes in the various C(1s) peaks during UV irradiation and argued that a model in which the photochemical dissociation pathway is negligible is inconsistent with the results. However, it is clear that the dissociated species is much more reactive under UV illumination than the molecular species [65, 76]. For instance, Shen and Henderson observed an improvement of nearly an order of magnitude in the initial photo-oxidation rates of methoxide over methanol (see Figure 2.13). It is clear that the photo-oxidation of methoxide proceeds much faster on this surface than any photo-dissociation of methanol, otherwise the methanol-covered surface would rapidly convert to a methoxide-covered surface and the two cases would be indistinguishable. It has been suggested that methoxide's increased potential for photo-oxidation is a result of a closer alignment between its own electronic states and the top edge of the valance band of TiO_2, which facilitates hole transfer from the surface to

the adsorbate [59]. Thus the methanol photo-oxidation activity on TiO_2 surfaces is strongly-linked with the capability of the surface to thermally-dissociate methanol and with the ability of O adatoms to promote methanol dissection [35, 67].

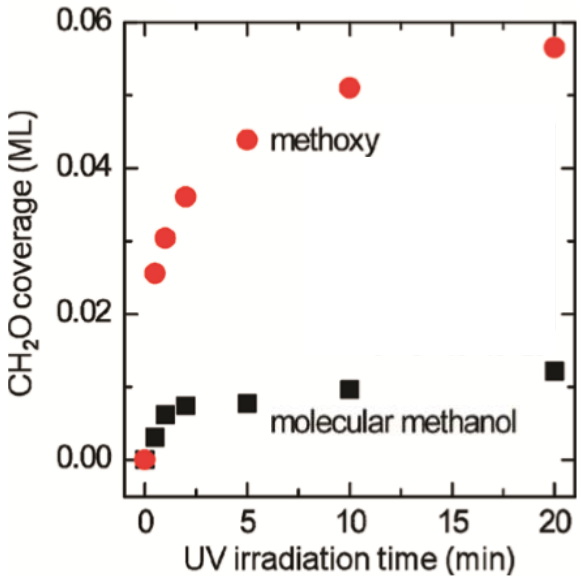

Figure 2.13 Formaldehyde production as a function of UV exposure for methoxide- and methanol-covered R-(110) surfaces Redrawn from [65].

Photo-oxidation of methoxide to formaldehyde involves abstraction of a methyl-H by a bridge-bonded O. This is supported by an investigation into the effects of water on methanol photochemistry by Shen and Henderson [68]. It was observed that water hydrogen-bonded to the bridging O inhibited methoxide photo-oxidation. Additionally, electron paramagnetic resonance studies suggest that photo-generated holes become trapped at twofold coordinate O surface sites [77], which is consistent with the idea that these sites play a role in the photo-oxidation process. It appears that the distance between

these twofold O sites and the methyl-H is a key parameter in determining the photo-oxidation rate. A density functional theoretic simulation of methoxide on both R-(110) and R-(011) found this distance to be 3.1 Å on R-(110) and 3.4 Å on R-(110), which was used to explain the increased oxidation activity observed on the former surface during methanol TPD [71]. The H left on the bridging O as a result of this reaction, as well as the dissociation of methanol, may combine upon heating, desorbing as H_2 [72, 76].

Under UV illumination, formaldehyde may continue to oxidize by cross-coupling with methoxide to produce methyl formate. This is known to occur on R-(110) [70, 72, 75, 78] and also on A-(101) [76]. TPD of methanol and isotopically-labeled formaldehyde (Figure 2.14) by Phillips et al. [78] determined that (1) the coupling step requires UV exposure, as no methyl formate was produced from a methanol- and formaldehyde-covered surface without illumination, and (2) the coupling occurs between methoxide and an oxidized intermediate of formaldehyde, since only the 'formate' component of the methyl formate product retained formaldehyde's isotope labels, while the 'methyl' portion was unlabeled and thus derived from methoxide. It was suggested that this oxidized formaldehyde intermediate may be a formyl (CHO) radical. Others [70] have argued instead that the adsorbed formaldehyde diffuses across the surface and couples directly with the methoxide, without going through a formyl intermediate. In this case, the coupled product would still need to transfer a H from the formaldehyde/formate carbon to the TiO_2 surface.

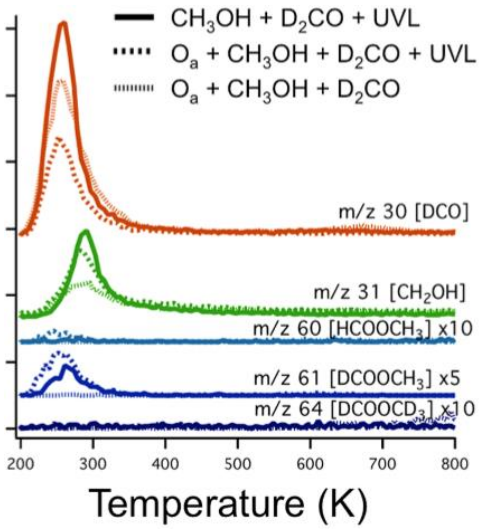

Figure 2.14 TPD results from methanol and isotopically-labeled formaldehyde on R-(110). Redrawn from [78].

2.3.3 Other photocatalytic studies of TiO_2

The previous section focused exclusively on surface reactions themselves. However, there is much to be learned in terms of structure-activity relationships by investigating the processes leading up to the surface reaction. These include charge-carrier separation at phase boundaries, charge-carrier separation at the intersections of well-defined facets, anisotropic charge-carrier migration, and the effects of crystallinity, surface energy, and lattice strain on overall photoactivity.

The commercial TiO_2 catalyst P25, which was discussed in section 2.2.2, is considerably more active than pure-phase TiO_2 catalysts for many photocatalytic applications [9]. There is still some debate over the exact reason for the high activity, but it is commonly thought that the two-phase mixture acts as a sort of semiconductor heterojunction due to their slightly different electronic band structures [79, 80].

Whenever two semiconductors are in electrical contact, charge is distributed across the interface such that the fermi levels are aligned on both sides. The resulting gradients in both carrier concentration and electric potential tend to separate photo-generated charge carriers by favoring electron transport in one direction across the interface and hole transport in the other direction. Since rutile and anatase have slightly different bandgaps, it has been proposed that the antase-rutile phase boundaries in P25 and other mixed-phase TiO_2 photocatalysts act as heterojunctions, sending photo-generated holes to the anatase crystallites (see Figure 2.15a). This would decrease the probability of electron-hole recombination and thus increase the quantum yield (i.e. the fraction of photons which successfully drive a reaction). Interestingly, it appears that a similar effect may even occur to some extent between different facets of a single-phase nanocrystal [42, 62, 81-83]. Ohno et al. [82] carried out a series of solution-phase photo-deposition experiments on anatase nanocrystals to illustrate the separation of photo-generated electrons and holes onto separate facets of anatase nanocrystals. Immersion of nanocrystals in an aqueous H_2PtCl_6 solution and exposure to UV light resulted in Pt reduction and deposition preferentially on the {011} facets (Figure 2.15b), while an analogous experiment in $Pb(NO_3)_2$ solution saw oxidation and deposition of PbO_2 particles primarily on the {001} facets. The spatial segregation of oxidation and reduction processes suggests a separation of the photo-induced charge carriers themselves, which would be expected to increase photocatalytic efficiency.

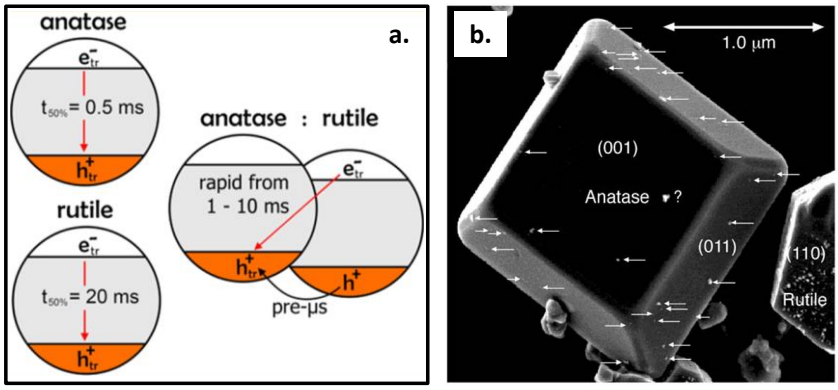

Figure 2.15 (a) Representation of charge carrier separation at the anatase-rutile interface. Reproduced from [79]. (b) Location of Pt particle deposition on an anatase nanocrystal, indicating the reduction preferentially occurs on the {011} facets. Reproduced from [82].

The migration of electrons and holes within the nanocrystal is not isotropic. For instance, holes are thought to migrate by 'hopping' between lattice O anions. A density functional theoretic study found one particular O-O hopping event (labeled D in Figure 2.16a) to be orders of magnitude more efficient than the other possibilities [15]. When considering all geometrically-equivalent transfers, this suggests a net movement along the [100] axis. An analogous study of the transport of conduction-band electrons (which are thought to 'hop' between Ti^{4+} cations), also found some anisotropy (see Figure 2.16b), although to a lesser extent [16]. Taken together with the facet-dependent charge-carrier separation discussed above, this suggests that the shape of a TiO_2 nanocrystal can strongly impact the photocatalytic activity [42, 60, 83].

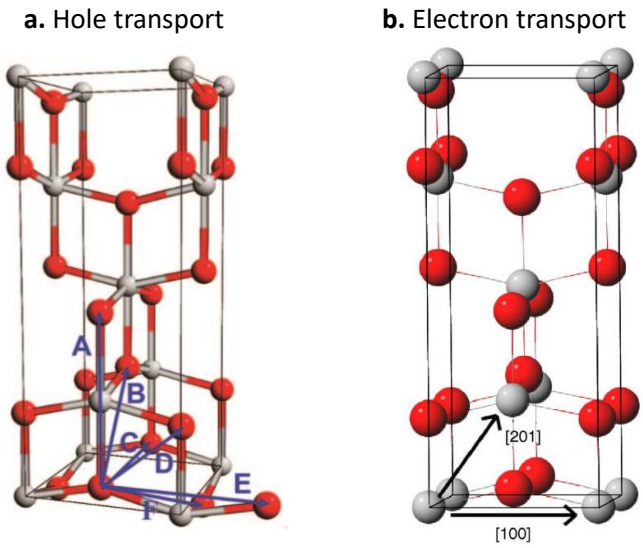

Figure 2.16 Anisotropy of (a) hole and (b) electron transport in TiO_2 anatase. The hole transfer marked D in panel a is several orders of magnitude faster than the others, while electron transport in the [201] direction is roughly five times more efficient than transfer in the [100] direction. Reproduced from [15, 16].

Lastly, there are several ways in which the size of a TiO_2 nanoparticle can affect the overall photoactivity. It has been suggested that smaller nanoparticles confine the electrons and holes into a smaller volume, increasing the rate of recombination [60, 84]. The particle size also affects the lattice strain and surface energy [85]. For instance, the abundance dangling bonds of the surface Ti^{4+} and O^{2-} species depends on the nanoparticle size. Since these features are known to trap electrons and holes, respectively, on the surface, the abundance and energy of these dangling bonds directly impacts the recombination rate and availability of charge-carriers at the surface [9].

Chapter 3. Experimental Methods

This chapter is meant to complement the experimental methods sections in each of the following three chapters. For the most part, those sections simply detail the experimental parameters, while assuming that the reader is already familiar with the experiments themselves. The chapter opens with a short introduction motivating the use of the vacuum environment and then describes both the theory and practice of the relevant techniques and their associated equipment.

3.1 Ultra-high vacuum environment

Catalytic surfaces exposed to air are often covered with molecules from the air. TiO_2 is particularly good at binding water molecules. If these contaminants are present during reactivity experiments, they may block the reagent from accessing the surface, they may influence surface reactions, and they may restructure the surface itself (e.g. oxidation). Thus a clean surface is a requirement for fundamental catalytic studies. Surface cleaning will be discussed later, but keeping a surface clean is only possible in a vacuum. Furthermore, many surface science techniques require a vacuum environment to operate. Therefore a well-maintained vacuum environment is the foundation for most surface science studies.

3.1.1 Gas behavior in high vacuum

The level of vacuum required to maintain sample cleanliness is determined by the rate at which gas molecules impinge on the sample surface. By making several simplifying assumptions (e.g. there are no long-range intermolecular interactions, average intermolecular separation is much larger than the diameter of the molecules themselves, etc.), the kinetic theory of gases can provide an estimate of this rate. In this framework, the speed and direction of each molecule is random, but the probability of having any given speed is determined by the Maxwell-Boltzmann distribution (which itself is based on statistical mechanics). Weighting this distribution by the velocity and integrating across all possible velocities gives the average speed for molecules in a gas (see equation 3.1). For a reference point, nitrogen molecules travel at an average speed of 470 m s^{-1} at room temperature.

$$v_{avg} = \left(\frac{8kT}{\pi m}\right)^{1/2} \qquad \textbf{3.1}$$

The rate at which molecules impinge upon a surface (i.e. the recently-cleaned sample) depends on density of molecules and on the component of the velocity normal to the surface. In other words, the molecules may be traveling in any direction, and those approaching the surface at a shallow angle contribute less to the total flux than those approaching along the normal vector. Integrating over all angles gives an average speed

towards the surface of one quarter of the average molecular speed. Multiplying this speed by the molecular density gives the flux towards a surface (equation 3.2).

$$\Phi = \frac{1}{4} v_{avg} \frac{n}{V} = \frac{P}{\sqrt{2\pi m k T}} \qquad \textbf{3.2}$$

Thus for a given temperature, the rate of impingement is proportional to the pressure. The flux can be used, together with the density of active sites on the surface (~5.2 x 10^{14} cm^{-2} for TiO_2, see section 2.1.2), to estimate the frequency of collisions with a single surface site. At ambient conditions, this happens on the order of nanoseconds, while there is roughly one collision per surface site each second at a pressure of 10^{-6} torr (this is the basis of the unit of surface exposure, the Langmuir). It is impossible to keep a sample clean for a reasonable amount of time in either environment. But in an ultra-high vacuum (~10^{-10} torr), a surface may be expected to remain clean for several hours.

The kinetic theory of gases also predicts the distance a molecule may travel, on average, before colliding with another molecule. This is called the mean free path. For air at ambient conditions, this distance is roughly 70 nm, which means that gas behavior is dominated by gas-gas collisions. This gives rise to many of the familiar properties of gasses, and allows gas to be treated as a continuum in many instances. On the other hand, in an ultra-high vacuum environment, the mean free path may be tens of kilometers, meaning that gas-gas collisions are negligible next to gas-wall collisions. This regime, which is called molecular flow, exhibits unfamiliar behavior. For instance, the

rate at which a gas flows through a long tube is proportional to the cube of the tube's radius for molecular flow (Knudsen equation) while it is proportional to the fourth power of the radius for laminar flow (Hagen-Poiseuille equation). Furthermore, if the molecular flow exits the tube into a larger volume, it does not expand uniformly in all direction as expected, but continues mostly in the same direction with some angular dispersion (shown in Figure 3.1). This presents a sense of anisotropy alien to common intuition about gas behavior. This means that line-of-sight, orientation are all important considerations when depositing reagents, modifying a surface, measuring pressure, and quantifying desorption products. For instance, a sample facing the opening by which reagents are admitted to the chamber will receive a much higher flux than (1) a sample facing away from the opening and (2) a sample facing the opening but positioned further away (since the molecular flow diverges a little upon entering the chamber). Similarly, the local pressure (or more properly, density) may vary throughout the vacuum chamber. Also, since desorption products are most likely to leave a surface closer to the normal direction,[5] the intensity of these products as detected by a mass spectrometer depends on the relative orientation and distance.

[5] Knudsen's cosine law states that the desorption flux in a given direction is proportional to $\cos(\theta)$, where θ is the angle between that direction and the surface normal.

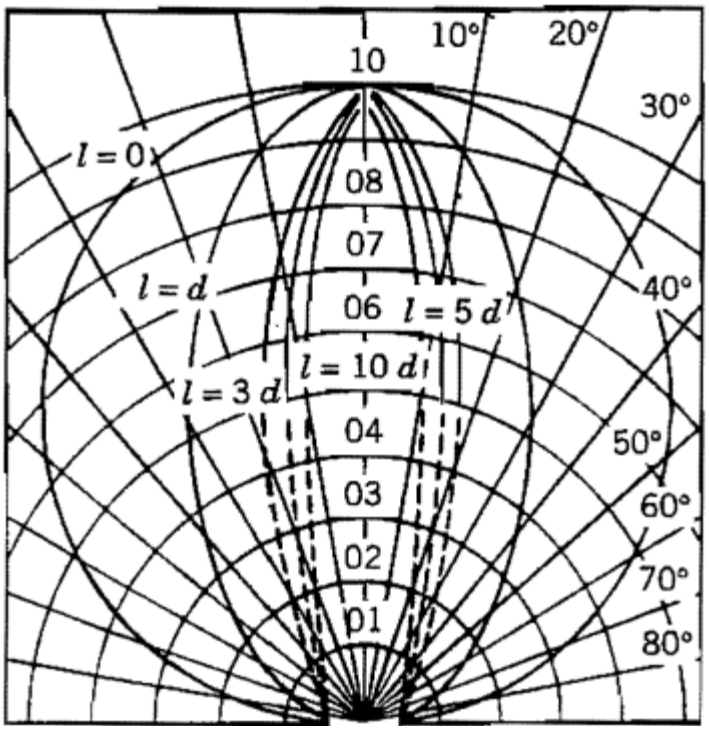

Figure 3.1 Angular distribution of molecular flow exiting a tube. The straight lines represent the angle from the axis of the tube and the concentric circles represent the relative flux (with the flux at 0° set to 10). Reproduced from [86].

3.1.2 Pressure measurement and management

The simplest pressure gauges (e.g. manometers, Bordon tubes) effectively measure the force applied at an interface, since pressure is simply force per area. However, this is not practical at lower pressures where the relevant forces are difficult to measure. Most methods of so-called pressure measurement in fact only measure the (number) density and report a calculated pressure. Nevertheless, vacuum scientists generally prefer to speak in terms of pressure instead of density.

One such method involves the rate of heat transfer away from a heated wire. Interestingly, the thermal conductivity of a gas is only a weak function of pressure under ambient conditions. The kinetic theory of gases predicts that the conductivity is a function of both the density and the mean free path of the gas. In viscous flow, a decrease in density is offset by an increase in the mean free path. Qualitatively, there are fewer gas molecules to carry heat, but each molecule will travel further. But as the pressure approaches the molecular flow regime, the mean free path is bounded by the dimensions of the vessel, so this model breaks down. In this transition region, the thermal conductivity is quite sensitive to the gas density. A thermocouple placed at the center of the heated wire can be used to indirectly measure the heat transfer rate in and therefore the pressure. However, heat may also transfer away from the wire by radiation or by conduction through its terminals. While these are minor contributors in a well-designed gauge, they are not a function of the pressure, and thus they will mask conductive transfer rates at very low pressures. This places a lower limit on the measurement range. In practice, these gauges, called thermocouple gauges, can only read pressures in the range of 10 torr to 10^{-3} torr. They are also not particularly accurate, although they are simple, durable, and resistant to contamination, which makes them well-suited for the environment of a dosing line (section 3.3.3).

Below the lower measurement limit of thermocouple gauges, the preferable method involves ionization of gas molecules. Electrons are ejected into the vacuum, where they may collide with a molecule and form a cation. Any such cations are collected and counted. For a given emission current, the collected ion current depends only on the

fraction of electrons which encounter molecules and the fraction of electron-molecule collisions that result in the creation of a cation. The former is clearly related to the gas density, and the latter depends on the composition of the gas. Thus an ionization gauge has different sensitivities for different species according to the corresponding ionization efficiencies, although these may often be neglected.

There are two types of ionization gauges relevant to this thesis and they are differentiated by the method of generating free electrons. A hot cathode ionization gauge contains a filament, usually W, heated resistively to the point where electrons have enough energy to overcome the work function (generally over 1000 K). This process is called thermionic emission. A Bayard-Alpert biases this filament at 30 V above ground and places it just outside of a cylindrical anode grid which is biased 150 V above the filament. A very fine current collection wire is located at the center of the grid and grounded. Emitted electrons are accelerated towards the grid. Most pass through and then accelerate back towards the grid, repeating until colliding with a gas molecule or the grid itself. Any cations formed within the cylindrical grid will be accelerated towards the collector. The current flowing out of the collector pin is used to calculate the gas density. The impact of electrons on the anode grid may cause two unwanted effects: (1) emission of x-rays which may strike the collector pin, which in turn may eject an electron giving the appearance of a cation collection and (2) desorption of species, including cations, from the surface of the grid wires, which will also count towards the measured pressure. While these effects are small (the switch from a large plate to a fine wire for current collection was done to reduce the number of x-ray impacts on the collector), they still

place a lower limit on pressure measurements. Hot cathode gauges are useful in the range of 10^{-5} torr to 10^{-11} torr, which makes them ideal for pressure measurement during normal operation of the ultra-high vacuum chamber, but they are susceptible to filament burnout at higher pressures. The other type of ionization gauge, the cold cathode ionization gauge, overcomes this limitation by replacing the hot filament with a cold (i.e. room temperature) cathode plate. This plate also serves the function of the hot cathode gauge's collector wire. The inverted magnetron variety of cold cathode gauge uses a cylindrical cathode with an anode pin biased several kilovolts above the cathode and located at the center. This assembly is placed in a strong magnetic field oriented such that free electrons travel in tortuous spirals, greatly increasing the path length and therefore the chance of encountering and ionizing a gas molecule. In normal operation, the impact of a cation onto the cathode, in conjunction with the strong electric field (~MV/m) ejects an electron which can create another cation upon collision with a gas molecule. On the other hand, production of free electrons during startup depends on field emission or on cosmic ray bombardment, which can be troublesome at lower pressures. The high pressure limit of operation is determined by the sputtering of the electrodes by ions. These gauges are usually used in the range of 10^{-3} torr to 10^{-8} torr. The side chamber of the apparatus used in these studies is equipped with an inverted magnetron gauge.

Just as pressure measurement in vacuum science requires a variety of gauges for different conditions and pressure ranges, several different types of pumps are used to set-up an ultra-high vacuum environment. Under normal operating conditions however, the ion pump alone is sufficient to maintain pressures as low as 10^{-10} torr. The operating

principle of this pump is quite similar to that of the cold cathode pressure gauge. In fact, ion pumps are capable of pressure measurements and ionization gauges are capable of pumping gases (albeit very slowly). Electrons are emitted from a cold cathode and forced to travel in spirals by static electric and magnetic fields at right angles. This increases the chance of collision with a neutral gas molecule which may create a cation. Any cations are accelerated towards a Ti cathode. The impact sputters away a bit of the cathode. When the sputtered Ti atoms are deposited back on a surface, they may (1) bury and trap any molecules adsorbed on the surface and (2) expose a clean Ti surface to which further gas molecules will strongly adsorb. Ion pumps generally consist of several pumping units, each of which contains a stainless-steel honeycomb anode placed between two planar Ti cathodes. These units are usually welded directly to the vacuum chamber and permanent magnets are fixed to the outside of the cells to create a ~0.1 T field within. A 5 kV potential is typical between the anode and cathodes. These pumps are very reliable (no moving parts) and are among the best in terms of ultimate pressure, but they cannot be started or run if the pressure is more than $\sim 10^{-6}$ torr. Many vacuum chambers also have a titanium sublimation pump. This is simply a heavy-duty filament made of a Ti-rich alloy. Resistive heating sublimates Ti from the surface of the filament, after which is will deposit on a surface and provide much of the same pumping actions as the ion pump. This pump is typically only used when the ion pump alone is insufficient, and even then it is used in short bursts (~30 s).

The task of pumping a vacuum chamber down to the point where the ion pump may be started usually falls to a combination of a roughing pump and a turbomolecular

pump. Turbomolecular pumps consist of an alternative series of rotor and stator blades similar to a jet turbine or axial compressor, but unlike those devices a turbomolecular pump is specifically designed to operate in the molecular flow regime. In other words, fluid behavior in an axial compressor may be analyzed in terms of pressure, but since individual molecules in molecular flow do not 'feel' pressure from the rest of the gas, an alternative framework is needed. When a gas molecule collides with a spinning rotor blade, it may scatter off the blade in any direction, but due to the momentum imparted by the blade, it is more likely to travel in the direction of the exhaust. This requires the distance between adjacent rotor and stator stages to be less than the mean free path of the gas. Thus a turbomolecular pump will not pump gas when the foreline pressure is above $\sim 10^{-2}$ torr and therefore must be backed by another pump. Nevertheless, they can achieve ultimate pressures in the range of 10^{-8} torr which makes them essential for pumping a vacuum chamber down in preparation for starting the ion pump and for pumping species which might otherwise negatively impact the ion pump, such as argon.

Roughing pumps are used to maintain a low foreline pressure for the turbomolecular pump. These are usually simple mechanical positive-displacement pumps. One of the more common variants is the rotary vane pump. These have a rotating cylinder inside a cylindrical pumping chamber. The axis of the rotating cylinder is parallel to that of the pumping chamber, but it is offset such that the cylinder is in contact with the inner wall of the chamber. The rotating cylinder has two vanes which may slide in and out of slots cut into the cylinder, but which are held against the inner wall of the pumping chamber by a spring. This effectively divides the pumping chamber into two

pockets which rotate along with the cylinder. As the off-center cylinder turns, the volume of each pocket expands near the inlet and then compresses near the outlet. All surfaces are coated in oil for lubrication and sealing. The ultimate pressure is limited to ~10^{-3} torr and they require more maintenance due to the metal-metal contact, but these pumps have the distinct advantage (among the pumps discussed here) of being able to operate with their exhaust at atmosphere pressure. They are used on their own to pump down dosing lines (section 3.3.3) and to provide differential pumping to the rotary motion manipulators (section 3.2.2), as well as backing the turbomolecular pump.

Finally, several procedures help to maintain vacuum by limiting outgassing (i.e. desorption of gasses from surfaces). When opening a vacuum chamber for maintenance or to change samples, water vapor adsorbs onto the inner walls of the vacuum chamber. This water will slowly desorb, preventing the chamber from reaching the very lowest pressures required for a traditional surface science study. This process is mitigated in two ways. Equalizing the pressure with dry nitrogen (drawn from a liquid nitrogen reservoir) before opening the chamber prevents the inrush of humid air. Additionally, when pumping the chamber down again, the entire vacuum chamber is heated to accelerate the outgassing process. This procedure, called a bake-out, usually brings the vacuum chamber to the order of 10^{-10} torr after about 16 hours. Various components (e.g. mass spectrometer filament, x-ray source filament, sample etc.) inside the chamber which may be heated during the course of experiments are often purposely outgassed after the bake-out but while the chamber walls are still warm. This prevents them from outgassing and degrading vacuum during experiments. Care is also taken to avoid introduction of foreign

substances which might outgas into the chamber. This is accomplished by wearing clean gloves when working inside the chamber or on any equipment which will end up inside, and by avoiding certain adhesives, lubricants, paint, plastics, and rubbers.

3.2 Sample preparation

3.2.1 Synthesis

The TiO_2 nanocrystals used in the reactivity studies of this thesis (Chapter 4 and Chapter 5) were synthesized by the Murray group in Penn Chemistry. This section will be limited to a summary of the key concepts and mechanisms involved. For a detailed description of the synthesis procedure, please see [87]. Ti was provided in the form of $TiCl_4$ and TiF_4 dissolved in 1-octadecene. A small portion of this stock solution is added to another 1-octadecene solution containing a surfactant, either 1-octadecanol or oleylamine. This mixture is rapidly heated to 560 K and held for 10 m to allow TiO_2 seed crystals to form. Then without cooling, additional stock solution is steadily introduced, growing the crystals. The entire process is carried out under an inert nitrogen atmosphere.

The nanocrystal shape is determined by the relative energies of the various exposed crystal planes. As discussion in section 2.1.2, the (101) plane of anatase has lower energy than the (001) plane, which means nanocrystals will tend to expose more {101} surface area than {001}. This leads to a roughly-bipyramidal equilibrium crystal shape, consisting of eight larger {101} facets and two small {001} facets in place of the points of the pyramids. However, lowering the energy of the (001) plane increases the

size of the {001} facets, resulting in a flatter platelet shape. Figure 5.1 shows both shapes side-by-side. Note that the underlying geometry is preserved in both cases. The {101} facets always make a 111° angle with the {001} facets. (In fact, this must be the case if each nanocrystal is a single crystal rather than a polycrystal containing multiple domains separated by grain boundaries.) So it would be more accurate to refer to this entire family of shapes as truncated bipyramids, each with various degrees of truncation, but for the sake of clarity the studies contained in this thesis use the term 'bipyramidal' to refer to the less-truncated shapes which are roughly twice as 'tall' (in the [001] direction) as they are wide and expose ~95% (101) surface area, and the term 'platelet' to refer to the more-truncated shapes which are ~4-5 times wider (in the [100] and [010] directions) than they are 'thick' (in the [001] direction) and expose ~65% (001) surface area.

Control over nanocrystal shape is achieved by controlling the presence of F during synthesis. F is known to stabilize the (001) surface relative to the (101) surface, therefore increasing the fraction of exposed (001) area. HF is released during synthesis by hydrolysis of the TiF_4 precursor. The concentration of F during synthesis can be moderated by the choice of cosurfactant. Oleylamine, which is a base, can act to quench HF as it is generated, reducing the F concentration, and by extension, the resulting (001) area. Therefore the choice of both cosurfactant and precursors (i.e. ratio of TiF_4 to $TiCl_4$) determines the nanocrystal shape. Results of several combinations are shown in Figure 3.2. Nanocrystal size is a controlled by varying the amount of stock solution added after the initial seed crystal formation, although longer synthesis duration tends to broaden the size distribution of the finished nanoparticles.

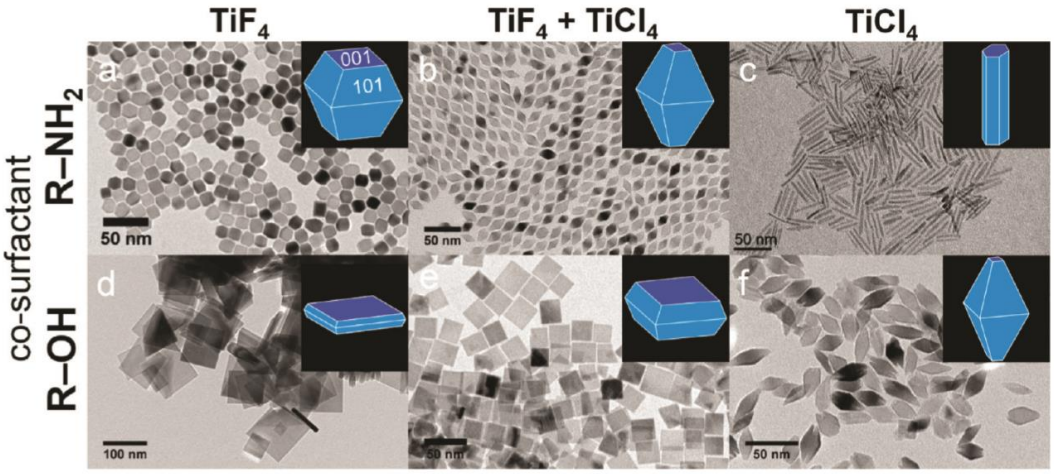

Figure 3.2 Effect of precusor and co-surfactant on nanocrystal morphology. Reproduced from [87]. The nanocrystal in panel b were studied in Chapter 4, while Chapter 5 introduces the nanocrystals in panel e.

After synthesis, a series of steps are taken to separate the nanocrystals from the cosurfactants, filter out the agglomerated particles, and remove the organic ligands. The resulting nanocrystals are suspended in hexane and spin-coated onto a 0.5 mm thick oxidized Si wafer. Spin coating results in a thin, uniform film of nanocrystals. This ensures the entire substrate will be covered, but the film will not be thick enough to cause chromatographic issues during temperature programmed desorption experiments. It also facilitates the use of surface science techniques and equipment designed with planar single-crystal samples in mind. The choice of an oxidized Si wafer as the substrate has several key advantages. (1) The thin SiO_2 overlayer is quite inert, which prevents it from contributing during reactivity experiments on the TiO_2. The Si bulk, however, has better (2) thermal and (3) electrical conductivity than a material such as Al_2O_3. Good thermal

contact between the nanocrystals and the substrate increases the accuracy of temperature readings, especially during a temperature ramp (i.e. TPD, see section 3.3), while good electrical conductivity helps to reduce sample charging during XPS (section 3.4). The wafer was then cut into rectangular samples ~7 mm across.

3.2.2 Temperature measurement and manipulation

The temperature of the sample is monitored by a type-K thermocouple affixed to the Si wafer using ceramic glue. Thermocouples make use of the thermoelectric effect, whereby thermal gradients induce electrical potential gradients, and vice versa. By using two wires made of materials with dissimilar thermoelectric properties, the same thermal gradient (between the sample and a reference cold sink) produces a different potential gradient along each of the two wires. Specifically, type-K thermocouples the alloys chromel, which has a response of 22 $\mu V\ K^{-1}$, and alumel, which has a response of -18 $\mu V\ K^{-1}$. Thus the two wires generate 40 $\mu V\ K^{-1}$ together [88]. The two wires are shorted at the sample (and only at the sample), which means that the thermal gradient can be calculated from the voltage between the ends of the two wires. Applying this thermal gradient to the known temperature of the reference junction gives the temperature of the sample. Of course this requires a constant, known temperature for the reference junction. In these types of studies, this is usually accomplished by immersing the chromel-Cu and alumel-Cu transition points in a reservoir of liquid nitrogen.

The sample is mounted in a holder cut from 0.025 mm Ta foil which is spot-welded to 0.25 mm Ta wires. Like the W used in ionization gauge filament (section

3.1.2), Ta is a refractory metal, which makes it fairly chemically inert and thermally stable. But unlike W, Ta has a lower yield strength [89], which makes it easier for clumsy graduate students to form into delicate shapes. These Ta wires are welded to larger 1 mm Cu wires which exit the vacuum chamber through ceramic feedthroughs (alongside the chromel and alumel thermocouple wires). The sample temperature may be increased by passing a current through this circuit. Resistive heating is mostly localized to the small-diameter Ta wires due to the increased current density. The Ta foil holder ensures this heat is spread evenly across the back face of the Si substrate, ensuring a uniform temperature across the nanocrystalline thin film on the front face. Conduction of heat through these same Cu wires to the liquid nitrogen reservoir (introduced in the previous paragraph) passively cools the sample. Temperature is controlled by a feedback loop subject to P-control during temperature ramps (e.g. during temperature programmed desorption, section 3.3) and PI-control during prolonged anneal treatments. Both control modules are written in VBA and executed by Excel, which interfaces with the thermocouple and the heater power supply via a Measurement Computing DAQ.

The flange through which the two heater wires and two thermocouple wires pass is not mounted in a fixed position, but rather placed at the end of a 4-axis manipulator. This allows the sample to be moved around the chamber and reoriented for various treatments and experiments without breaking vacuum (which necessitates a lengthy bake-out process, section 3.1.2). This manipulator actually consists of a Vacuum Generators single-axis rotary manipulator mounted onto a Thermionics three-axis manipulator. The three-axis manipulator has a flexible metal bellows with one end fixed onto the vacuum

chamber and the other end attached to a stage which is moved in three dimensions by worm screws. The use of a bellows means that all of the movement occurs away from the sealing surfaces which greatly reduces the leak rate. Such sealing surface movement is (nearly) unavoidable with rotary manipulators, however. In the case of the Vacuum Generators rotary manipulator, there are actually two o-rings spanning between an outer stationary cylinder and an inner rotating cylinder. The leak rate across one of these seals is roughly proportional to the pressure differential across the seal. The space between the two o-rings is continuously pumped down using a mechanical pump to mitigate leakage into the main vacuum chamber. This effectively maintains the main vacuum chamber at 10^{-10} torr even during movement of the manipulator.

3.2.3 Cleaning Procedure

Typically, metal and metal-oxide single crystals are cleaned by repeated cycles of Ar^+ sputtering and annealing. The sputtering process ejects atoms from the surface, with a slight preference towards lighter atoms. The annealing period allows the bulk atoms to re-form the lattice. Sputtering is quite efficient at removing coke or oxide layers from metal nanocrystals. Sputtering of metal oxides will result in reduction of the surface which can usually be reversed upon annealing in O_2. However, it is important to note that this process involves continual destruction and re-formation of the surface. This is not an issue for single crystals, but with nanocrystals this has a possibility to irreversibly alter the structure. The nanocrystals used in this study were instead annealed in pure O_2 for

extended periods of time. These treatments successfully remove F from the surface (leftover from synthesis, section 3.2.1) and greatly reduce the C content on the surface.

3.3 Temperature programmed desorption

Temperature programmed desorption (TPD) is a technique used to probe the adsorption energetics and reaction kinetics on a surface. It involves allowing a gas-phase reactant to adsorb onto a clean surface, then linearly ramping the surface temperature and monitoring the desorption products using mass spectrometry. The location, shape, and area of each desorption peak, as well as how these quantities change in response to varying adsorbate coverage, surface pre-treatment, UV exposure, etc., give information about the nature of the underlying adsorption and reaction mechanisms.

3.3.1 Theory

Surface-adsorbate interactions can generally be grouped into two categories: physisorption and chemisorption. Physisorption, or physical adsorption, results from Van der Waals forces between the adsorbate and the surface. This interaction is not chemically-specific (i.e. is not a strong function of the surface and adsorbate identities). Chemisorption, or chemical adsorption, involves the formation of chemical bonds between the adsorbate and the surface. Consequently, the binding energy is generally much stronger in a chemisorbed state (~1 eV) than in a physisorbed state (~100 meV) [90]. However, like any chemical reaction, chemisorption requires overcoming an

activation energy. This is depicted qualitatively in Figure 3.3. This barrier means that reagents are not guaranteed to chemisorb onto a catalytic surface, and in fact chemisorption sometimes requires specific sites on a surface. Note that in some cases the binding energy of physisorption may supply more than enough energy to overcome the activation energy, making this effectively a non-activated process.

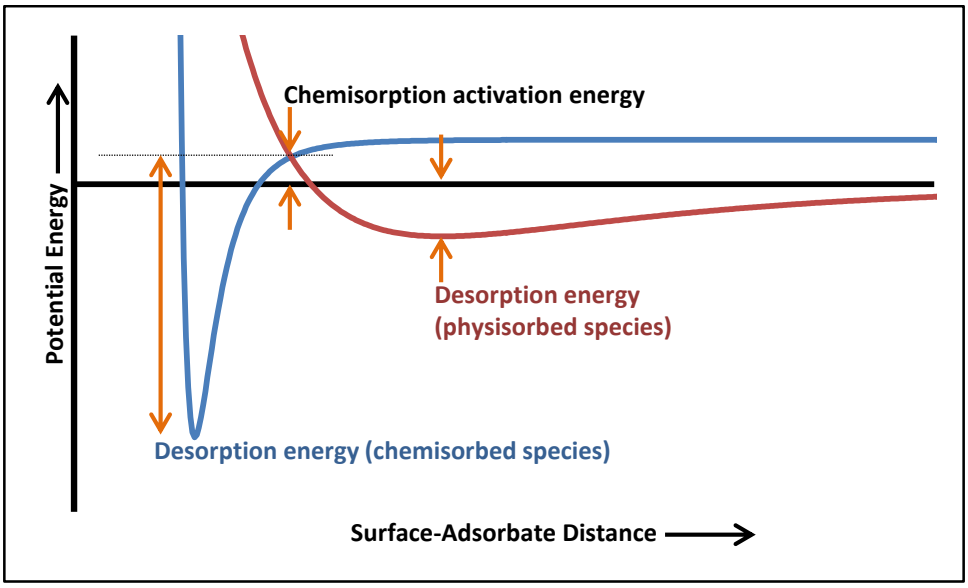

Figure 3.3 Adsorption energetics for (red) physisorption and (blue) chemisorption.

During a TPD experiment, physisorbed species generally desorb at or below room temperature due to their relatively weak binding energy, while chemisorbed species may remain adsorbed until elevated temperatures. One example of a physisorbed state is the multilayer formed when adsorbing more than a saturation dose of a reagent. These multilayers desorb in a sharp, narrow peak before the first layer desorbs (e.g. the left-most peak in Figure 2.4). In the case of oxygenate adsorbates such as alcohols and

carboxylic acids, chemisorption may involve dissociation into two or more fragments. For instance, methanol may dissociate upon adsorption on TiO_2 to form a methoxide group and a surface H. These dissociated species are much more stable on the surface which allows them to remain on the surface until the temperature is high enough to drive a reaction.

The relationship between adsorption energy and desorption temperature during TPD may be analyzed quantitatively. The rate of desorption is assumed to follow an Arrhenius form according to equation 3.3, where *m* is the reaction order. The temperature ramp rate can be used to rewrite the time derivative in terms of a temperature derivative, as is done in equation 3.4.

$$\frac{dN}{dt} = -k_d N^m = -A_d \exp\left(-\frac{E_d}{RT}\right) N^m \qquad \textbf{3.3}$$

$$\frac{dN}{dT} = -\frac{A_d}{\left(\frac{dT}{dt}\right)} \exp\left(-\frac{E_d}{RT}\right) N^m \qquad \textbf{3.4}$$

For a constant pumping speed, the partial pressure of a given species is directly related to the desorption rate of that species. This implies that the peak temperature is the point at which the desorption rate, given by equation 3.4, reaches a maximum. Thus the

adsorption energy may be related to the peak temperature according to equations 3.5 and 3.6 for first- and second-order desorption processes, respectively.

$$\frac{E_d}{RT_{peak}^2} = \frac{A_d}{\left(\frac{dT}{dt}\right)} \exp\left(-\frac{E_d}{RT_{peak}}\right) \quad \textbf{3.5}$$

$$\frac{E_d}{RT_{peak}^2} = \frac{2A_d N}{\left(\frac{dT}{dt}\right)} \exp\left(-\frac{E_d}{RT_{peak}}\right) \quad \textbf{3.6}$$

In practice, peak temperatures tend to be interpreted in a more qualitative sense, since there are many limiting assumptions behind the above analysis. For instance, it is assumed that desorption can be modeled as a single mechanistic step and that the activation energy of desorption is not a function of coverage, which is not always the case. Furthermore, the pre-exponential factor A_d is not known and must be assumed to be on the same order as the molecular vibration frequency. Nevertheless, this framework provides insight on desorption behavior. The peak temperature of a first-order desorption process is insensitive to adsorbate coverage; while a second-order desorption process will shift to lower temperatures with increasing coverage. Figure 3.4 shows typical TPD peak shapes and coverage-dependence.

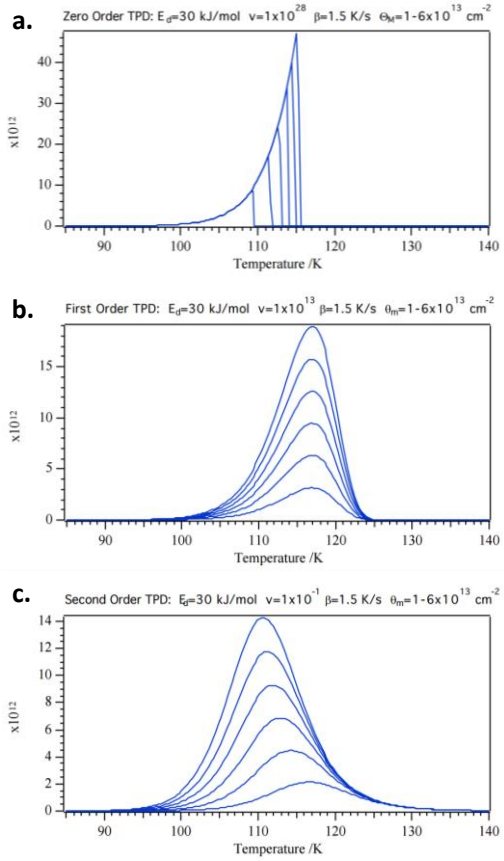

Figure 3.4 Simulated TPD peaks for (a) zero-order, (b) first-order, and (c) second-order processes. Adapted from [91].

3.3.2 Analysis

Mass spectrometers function by ionizing a molecule (which often leads to fragmentation) and then measuring the mass-charge ratio of the resulting ion fragments. To get meaningful information about the relevant chemical species, two major operations must be performed. First, the relative intensities of the various ion fragments are used to reconstruct the parent molecules which produced them. This is not always trivial, as a single fragment may derive from one of several different parent molecules. Each

molecule has an empirically-determined distribution of fragments, known as a cracking pattern. Thoughtful application of this knowledge allows one to determine the extent to which various chemical species contribute to each mass fragment's signal. A qualitative example of this process is shown in Figure 3.5. Note that the deconvolution process does not directly give information on the relative abundance of the various chemical species, only on their contributions to the various mass fragment signals. The second procedure involves using these mass signal intensities to calculate amounts of chemical species [92]. This step involves determining (1) the likelihood that a certain molecule will produce a certain mass fragment (based on the cracking pattern and on the ionization efficiency) and (2) the sensitivity of the mass spectrometer to that mass fragment. The sensitivity of a quadrupole mass spectrometer (section 3.3.3) to any given mass fragment is the product of the gain, which scales with the -½ power of the mass, and the transmission probability, which is constant for all fragments below 30 amu, then decreases more-or-less linearly for larger fragments.

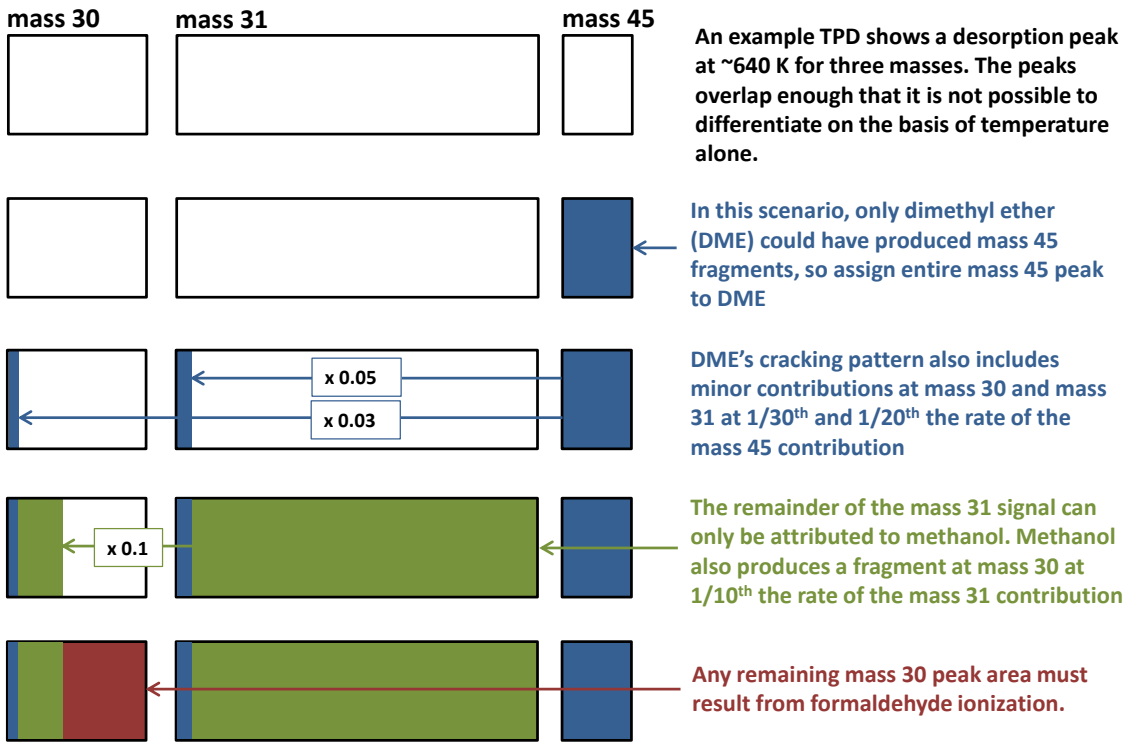

Figure 3.5 Qualitative mass spectrum deconvolution example.

The two-part procedure described above can be used to determine the relative concentrations of various chemical species based on the relative mass signal intensities. Note that obtaining absolute concentrations requires calibrating the mass spectrometer using a known concentration of a certain chemical species. But for most purposes, relative concentrations are sufficient. Evaluation of adsorption and reaction energetics relies only on the peak temperatures and shape. Reaction selectivity depends only on the relative peak areas. Knowledge of the absolute amounts of the relevant chemical species is only necessary when trying to determine the number of reactions per surface site (i.e. turnover) or number of reactions per absorbed photon (i.e. quantum yield), and TPD is not the ideal method for determining these quantities anyway.

Calculation of the yield of various reaction products gives information about the catalytic selectivity. Even in situations without any reaction, the areas of various desorption peaks give information on the relative abundances of the related adsorption states. As mentioned in section 3.3.1, the partial pressure of a certain chemical species at any given time is directly related to the rate of desorption for a fixed pumping speed. The yield of a chemical species is just the time-integral of the desorption rate; therefore the time-integral of the relevant mass fragment signal intensity gives the yield (after taking into account deconvolution and sensitivity factors). Since the temperature is ramped linearly in during a TPD, the temperature-integral of a mass signal is directly proportional to its time-integral (recall that TPD data is collected as mass signal vs. temperature). The conclusion is that one may directly integrate a TPD peak to obtain relative chemical yields without worrying about desorption rates, pumping speed, temperature vs. time, etc.

Sometimes it is also desirable to reduce the noise present in a TPD dataset. The simplest method involves a moving 'window' average, where each point is replaced by the average of itself and the surrounding points. However, this has the tendency to slightly flatten peaks. Also, the occasional, sharp noise spikes may be smeared into a small, broad peak. This is problematic because a sharp spike is obviously not a meaningful feature, but a small, broad peak may appear as a meaningful feature. Fourier smoothing (i.e. transforming a dataset into Fourier space, applying a low-pass filter, then transforming back) avoids both of these problems. Unfortunately, the process of transforming to and from Fourier space can introduce artifacts such as a series of small 'ripples' in the data. A third option involves fitting a polynomial around each point using

least-squares regression. The use of a polynomial allows this method to accurately capture peak shapes, which avoids the first problem associated with the window-average method. Of course it would be time-consuming to perform a least-squares regression for each point in the data. However, Savitzky and Golay [93] showed that the same effect may be achieved by simply convolving the dataset with a certain smoothing function (see Table 1 of [93]). This was the preferred method for smoothing TPD and XPS data for the bulk of this thesis.

3.3.3 Equipment

TPD experiments require (1) a mechanism for delivering pure, gas-phase reagent to the sample surface, (2) a method for linearly ramping the surface temperature, and (3) the ability to identify and quantify the desorption products. Temperature control was described in section 3.2.2. Analysis of mass spectrometer data was explained in the previous section, but a description of the mass spectrometer itself is included later in this section. First, however, the dosing mechanism will be described.

Dosing is the act of introducing reagents to the sample and allowing them to adsorb. Dosing quantities may be reported in terms of Langmuir (L) or monolayers (ML). The Langmuir is a unit of exposure equal to 10^{-6} Torr s. As discussion in section 3.1.1, the flux of a gas is proportional to the pressure. Therefore 1 second of exposure at 10^{-6} Torr is equivalent to 10 seconds of exposure at 10^{-7} Torr, which is reflected in the definition of the Langmuir. The monolayer is actually a unit of surface coverage. Determining this *a priori* requires knowledge of the sticking coefficient (i.e. probability

that an impinging molecule will adsorb) and the density of adsorption sites. If it is desirable to report coverages in terms of monolayers, a series of TPD experiments at increasing exposures will be used to determine the exposure at which the first adsorption layer saturates and the multilayer adsorption begins, and this number can be used to retroactively convert exposure (in L) to coverages (in ML).

Dosing is performed using a manifold which is maintained at a moderate level of vacuum (~10^{-2} Torr) by continuous pumping with a roughing pump. Liquid reagents are stored in glass vials attached to the manifold. Opening the valve between the manifold and the vial fills the manifold with the vapor pressure of that reagent. Gas reagents are stored in lecture bottles attached to the manifold. This manifold is connected to the vacuum chamber through a Varian variable leak valve. This valve allows precise control over the rate at which gasses inside the dosing manifold are admitted to the chamber (whereas most conventional valves have more-or-less binary control over flow). Dosing involves filling the dosing manifold with the relevant gas/vapor reagent, then slowly opening the variable leak valve to allow the reagent into the main vacuum chamber. Since the chamber is continuously pumped, the partial pressure of the reagent will quickly reach a steady-state value corresponding to ration of the leak rate to the pumping speed.

In order to allow for higher levels of exposure without flooding the vacuum chamber with the reagent, a dosing needle is installed on the UHV-side of the variable leak valve. The sample may be positioned directly in front of this end of the needle. Due to the behavior of gasses in high vacuum environments (section 3.1.1) the pressure at the

end of the needle will be considerably higher than elsewhere in the chamber (including the pressure gauge). This means that higher sample coverages may be attained without adversely affecting the cleanliness of the rest of the vacuum chamber, but it also means that the coverage calculated from the gauge-reported pressure underestimates the true coverage. Thus the calculated coverage is often multiplied by 'enhancement factor'. This factor depends on the relative arrangement of the dosing needle, sample, and pressure gauge, and on the pumping speed, but it can be estimated by comparing the coverage when dosing with the sample is directly in front of the dosing needle and when it is facing away from the needle.

Mass spectrometers work by using free electrons to ionize gas molecules, accelerate those ions through a filter, and then quantifying the remaining ions. The three sections shown in Figure 3.6, ionizer, mass filter, and detector, correspond to these roles. The ionizer consists of two filaments, which act as cathodes, encircling a cylindrical anode grid. Electrons are emitted from the filaments at a rate of 1 mA and are accelerated towards to anode grid, which is held at 70 V above the filament. Most electrons pass through the gaps in the grid. While within the anode grid, they may collide with a neutral gas molecule, ionizing it. Cations created this way are repelled by the high (positive) voltage of the anode grid and are accelerated into the mass filter. This is quite similar to the operation of the hot cathode ionization pressure gauge (section 3.1.2). In fact, an ionization pressure gauge is basically a mass spectrometer without the mass filter. However, the mass spectrometer often has a second cylindrical grid enclosing the filament-anode assembly. This grid, called the repeller, is at the same potential as the

filament and is meant to help contain electrons to increase ionization efficiencies and to prevent cross-talk with the pressure gauge.

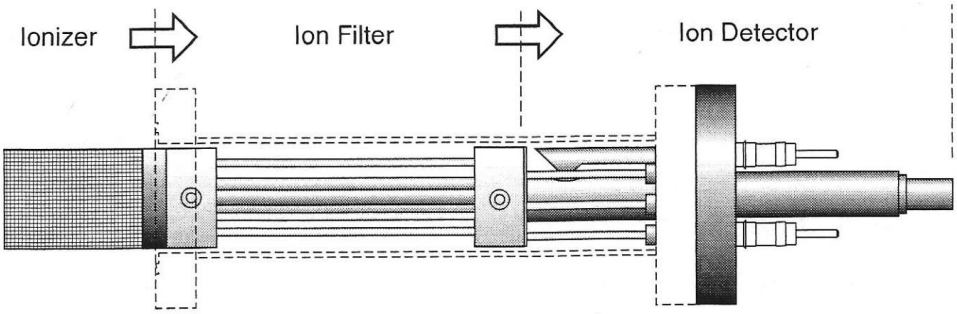

Figure 3.6 Schematic of a quadrupole mass spectrometer. Reproduced from [94].

The mass spectrometer used for the bulk of this thesis was a Stanford Research Systems quadrupole mass spectrometer. Its quadrupole mass filter uses electric fields to separate ions based on their mass-to-charge ratio. The filter consists of two pairs of parallel cylindrical rods (hence 'quadrupole'). One pair of rods has a positive DC bias which serves to keep the cations centered in the middle of the channel. On top of this bias is a high-frequency AC voltage which periodically perturbs ions away from the center of the channel. All singly-ionized cations experience the same force, but the resultant acceleration depends on the mass of the ion. This means that lighter ions are more susceptible to these perturbations than heavier ions, so their trajectory will deviate more and more from the center of the channel until they collide with one of the rods. Thus this pair of rods effectively serves as a high-pass mass filter. The other pair of rods has a negative DC bias which draws the cations away from the center of the channel (closer to

a collision with the rods). These also have a high-frequency AC voltage on top of the DC bias, but in this case the periodic perturbations work to push the ions back towards the center of the channel. The heavier ions are less susceptible to the perturbations, and eventually succumb to the pull of the DC bias, colliding with the rods. Thus this pair acts as a sort of low-pass mass filter. Together, the quadrupole serves as a band-pass filter. Varying the ratio of the RF and DC voltages allows for control of the band position. Ions which remain near the center of the channel will pass through the length of the mass filter and reach the detector.

The mass spectrometer used in this thesis was equipped with two detectors. The first detector, the Faraday cup, is analogous to the current collector pin of the ionization pressure gauges (section 3.1.2). It simply measures the current of the impinging cations using a high-precision electrometer. However, this is not sensitive enough for use below ~10^{-9} Torr. At UHV conditions, the electron multiplier it typically used. This type of multiplier, called a continuous dynode electron multiplier, has a very low work function and is held at a highly negative voltage. The impact of an ion results in the ejection of several electrons from the surface, similar to the mechanism of electron emission in a cold-cathode pressure gauge (section 3.1.2). These electrons are drawn towards the CDEM anode, but due to the geometry of the multiplier, most will collide with the surface again, resulting in the ejection of even more electrons. Under typical operating conditions, a single ion impact at the front end of the CDEM results in ~10^{7} electrons reaching the detector. This allows for accurate measurements even below 10^{-10} Torr.

VBA code running in Excel is used to control the temperature ramp (see section 3.2.2) and to continually cycle the mass spectrometer through a pre-selected list of masses. The resulting mass fragment signal intensities are paired with the temperatures at which the readings were taken.

3.4 X-ray photoelectron spectroscopy

X-ray photoelectron spectroscopy (XPS) is a technique which is used to probe the chemical structure (i.e. composition and oxidation state) of a surface and even adsorbates. X-ray photons absorbed by a surface generate free electrons with energy characteristic of the surface composition. Since both x-rays and electrons cannot travel very far in a solid before interacting with it, XPS is a surface-sensitive technique. This means that information is gathered on the first few nanometers of a material, rather than on the entire bulk.

3.4.1 Theory

XPS draws information about the electronic structure of a surface by use of the photoelectric effect. It was known since the late 19th century that certain metals will eject electrons under illumination by high-frequency light. Albert Einstein first explained this effect in terms of what we now call quantum mechanics (earning him the Nobel Prize in Physics in 1921). Basically, each photon has a fixed energy based on its frequency. Above a certain frequency (UV-range and higher for most metals), this energy exceeds

the potential energy binding the electrons to the metal, allowing an electron to leave the metal surface upon photon absorption.

Conservation of energy dictates that the kinetic energy of the ejected electron (which can be measured) must be equal to the energy of the absorbed photon (which is known) and the binding energy of the recently-ejected electron (see equation 3.7). Technically, the term 'binding energy' is used to refer to the difference in potential energy between the electron orbital and the fermi level, while the work function refers to the difference between the fermi level and the vacuum level. So ejecting an electron from a surface requires overcoming the sum of the orbital binding energy and the work function. The work function (denoted as Φ in equation 3.7) is only dependent on the material, while each electron energy level has a unique binding energy. For instance, the Si 2p orbital has a binding energy of 103 eV while the 2s orbital has a binding energy of 153 eV [95]. Furthermore, the exact binding energy of each of these orbitals depends strongly on the identity of the atom, and weakly on the oxidation state of that atom. The $2p_{3/2}$ feature has a binding energy of 454 eV for Ti^0, 459 eV for Ti^{4+}, and 512 eV for V^0 [95]. Since the binding energy is constant for a given element and oxidation state, but the kinetic energy depends on frequency of the x-ray source, XPS data are presented as photoelectron intensity as a function of binding energy, rather than as a function of kinetic energy. However, since kinetic energy is the directly-measured quantity, it is not unusual to see XP spectra which preserve the orientation of the kinetic energy axis (i.e. binding energy decreasing to the right).

$$E_{binding} = h\nu - E_{kinetic} - \Phi \qquad \textbf{3.7}$$

Photoelectron features which originate from orbitals with non-zero angular momentum quantum number (i.e. *p, d, f,* etc.) actually appear as a pair of closely-spaced peaks. This phenomenon is called 'peak splitting'. It is due to a quantum mechanical phenomenon called 'spin-orbit coupling'. Conceptually, the spin of an electron may either align with the local magnetic field or against it. This has a small but measurable effect on the binding energy.[6] For instance, the 2p orbital of Ti^0 gives rise to two features: $2p_{3/2}$ at 453.8 eV and $2p_{1/2}$ at 459.9 eV [95]. The relative areas of each peak depend on the degeneracy of the underlying quantum states, but luckily it follows a simple pattern. The ratio of the low binding energy peak to that of the high binding energy peak is 2:1, 3:2, and 4:3 for the *p, d,* and *f* orbitals [96].

Each peak in a XP spectrum usually corresponds to a specific orbital. In other words, the peak consists of photoelectrons which only lost energy to the work function and orbital binding energy. However, photoelectrons can also lose energy through inelastic collisions on their outward trajectory. This energy loss will give the appearance of higher binding energy. If these loses are random, they will manifest as a featureless increase in the photoelectron intensity at binding energies higher than the peak (compare the baseline level on both sides of the peak in Figure 3.7). In special circumstances, however, photoelectrons may be more likely to lose a specific amount of energy, for

[6] This is somewhat analogous to the Zeeman Effect in which a large, external magnetic field splits the energy levels of otherwise-indistinguishable states. Techniques such as NMR make use of this effect.

instance through collisions with valence electron from the same atom (i.e. ‘shake-up’) or through by interacting with plasmons. Both of these events may result in smaller but well-defined peaks at energies above the primary peak. These peaks can be useful in aiding surface characterization. For instance, the XP spectrum for Ce contains many overlapping peaks, but there is an isolated shake-up feature at 915 eV which is solely attributable to Ce^{4+} [95]. While the above artifacts are the result of photoelectrons losing energy before reaching the detector, there is another class of electrons which can produce features on an XP spectrum. When a core-level electron is ejected from an atom, it is possible for the vacancy to be filled with an electron from a higher-energy orbital. The energy gained by this second electron upon descending deeper into the potential well can be transferred to a third electron. Sometimes, especially in lighter elements, this third electron has enough energy to leave the material entirely. This electron is called the Auger electron. Note that the kinetic energy of the Auger electron is independent of the incident photon energy, yet XP spectra are plotted as a function of binding energy (which depends on the photon energy). This means that the position of an Auger feature in an XP spectrum depends on the type of x-rays used.

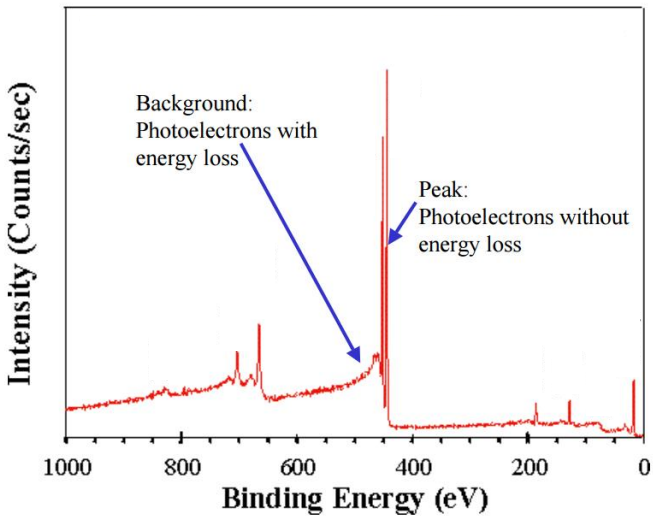

Figure 3.7 Example XP spectrum showing the uneven baseline due to photoelectrons' inelastic collisions. Adapted from [97].

The process of ejecting photoelectrons from a surface results in an excess of positive charge. This is neutralized by current from the rest of the sample, which in turn will draw from the sample mounting, and eventually from ground (assuming the sample has been properly grounded). For conductive samples, the charge neutralization is so efficient that there is no measurable bias at the surface. However, insulating or semiconductor surfaces may experience a considerable steady-state bias. This positive voltage will decelerate electrons leaving the surface, lowering their kinetic energy and therefore overestimating the binding energy across the spectrum. As long as the charging is on the order of ~1 V, a constant shift may be applied to the entire spectrum such that a reference peak appears at the expected position.

3.4.2 Analysis

As mentioned above, the position of an XPS peak indicates the presence of a certain atom on the surface. The peak area is related to the relative abundance of that atom (although the sensitivity varies according to the element and orbital). So in the absence of overlapping features, the peaks may be integrated numerically to obtain peak areas and the peak position may be taken to be the highest point of the peak. However, in the case of partially-reduced oxide samples, there may be many overlapping peaks. For instance, the difference in binding energy between the $2p_{3/2}$ feature for Ti^{4+} and Ti^{3+} is only 1.7 eV [95], which about the same as the peak width in a typical system. In such cases it is best to fit peaks to the data.

Before fitting any peaks to the data, however, the influence of the inelastically-scattered electrons (see Figure 3.7) must be removed. The main contribution from these scattered electrons is a rise in the baseline intensity from the lower-binding-energy to the higher-binding-energy side of the peak. This baseline must be subtracted from the signal before any meaningful quantification of the peak may be attempted. Figure 3.8 illustrates various baseline models. The step change and linear baseline models are clearly the simplest. The last model, called the Shirley Background, must be calculated iteratively based on the shape of the peak (whereas the step change and linear baselines only depend on the two end points), but it more accurately captures the true baseline behavior.

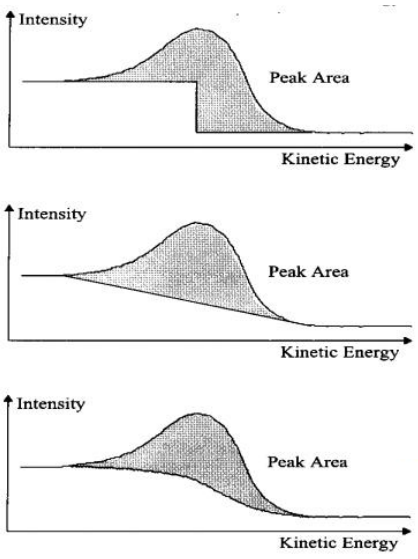

Figure 3.8 Several models for estimating the baseline under an XPS peak. Adapted from [97].

Due to the uncertainty principle, there is some inherent uncertainty in the product of energy and time. Since the excited state in a photoemission process does not last an infinite amount of time, there is some non-zero uncertainty in the energy of that state. This gives rise to a Lorentzian peak shape [96] rather than a zero-width feature. This intrinsic line-width is further broadened by relativistic Doppler shift due to vibrations and the limited resolution of XPS equipment, both of which can be modeled as Guassian functions. Therefore it is common to use a Gaussian-Lorentzian combined peak shape when fitting XPS peaks. Dedicated analysis software is able to fit multiple, overlapping peaks (such as in Figure 3.9), which can give detailed information on the amount of material in any given oxidation state.

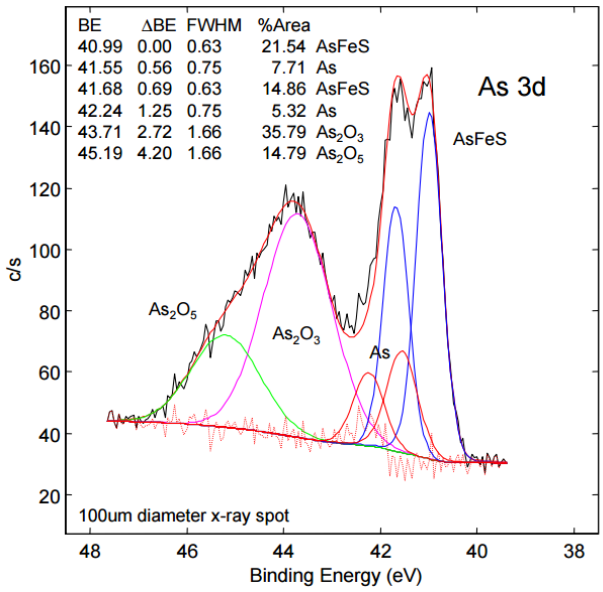

Figure 3.9 XPS peak fitting example. The baseline model is shown in bright red. Reproduced from [97].

Direct quantification of different components is complicated by the fact that the intensity of any given peak depends not only on the abundance of the corresponding chemical species, but also on the inherent sensitivity of that particular photoemission event and on the depth of that species. Elemental sensitivity is well-documented, but a non-uniform depth profile is non-trivial. For instance, if two signatures are detected, one strong and one weak, it would be quite difficult to determine if the weaker signature belongs to a minority species present throughout the sample, or to a high concentration of that species buried 1 nm beneath the surface. Therefore conclusions about composition often rely on an assumed depth profile. However, collecting photoelectrons from very shallow angles to the surface (rather than normal to the surface) effectively selects against photoelectrons generated from deeper within the material. This makes the

technique even more surface sensitive, and can help build a depth profile. This variation is called Angle-Resolved XPS and is often used to measure the thickness of oxide layers.

3.4.3 Equipment

XPS experiments require an x-ray source and a spectrometer to analyze the energy of the ejected photoelectrons. The x-ray source used in this thesis was an Al-Mg dual-anode source. Each anode has its own filament serving as its cathode, although only one is active at time. As with the hot cathode filaments in the ionization pressure gauge (section 3.1.2) and the mass spectrometer (section 3.3.3), these filaments thermionically emit free electrons (typically at a rate of ~15-20 mA). These electrons are accelerated towards the corresponding anode, which is held at 15 kV above the filament. The impact of the 15 keV electrons produces significant heating, so the anodes are water-cooled. These electrons are energetic enough to eject electrons from the 1s orbital of the Al and Mg atoms. When another electron from that atom moves from a higher-energy orbital to fill the 1s vacancy, the amount of energy released is sufficient to produce an x-ray photon. The wavelength of the photon depends on the specific transition made by the electron filling the vacancy; therefore several different wavelengths can be produced. The strongest emission is the K_α line[7] at 1486.7 eV for Al and 1253.6 eV for Mg, which is produced when a 2p electron fills a 1s vacancy. These features have a line-width of 0.85 eV and 0.7 eV for Al and Mg, respectively [97], which is due in part to the fact that they are actually closely-spaced doublets arising from the same minute energy level splitting

[7] In x-ray notation, the 1s orbital is denoted by 'K', and α signifies a one-shell transition (i.e. $2 \rightarrow 1$).

discussed in section 3.4.1. The width of these emission features contribute to the overall XPS peak-width.

The spectrometer used in these studies was a hemispherical electron energy analyzer. These spectrometers contain two concentric hemispheres with the inner hemisphere held at a higher (more positive) potential than the outer hemisphere, causing electrons in the space between the hemispheres to accelerate towards the center of curvature. The trajectory of the electron, therefore, depends on its initial velocity. The inertia of the faster electrons means they will strike the outer hemisphere, while slower electrons will be drawn into the inner hemisphere. Only electrons with a narrow range of kinetic energies will traverse the channel between the two hemispheres and exit through a narrow aperture on the way to the detector. The resolution, i.e. the range of kinetic energies which are admitted to the detector at any given moment, is related to the aperture width, radius of curvature of the hemispheres, and the nominal kinetic energy according to equation 3.8, where ΔE is range of admissible energies.

$$\frac{\Delta E}{E} \sim \frac{w_{aperture}}{R_{hemisphere}} \qquad \textbf{3.8}$$

In principle, the position of the pass band can be adjusted by controlling the voltage between the two hemispheres. However, it is desirable to have a constant resolution throughout an XP spectrum. According to equation 3.8, this would require changing the width of the aperture along with the voltage. Unfortunately, narrowing the

aperture decreases the signal-to-noise ratio, which is also undesirable. Instead, it is simpler to fix the both the voltage between the hemispheres to only transmit a fixed electron energy, called the pass energy. A retarding grid placed at the entrance to the spectrometer makes up the difference between the electron energy of interest and the pass energy. In other words, electrons with the desired kinetic energy are slowed by the retarded grid such that they have the appropriate energy to pass through the spectrometer. This method preserves the absolute resolution and the signal-to-noise ratio throughout a spectrum. It has the additional advantage of maximizing the resolution for a given radius of curvature and aperture width by working with lower electron energy (typical pass energies are on the order of ~5-20 eV).

As with TPD experiments (section 3.3.3), VBA (running in Excel) is used to step the spectrometer through a user-determined range of electron energies, and to match to the resulting photoelectron intensities, measured in counts per second, with the corresponding binding energies. Due to low signal-to-noise ratios, it is common practice to scan a narrow range of binding energies multiple times and average the signal intensity at each point.

3.5 UV exposure

The band gap of TiO_2 anatase is ~3.2 eV. This corresponds to ~385 nm light, which is just past the end of the visible spectrum. Therefore it is necessary to illuminate the sample with UV light to drive photocatalysis. This thesis used a LED UV source which produces light at a nominal wavelength 365 nm. LED sources are generally much

less powerful than Hg arc lamps, but they produce only a very narrow range of light which eliminates the need for IR filters.

The LED source is designed to focus the light onto the tip of an optical fiber. This allows the source to remain outside the vacuum chamber, while the light is passed into the chamber through a fused silica optical fiber. The sample is positioned directly in front of the end of the cable at a distance of 1 cm to ensure the entire sample was illuminated. (This was verified visually, as the tail end of the source's spectrum reaches far enough into the visible range to be seen as a very faint blue.) The photon flux as measured by a Thorlabs photodiode sensor is 1.0×10^{15} cm^{-2} s^{-1}. Unfortunately, the light lost to reflection and scattering could not be easily quantified.

The sample was held at 160 K during illumination to prevent desorption of weakly-bound surface species and to minimize sample heating from the absorbed light that might accelerate non-photochemical reactions. Any effects from sample heating might be mistakenly interpreted as photocatalytic effects, thus maintaining a constant sample temperature through the UV exposure is essential.

Chapter 4. Thermal and Photochemical Reactions of Methanol on Nanocrystalline Anatase TiO_2 Thin Films[8]

Summary

The publications in this chapter and in Chapter 5 resulted from a collaboration with members of the Chris Murray lab in the Chemistry Department. This study featured three sizes of the bipyramidal anatase nanoparticles. It was first and foremost a demonstration that traditional surface science techniques can yield structure-activity relationships from thin films of well-defined nanocrystals. The impact of nanoparticle size on several catalytic and photocatytic processes was documented and active sites were proposed for two of the reactions.

[8] This chapter was published as **Bennett, D. A.**; Cargnello, M.; Gordon, T. R.; Murray, C. B.; Vohs, J. M., *Phys. Chem. Chem. Phys.* 17 (2015) 17190-17201

4.1 Introduction

Surface science studies employing single crystals of metal oxides as model catalysts have provided considerable insight into the complex relationships between surface structure and reactivity for these materials [3, 20, 98, 99]. The site requirements for specific reactions, especially those involving simple oxygenates, have also been determined for a range of metal oxide single crystal surfaces. While this body of work has been very insightful, questions still remain as to how the results obtained from macroscopic single crystals can be used to understand and predict the reactivity of the more complex, high surface area polycrystalline metal oxide powders that are typically used as catalysts and photocatalysts in industrial processes. This issue is often referred to as the "materials gap" between studies of model single crystal and high surface area catalysts. On oxide surfaces highly undercoordinated metal cations are generally the active sites and in many cases such sites are associated with defects (e.g. oxygen vacancies) and surface reconstructions. The complex environments for both cations and anions on oxide surfaces also make the materials gap a more significant issue for oxides than it is for metals.

In recent years studies focused on bridging the so-called materials gap have started to appear in the literature in which well-defined oxide nanocrystals or nanostructured films have been used as model catalysts [100-108]. As a prototypical example, Mann et al. [107] have studied the reaction of acetaldehyde on CeO_2 nanocrystals with well-defined surface crystallographic orientations, showing that different facets possess very different reactivity, a knowledge that is critical in preparing

more active and selective systems. While many aspects of the reactivity of these nanomaterials could be correlated with results obtained from single crystal surfaces, some shape dependencies were observed which were attributed to structure-related variation in defect density, surface oxygen coordination, and vacancy formation energy.

In the work described here we study the thermal- and photochemical reactivity of well-defined anatase TiO_2 (A-TiO_2) nanocrystals with tunable size and morphology and have compared this reactivity to what has been reported for macroscopic single crystals. A-TiO_2 was chosen because it is active for both the thermal [8, 14, 27, 31, 43, 53] and photochemical [9, 76] oxidation of organic molecules. While there is extensive literature for these reactions taking place on rutile TiO_2 (R-TiO_2) [6, 11, 29, 35, 59, 65, 67, 68, 72, 75, 78], methanol was chosen as a probe reactant because it undergoes a range of crystal-plane dependent reactions on TiO_2, including complete and partial oxidation, and bimolecular coupling [6, 8, 9, 27, 35].

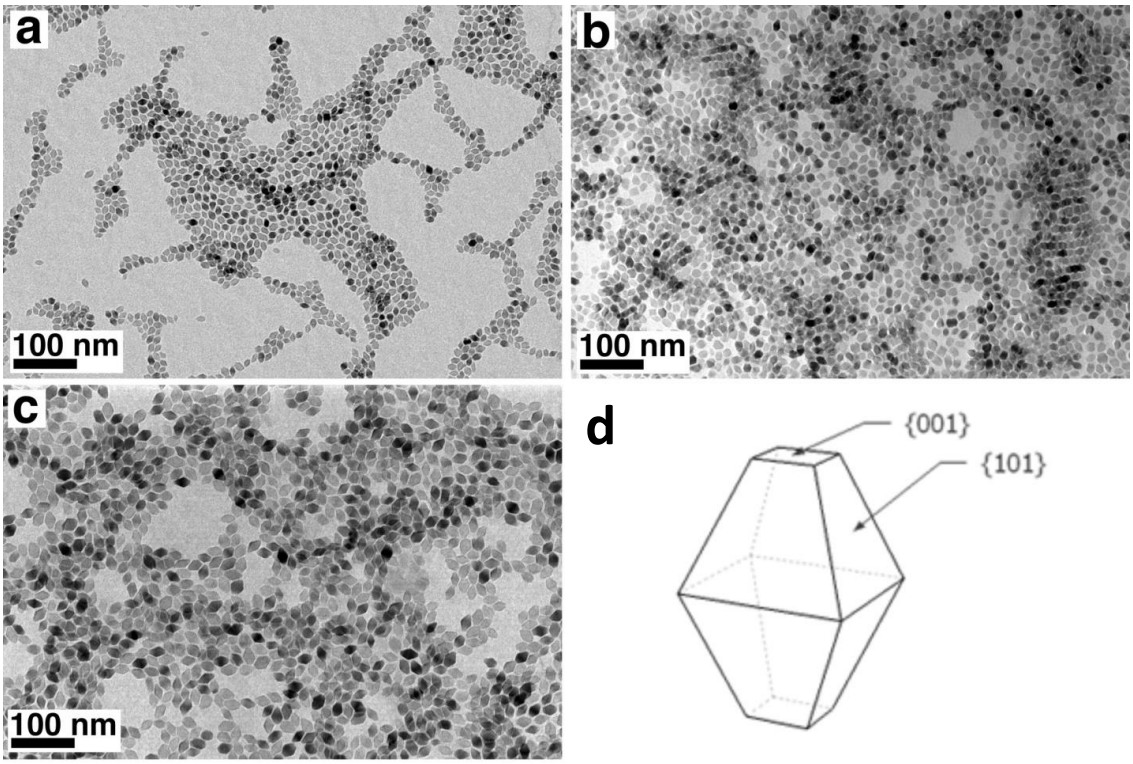

Figure 4.1 TEM micrographs of as-synthesized (a) 10 nm, (b) 18 nm, and (c) 25 nm A-TiO_2 nanocrystals. (d) Schematic showing the shape of the nanocrystals and the exposed crystal planes.

The A-TiO_2 nanocrystals employed in this study had a truncated, bi-pyramidal shape as shown in Figure 4.1. This shape is close to the equilibrium shape expected for anatase [87, 109, 110]. As shown in the figure, the nanocrystals expose eight {101} surfaces and two {001} surfaces, with the former accounting for the majority of the surface area.

4.2 Materials and Methods

TiO_2 nanocrystals were synthesized as described by Gordon et al. [87]. Briefly, a stock solution of TiF_4, $TiCl_4$, and oleic acid in 1-octadecene was added to a cosurfactant (oleylamine or 1-octadecanol) at 333 K and then heated to 563 K. The mixture was held at this temperature for 10 minutes allowing A-TiO_2 seed crystals to form then additional stock solution was continuously added facilitating continued growth of the crystals. The nanocrystal shape was determined by the choice of cosurfactant and the ratio of TiF_4 to $TiCl_4$ in the stock solution. The nanocrystal size was varied by injecting either 4, 8 or 12 mL of Ti stock solution into the seed solution. As will be shown below, this procedure produced crystals with a uniform truncated, bi-pyramidal shape (see Figure 4.1d) and a very small size distribution. Nanocrystals with lengths (long axis) of 10, 18, and 25 nm were used in this study. Detailed characterization data for the nanocrystals, including x-ray diffraction, N_2 adsorption, and TEM have been reported previously by Gordon et al.[87]

To facilitate ultra-high vacuum (UHV) reactivity studies, the resulting nanocrystals were spin-cast from hexane solution (~50 mg mL^{-1}) onto 8 x 6 x 0.5 mm oxidized, single crystal Si substrates. These thin film samples were then mounted in Ta foil holders that were spot-welded to an electrical feedthrough on the sample manipulator of the UHV chamber. Sample heating was accomplished by conduction from the resistively heated foil holder, and cooling was accomplished by conduction from a liquid nitrogen reservoir outside the chamber. The sample temperature was measured using a type-K thermocouple that was attached to the back of the Si substrate using a ceramic

adhesive (Aremco). Care was taken to ensure the thermocouple was not in contact with the Ta foil sample holder.

All reactivity experiments were conducted in an UHV chamber with a base pressure of 2 x 10^{-10} Torr. The chamber was equipped with a hemispherical electron energy analyzer (Leybold-Heraeus) and X-ray source (VG Microtech) for X-ray photoelectron spectroscopy (XPS) and a quadrupole mass spectrometer (Stanford Research Systems) which was used for temperature programmed desorption (TPD). The UHV chamber was also equipped with a fiber optic feedthrough and cable that allowed UV light from a 365 nm LED source (Prizmatix) to be directed at the surface of the sample. Photon flux at the sample surface was 10^{15} cm^{-2} s^{-1} as determined using a photodiode detector (Thorlabs). UV illumination was always carried out with the sample held at 160 K. *In situ* sample cleaning by Ar^{+} sputtering was not practical, since preserving the morphology of the nanocrystals was of central importance. Instead, cleaning was accomplished using oxidation treatments consisting of annealing each sample in oxygen (10^{-8} Torr, Matheson, 99.997%) at 700 K.

HPLC grade methanol (Fisher Scientific) was used as the reactant in the reactivity studies and was further purified by repeated freeze-pump-thaw cycles prior to use. The methanol was contained in a glass tube that was attached to a dosing manifold that allowed it to be introduced in the vacuum chamber using a variable leak valve and a directional dosing needle. Unless noted otherwise, the sample was held at 160 K during dosing.

During TPD experiments the sample temperature was ramped at a rate of 3 K s^{-1}. The following m/e values were used to monitor desorption products: 2 (H_2), 16 (CH_4), 18 (H_2O), 30 (CH_3OH and CH_2O), 31 (CH_3OH), 45 ($CH_3OCH_{3)}$, and 60 ($HCOOCH_3$). All TPD data were corrected for mass spectrometer sensitivity factors and overlapping cracking patterns for the various desorption products. To account for differences in surface area between the samples, the data was also normalized to the amount of molecular methanol desorbed for saturation methanol coverage. Since in all cases only a small fraction of the adsorbed methanol reacted to produce products (< 5%), the amount of methanol adsorbed at saturation provides a good approximation of the surface area. X-ray photoelectron spectra (XPS spectra) were collected using an Al(Kα) x-ray source and the energy scale in each spectrum was referenced to the O(1s) peak which was set at 531.6 eV.

All scanning electron microscopy (SEM) experiments were performed on a JEOL 7500F HRSEM operating at 5 kV in secondary electron imaging mode. The SEM images presented in the current study depict the nanocrystalline thin-films used in reactivity studies with no modifications aside from the addition of conducting tape to reduce sample charging. Transmission electron microscopy (TEM) characterization was performed using a JEOL JEM1400 TEM operating at 120 kV after dispersing the nanocrystals onto a 300 mesh carbon-coated copper TEM grid.

4.3 Results

4.3.1 Characterization of the A-TiO_2 Nanocrystals and Thin Films

Representative TEM images of the as-synthesized uniform A-TiO_2 nanocrystals are displayed in Figure 4.1a-c and show the truncated bi-pyramidal shape of the nanocrystals. The nanocrystal long axis was 10, 18 and 25 nm, respectively. Figure 4.2 shows an SEM image of a typical, freshly-prepared 18 nm crystallite spun cast, thin film sample. The film contains several layers of nanocrystals that are randomly oriented and the truncated bi-pyramidal shape of the nanocrystals is again readily apparent. Statistical analysis of particles in the image that have their long axis parallel to the substrate gave an average particle size of 14 nm ± 1.5 nm, which is in good agreement with the more accurate TEM measurement of the size of the as-synthesized particles. SEM was also used to characterize an 18 nm TiO_2 nanocrystal film that had been subjected to multiple cycles of heating to 850 K and then cooling to room temperature or below in UHV. As would be expected for this temperature range, sintering of the particles was not observed and they maintained their truncated bi-pyramidal morphology.

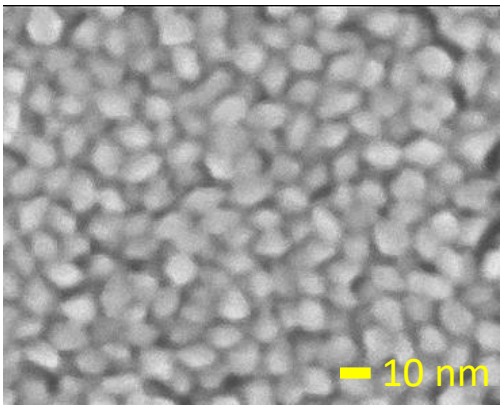

Figure 4.2 SEM images of an 18 nm A-TiO2 nanocrystal thin film on an oxidized silicon substrate.

XPS was also used to characterize the surface composition and the oxidation state of the Ti cations in the TiO_2 nanocrystal films before and after annealing in 10^{-8} torr of O_2 at 700 K which, as noted above, was used to clean the surface of the nanocrystals. Consistent with the SEM results (Figure 4.2), photoelectron peaks characteristic of the Si substrate, e.g. Si(2p), could not be detected, demonstrating that the nanoparticle films completely covered the substrate. In addition to peaks for titanium and oxygen, a F(1s) peak was observed for the fresh samples. The fluorine is a byproduct of the synthesis procedure which used TiF_4 as a reactant. The fluorine appears to be limited to the surface, however, and was removed by the oxygen annealing treatment (see Figure 4.3). The surface of the nanocrystals was also determined to be nearly carbon-free after the oxygen anneal via the lack of a C(1s) photoelectron peak (see Figure 4.4).

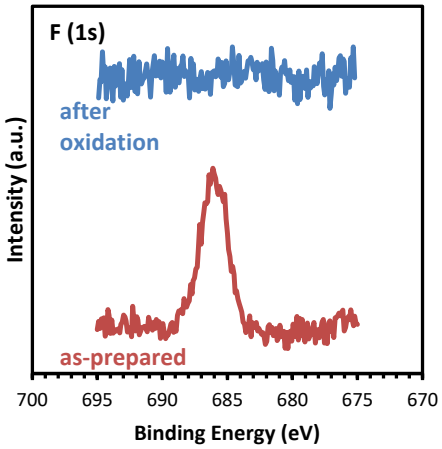

Figure 4.3 F(1s) XPS spectrum of as-prepared 18 nm A-TiO2 thin film sample and following oxidation treatment.

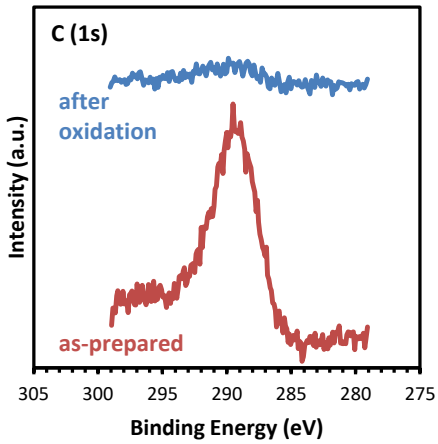

Figure 4.4 C(1s) XPS spectrum of as-prepared 18 nm A-TiO2 thin film sample and following oxidation treatment.

A typical Ti(2p) spectrum for an oxygen-annealed film is shown in Figure 4.5. This spectrum exhibits the expected 2p doublet, with the $2p_{3/2}$ peak at 459.3 eV and the $2p_{1/2}$ peak at 465.1 eV. These peak positions are consistent with those reported in the

literature for Ti^{4+} [29, 31, 111]. The symmetric shape of the peaks and the lack of shoulders on the low- and high-energy sides of the peaks indicate that the Ti cations are predominantly in the 4+ oxidation state. Furthermore, the spectrum did not change significantly over the course of reactivity experiments, nor across different samples, indicating the chemical state of the titanium cations in the catalyst remained consistent throughout the reactivity studies.

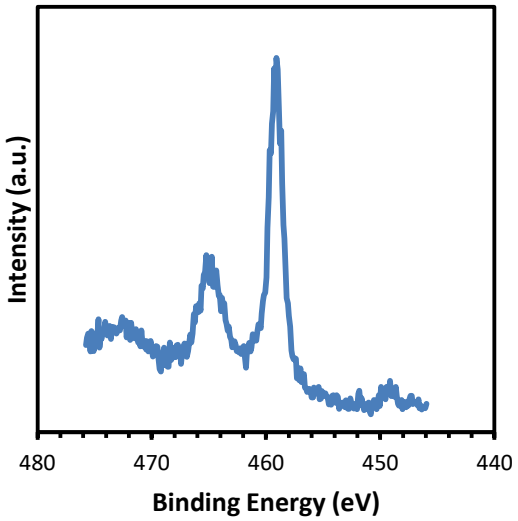

Figure 4.5 Ti(2p) XPS spectrum of an 18 nm A-TiO2 thin film obtained after annealing the sample in oxygen.

4.3.2 Thermal Reactions

The initial TPD reactivity studies focused on the thermally-induced reaction of methanol on the various TiO_2 thin film samples. Experiments were carried out as a function of the particle size and methanol exposure. TPD data obtained from the 10 nm

TiO_2 sample dosed with 2.5 L (1 L = 10^{-6} torr·s) of methanol at 160 K are displayed in Figure 4.6a. Data obtained from the 18 and 25 nm crystallite films were qualitatively similar. As shown in this figure, the primary desorbing species was methanol which produced a broad feature between 200 and 400 K with a tail extending to higher temperatures. A smaller methanol peak, centered at 650 K, was also observed. For this sample, the 2.5 L methanol dose was sufficient to saturate the low-temperature methanol peak. For higher exposures, an additional sharp methanol peak grew in at 195 K which we attribute to desorption of methanol multilayers. The only reaction products detected were small amounts of water, dimethyl ether (CH_3OCH_3), and methane (CH_4) which were produced at 320, 630 and 650 K, respectively. It is possible that a small amount of formaldehyde (CH_2O) was also produced at low temperatures, but it was hard to distinguish this product from methanol due to the overlap in their mass spectrometer cracking patterns and the large size of the methanol signal. The relative product yields for the 10 and 25 nm crystallite films dosed with 2.5 L of methanol are listed in Table 4.1.

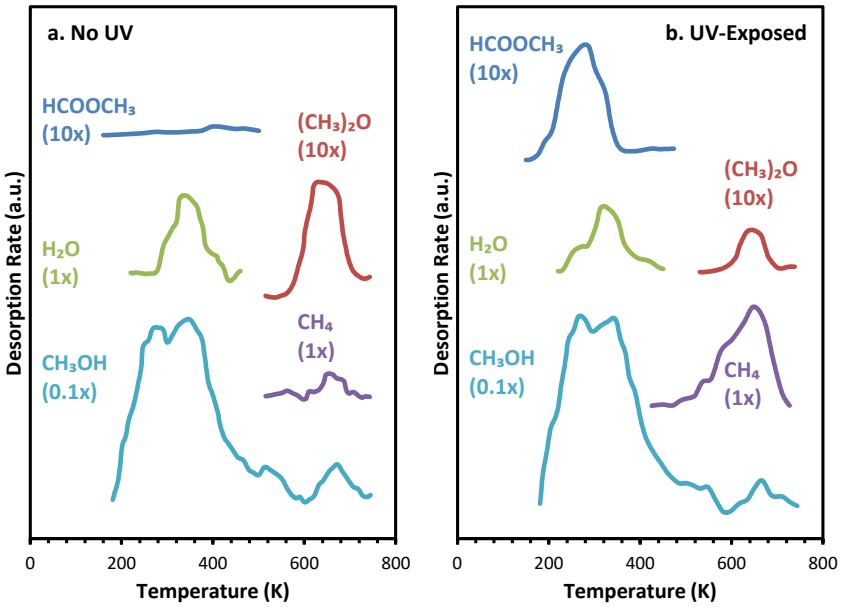

Figure 4.6 TPD results obtained from a 10 nm A-TiO2 nanocrystal film dosed with 2.5 L of methanol at 160 K. The data in panel (a) was obtained immediately following dosing, while that in (b) was obtained after a 3 h UV exposure.

Table 4.1 Product yields for 2.5 L methanol dose.

Nanocrystal Size	CH_3OCH_3	CH_3OH	H_2O	CH_4
10 nm	0.002	1	0.011	0.003
25 nm	0.002	1	0.032	0.008

It is useful to compare these TPD results with those that have been reported previously for the reaction of methanol on A-TiO_2. Herman et al. [27] have reported methanol TPD data obtained from an A-TiO_2(101) single crystal surface. They also observed that for saturation coverage, methanol desorbed between 200 and 400 K. Based in part on XPS data this peak was assigned to molecular methanol adsorbed on the

exposed fivefold coordinate Ti cations on the (101) surface as shown in Figure 4.7. They found that the surface was not very reactive with nearly all of the methanol desorbing intact, although a small methanol peak, corresponding to < 1% of the total adsorbed methanol, was observed at 610 K which was attributed to recombinative desorption of methoxide adsorbed on step edges. These results are similar to those obtained here for the TiO_2 nanocrystals which predominantly expose (101) surfaces.

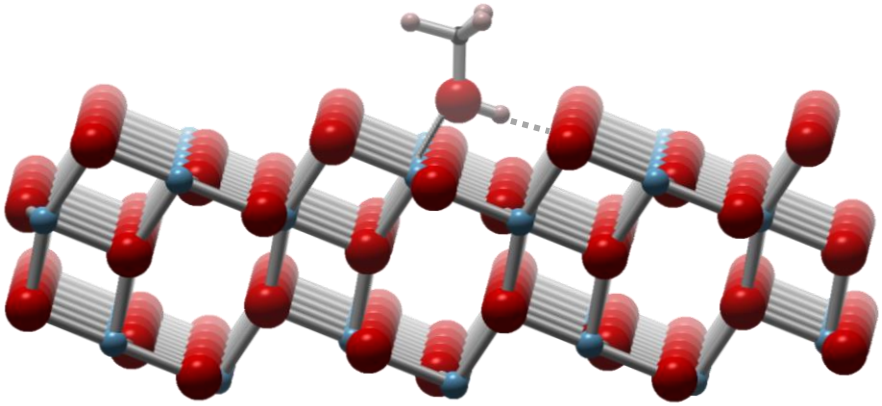

Figure 4.7 Schematic of molecular methanol adsorbed on a fivefold coordinate Ti cation on the A-TiO2(101) surface.

One difference between the Herman et al. [27] study and the results obtained here is that small amounts of the reaction products, H_2O, CH_3OCH_3, and CH_4, were produced on the nanocrystals. A TPD study of the reaction of methanol on a commercial polycrystalline anatase powder by Lusvardi et al. [14] provides some clues as to the origin of these reaction products. In that study roughly 20 % of the adsorbed methanol

was found to react to produce CH_4, CH_3OCH_3, and CH_2O between 600 and 700 K. Based on comparisons to studies of the reaction of methanol on R-TiO_2 single crystals and powders [6, 8, 14, 27, 35, 36, 43] they assigned these products to reaction of methoxide adsorbed on fourfold coordinate Ti cations. Moreover, in the case of CH3OCH3 it was argued that coupling occurs between two methoxide species adsorbed on a single fourfold coordinate Ti cation site [6, 14, 28, 112]. Thus, it is likely that the reaction products obtained on the nanocrystalline films result from reaction of methoxide adsorbed on similar, more highly undercoordinated cation sites. The fact that the fraction of the adsorbed methanol that reacts to produce CH_3OCH_3 and CH_4 on the nanocrystals (<1 %) is significantly less than that observed for polycrystalline powders implies that the active sites for these reactions are not present on the (101) surfaces that are predominantly exposed on the nanocrystals. This scenario is also consistent with the Herman et al. [27] results which show that the TiO_2(101) surface is not active for the reaction of methanol to produce these products. Thus, for the TiO_2 nanocrystals we conclude that highly undercoordinated Ti cations present on the (001) capping surfaces provide sites for dissociative adsorption of methanol to produce methoxide which reacts to form CH_3OCH_3 and CH_4 near 640 K. Such sites could also be located at the edges of the nanocrystals but the concentration of sites at these locations would not likely be high enough to account for all of the CH_3OCH_3 produced. Furthermore, if the sites that are active for CH_3OCH_3 production were predominantly located on the edges, one would expect the yields of these products relative to the amount of methanol that desorbs at low

temperature (coming primarily from the (101) surfaces) to increase with decreasing crystallite size, but no such correlation was observed.

While particle size effects were not observed for the thermally-induced reaction of methanol on the TiO_2 nanocrystals, the amount of reaction products, especially CH_3OCH_3, were found to increase as the methanol dosage was increased beyond that required to saturate the molecularly adsorbed methanol on the fivefold coordinate Ti cation sites on the (101) surfaces (~ 2.5 L). This is illustrated in Figure 4.8 which shows a plot of the amount of CH_3OCH_3 produced at 610 K as a function of the methanol dosage for the 10 and 25 nm TiO_2 nanocrystals. Note that since this is a bimolecular coupling reaction, a non-linear yield trend is not unexpected. This result suggests that the sticking coefficient for methanol on the sites that are active for the production of CH_3OCH_3 is much less than that for molecular adsorption onto the fivefold coordinate Ti cation sites the (101) surfaces. This is the expected result if one assumes that methanol adsorbs dissociatively on the undercoordinated sites to produce methoxide which would be an activated process.

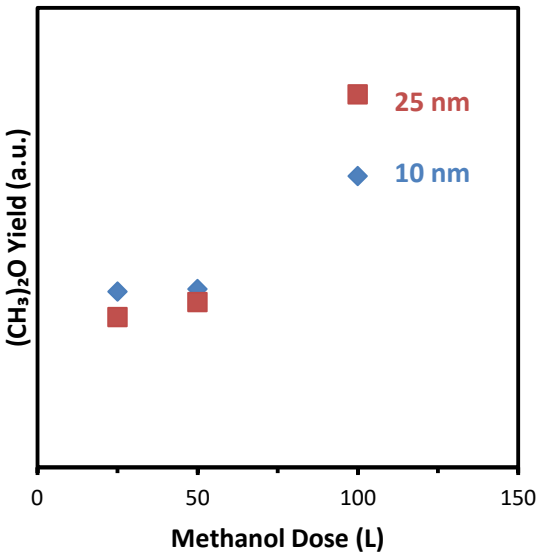

Figure 4.8 Dimethyl ether yield during methanol TPD on 10 nm and 25 nm TiO2 nanocrystals as a function of methanol coverage.

4.3.3 Photochemical Reactions

The photocatalytic reaction of methanol adsorbed on the anatase nanocrystal films was also studied using TPD. For these experiments the samples were initially dosed with methanol at 160 K, then exposed to UV light, followed by TPD. Figure 4.6b displays composite TPD data obtained from a 10 nm TiO_2 nanocrystal film dosed with 2.5 L of methanol and then illuminated with UV light for 3 h. Comparison with the thermal reactivity data in Figure 4.6a shows that the UV exposure caused several changes in the TPD curves with the most significant being the production of the photochemical product, $HCOOCH_3$, which appears in a peak near 260 K. This result is consistent with what has been reported in the literature for both A-TiO_2(101) [76] and R-TiO_2(110) [72, 75, 78] surfaces. Other significant differences include changes in the relative amounts of H_2O at

320 K, and CH_3OCH_3 and CH_4 near 640 K. Similar results were obtained from the films with larger TiO_2 nanocrystals.

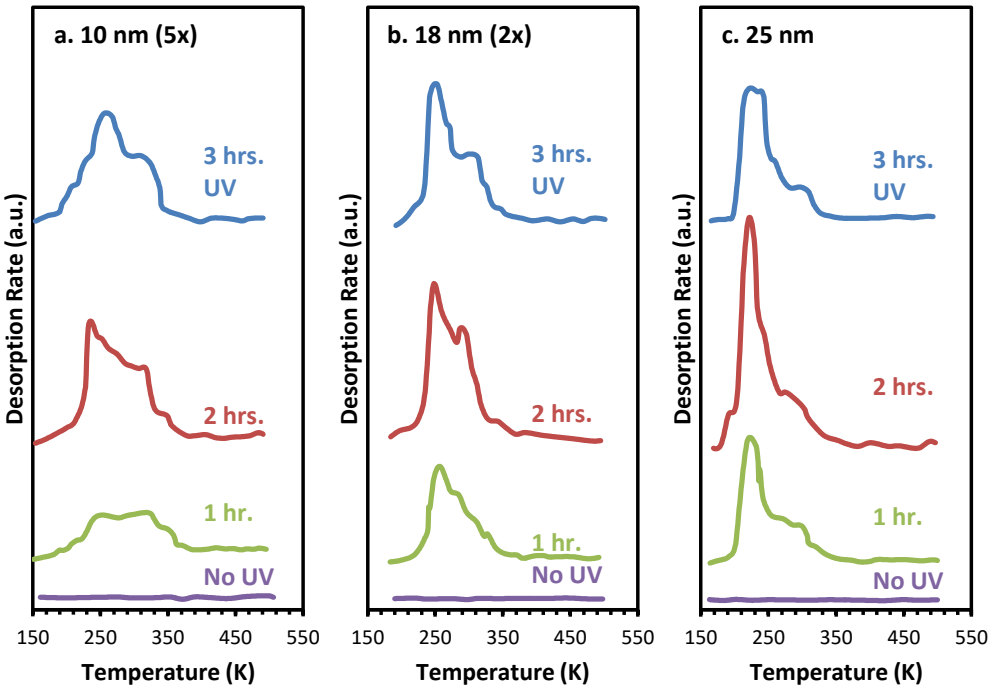

Figure 4.9 Methyl formate desorption obtained from UV-illuminated, methanol-dosed samples as a function of UV exposure time and nanocrystal size: (a) 10 nm crystallites, (b) 18 nm crystallites, and (c) 25 nm crystallites. Desorption rate has been scaled to account

Figure 4.9 shows the evolution of the $HCOOCH_3$ peak with increasing UV exposure for the 10, 18, and 25 nm TiO_2 films dosed with 5 L of methanol. These data along with analogous data for 2.5 L and 10 L methanol doses are quantified in Figure 4.10, which displays plots of the amount of $HCOOCH_3$ produced during TPD as a function of the TiO_2 nanocrystal size and the methanol and UV exposures. Note that in order to account for differences in the surface area of the thin film samples, the data in

these plots have been normalized to the amount of molecular methanol desorbed for saturation (monolayer) methanol coverage. Several trends are apparent in these data. First, the $HCOOCH_3$ production increases with increasing UV exposure up to 2 h, further confirming the photochemical nature of this product. For the 10 nm nanocrystal sample the amount of $HCOOCH_3$ became saturated for a 2 h UV exposure and remained constant when the UV exposure was increased to 3 h. For the 18 and 25 nm nanocrystal samples, however, increasing the UV exposure to 3 h resulted in a decrease in the $HCOOCH_3$ peak area. This trend was reproducible and observed for all three methanol doses. Second, the data in Figure 4.9 also show that the $HCOOCH_3$ desorption feature is composed of two overlapping peaks: a narrow peak centered at 230 K that increases in intensity with increasing methanol dose and a smaller, somewhat broader peak that appears as a shoulder at ~300 K. Third, the amount of $HCOOCH_3$ produced at a constant UV exposure does not saturate and continues to increase for methanol doses that produce multilayer coverages (i.e. 5 and 10 L). Fourth, when accounting for differences in surface area, the activity for the production of $HCOOCH_3$ increases with increasing TiO_2 nanocrystal size. The possible origins of these features and trends in the data will be discussed below.

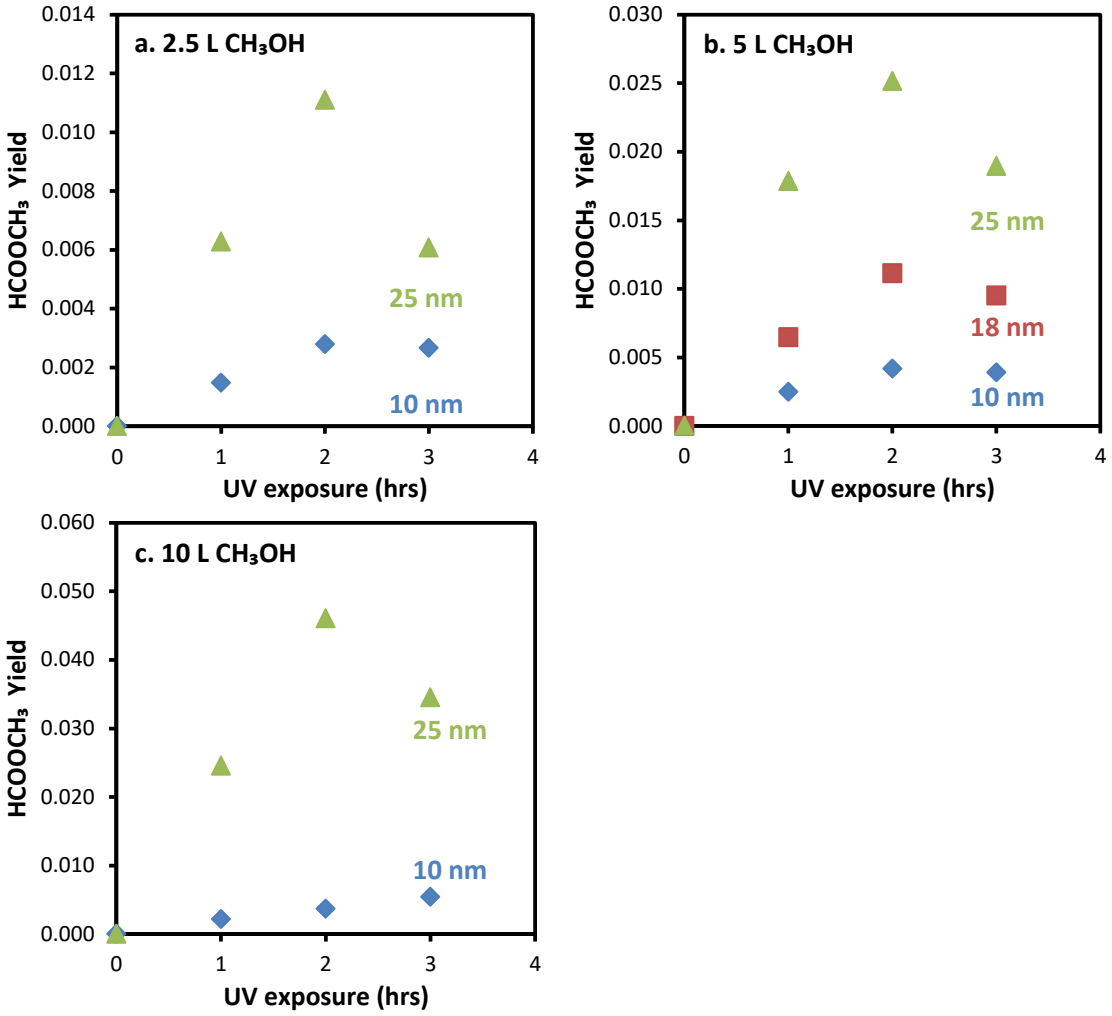

Figure 4.10 Methyl formate yield as a function of UV exposure time and nanocrystal size for (a) 2.5 L, (b) 5 L, and (c) 10 L methanol doses. The yields were normalized to account for differences in surface area.

The amount of CH_4 and CH_3OCH_3, produced during TPD as a function of the A-TiO_2 nanocrystal size and the methanol and UV exposures are plotted in Figure 4.11 and Figure 4.12, respectively. While some CH_4 was produced at 650 K for non-UV exposed samples, the amount of CH_4 produced at this temperature increased significantly upon UV irradiation, demonstrating that its precursor can also be produced via a

photochemical pathway. This is most apparent for the 25 nm TiO_2 nanocrystals where CH_4 is the dominant TPD product following UV exposure. The opposite trend is observed for CH_3OCH_3 (see Figure 4.12) that is produced at 630 K where the amount rapidly decreases with increasing UV exposure. This could be due either to photodecomposition of the methoxide that couples to produce CH_3OCH_3, or their involvement in the photochemical pathway that produces $HCOOCH_3$ at lower temperatures. Also note that the falloff in the amount CH_3OCH_3 produced with increasing UV exposure occurs more rapidly for the larger crystallites. This provides additional evidence that the photocatalytic activity increases with increasing TiO_2 particle size.

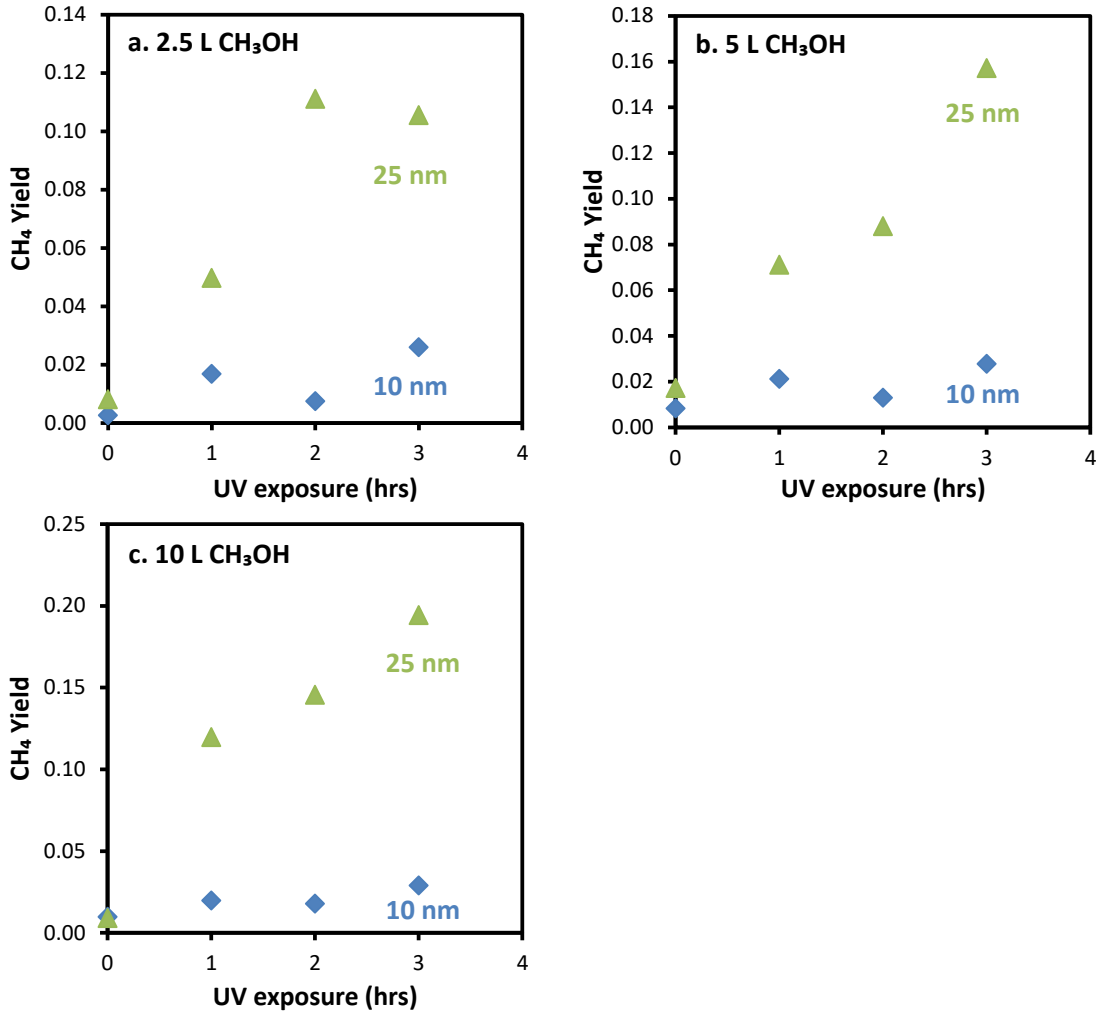

Figure 4.11 Methane yield as a function of UV exposure time and nanocrystal size for (a) 2.5 L, (b) 5 L, and (c) 10 L methanol doses. The yields were normalized to account for differences in surface area.

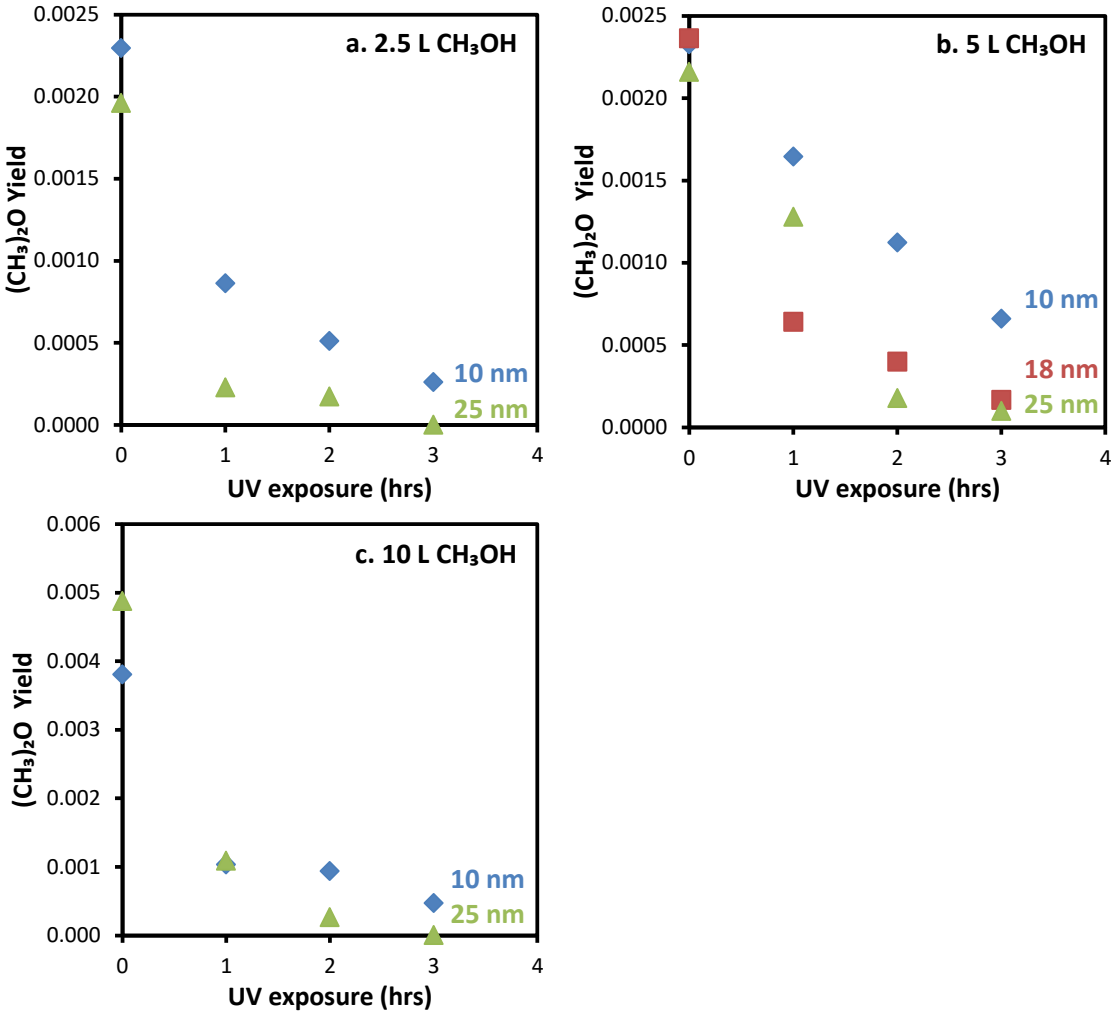

Figure 4.12 Dimethyl ether yield as a function of UV exposure time and nanocrystal size for (a) 2.5 L, (b) 5 L, and (c) 10 L methanol doses. The yields were normalized to account for differences in surface area.

In order to study the photochemical reactions of the methoxide which reacts at 630 K to produce CH_3OCH_3, the following experiment was performed. A 25 nm TiO_2 sample was exposed to 5 L of methanol at 160 K. The sample was heated to 400 K, and then rapidly cooled back down to 160 K. This was followed by a 2 h UV exposure and then TPD. The intermediate heating step to 400 K was done in order to remove

molecularly adsorbed methanol from both the exposed (101) and (001) surfaces. The TPD results obtained in this experiment, a subset of which are displayed in Figure 4.13, were quite interesting. Of particular note is the fact that the CH_3OCH_3 peak at 630 K was only slightly changed from that obtained in a regular TPD run without prior UV illumination (see Figure 4.6a), and that no $HCOOCH_3$ was produced at 260 K. This latter observation is consistent with the mechanism for the photocatalytic production of $HCOOCH_3$ on A-TiO_2(101) whose initial step is thought to be the photo-dissociation of methanol to produce methoxide on the fivefold coordinate Ti cations on this surface [72, 75, 76]. The results obtained here show that such methoxide cannot be produced thermally, at least on this surface. These results also provide further support for the conclusion that the methoxide that is responsible for the CH_3OCH_3 at 630 K are not located on sites on the (101) surfaces, but are on the (001) surfaces.

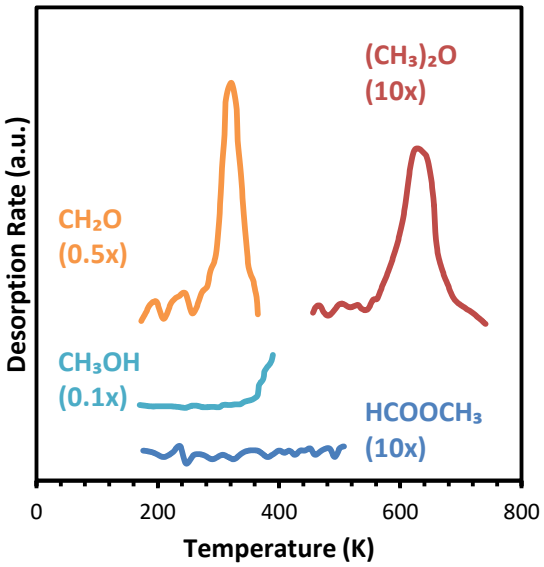

Figure 4.13 Methyl formate, dimethyl ether, methanol, and formaldehyde desorption curves obtained from a 25 nm A-TiO2 sample dosed with 5 L of CH3OH at 160 K. After dosing the sample was briefly heated to 400 K to remove molecularly-adsorbed methanol and allowed to cool back to 160 K. The surface was then exposed to UV illumination for 2 h before the TPD data was collected.

For constant methanol exposure, the relative amounts of CH_3OCH_3 produced at 630 K during TPD for a 25 nm sample not exposed to UV light, exposed to UV light (2 h) after an intermediate heating step, and exposed to UV light (2 h) without an intermediate heating step was 1.0 : 0.7 : 0.1. This result demonstrates that the methoxide that reacts to make the CH_3OCH_3 product are much less prone to photo-decomposition or reaction when the sample is not covered with molecularly adsorbed methanol. As shown in Figure 4.13, a small amount of CH_2O was produced at 320 K in the experiment with the intermediate heating step and must be a product of the photoreaction of the adsorbed methoxide.

4.4 Discussion

The results obtained in this study provide insight into the relationships between surface structure, nanocrystal size, and activity for both thermal- and photo-induced reactions of methanol on A-TiO_2. As described above, the data for thermally-induced reactions are consistent with what has been reported previously for the reaction of methanol on single crystal A-TiO_2(101) [27]. This surface is not very reactive toward methanol which adsorbs only molecularly on the exposed fivefold coordinate Ti cations (see Figure 4.7). During TPD this molecularly-adsorbed methanol desorbs intact between 200 and 400 K. This feature dominated the methanol TPD data obtained from the well-defined A-TiO_2 nanocrystal films used in the present study which preferentially expose the (101) surface. Thus, TPD results obtained from the macroscopic single crystal oxide surface can be directly mapped onto the corresponding surface in the nanocrystalline material.

While as expected, the reaction of methanol with the nanocrystals was dominated by the preferentially-exposed (101) surfaces, an additional pathway, bimolecular coupling of methoxide to produce CH_3OCH_3, was observed near 630 K. As discussed above, this latter pathway appears to take place on the minority (001) surfaces. The methoxide that is involved in this reaction is produced by dissociative adsorption of methanol at low temperatures. Thus, the (101) and (001) surfaces contain different types of Ti cation sites that have dissimilar reactivities toward methanol. Comparison to previous studies of the reaction of oxygenates on R-TiO_2 single crystal surfaces provides useful insight into the identity of the sites on the exposed (001) surfaces of the anatase

nanocrystals [6, 29]. In particular, these studies show that bimolecular coupling of adsorbed oxygenates, e.g. methoxide → (CH_3OCH_3 and acetate → acetone, occurs on fourfold coordinate Ti cations. Cations with a pair of coordination vacancies are thought to be required to facilitate both reactants (e.g. two methoxide species) being bonded to a common site. This leads to the conclusion that such sites must be present on the (001) surface of the nanocrystals. While this would not be the case for an ideal A-TiO_2(001) surface, this surface is not stable and undergoes a two-domain, (1 x 4) reconstruction [8, 30, 32, 33]. A variety of structural models that incorporate microfacets or added or missing rows have been proposed for this reconstruction [30-34], most of which contain at least some fourfold coordinate Ti cations on the surface. Such models would be consistent with the present study where the dimerization of the adsorbed methoxide occurs on fourfold coordinate Ti cations that are located on the exposed (001) surfaces. We note, however, that Tanner et al. [31] have performed formic and acetic acid TPD studies on the (1 x 4) A-TiO_2(001) surface and did not observe the bimolecular ketonization pathway which is known to occur on fourfold coordinate Ti cation sites [29]. Based in part on this result and AFM and STM studies they argued in favor of the so called add-molecule reconstruction proposed by Lazzeri and Selloni [34] that contains an added row of TiO_3 situated above a row of oxygen vacancies. While this reconstruction contains fourfold coordinate Ti cations, one of the missing ligands is located below the cation making it inaccessible to adsorbates. This adds some uncertainty to our assignment of the active sties for the coupling of methoxide to CH_3OCH_3 to fourfold coordinate Ti cations located on the exposed (001) surfaces on the nanocrystals. It is possible that due

to the differences in length scales a different reconstruction may occur on the nanocrystals. Note that the unit cell of the proposed added row (1 x 4) reconstruction of A-TiO_2(001) is ~1.5 nm in width in the [010] direction, which is similar to the width of the capping (001) surfaces in the A-TiO_2 nanocrystals used in this study which ranged from approximately 3 to 6 nm. Alternatively, the production of CH_3OCH_3 may occur at highly undercoordinated Ti cations located at defect sites or on the crystal edges.

The photochemistry experiments yielded additional insight into the site requirements and reaction pathways for the photo-induced reaction of methoxide on A-TiO_2. Consistent with previous studies of the photo-oxidation of methanol on A-TiO_2(101) [76] and R-TiO_2(110) [72, 75, 78] methyl formate was produced following exposure of the methanol-dosed A-TiO_2 nanocrystal thin films to UV radiation. The photochemical nature of this reaction is demonstrated by the increasing yield of $HCOOCH_3$ with increasing UV exposure (see Figure 4.9 and Figure 4.10). The generally accepted mechanism for this reaction is as follows [76]:

$$\mathrm{CH_3OH_{(Ti)}} \xrightarrow{h\nu} \mathrm{CH_3O_{(Ti)}} + \mathrm{H_{(O)}} \qquad \textbf{4.1}$$

$$\mathrm{CH_3O_{(Ti)}} \xrightarrow{h\nu} \mathrm{CH_2O_{(Ti)}} + \mathrm{H_{(O)}} \qquad \textbf{4.2}$$

$$\mathrm{CH_2O_{(Ti)}} + \mathrm{CH_3O_{(Ti)}} \xrightarrow{h\nu} \mathrm{HCOOCH_{3(Ti)}} + \mathrm{H_{(O)}} \qquad \textbf{4.3}$$

where (Ti) and (O) indicate the bonding sites which on A-TiO_2(101) are the fivefold coordinate Ti cations and bridging oxygens. Phillips et al. report that for R-TiO_2 the photo-dissociation of surface methoxide to produce formaldehyde (reaction 4.2) is a direct hole-mediated reaction and is the rate limiting step for this process [78]. Indirect pathways involving photochemically produced hydroxyl radicals can also occur, especially in aqueous environments [113, 114], but are not likely to play an important role for the UHV conditions used in the present study [68].

While this mechanism is consistent with reaction on the exposed (101) surfaces of the nanocrystals, the results obtained in the present study exhibit some features that were not observed in a previous study by Xu et al. of the photo-oxidation of methanol on A-TiO_2(101) [76]. In TPD photochemistry experiments in that study similar to those reported here, $HCOOCH_3$ was observed in a single peak centered at 260 K. In contrast, in the present study $HCOOCH_3$ was produced in two peaks centered 230 and 300 K. For a given methanol dose, the area of the latter peak was found to nearly saturate for relatively short UV exposures while the former continued to grow and became increasingly narrow with increasing UV exposure (see Figure 4.9). While it is tempting to assign the low- and high-temperature peaks to reaction on the exposed (101) and (001) surfaces, respectively, the TPD data shown in Figure 4.13 in which the surface was heated to an intermediate temperature to desorb molecular methanol prior to UV exposure argues against this. Note that in this experiment $HCOOCH_3$ was not produced in spite of the fact that methoxide

was still present on the (001) surface and undergoes coupling to produce CH_3OCH_3 at 630 K.

We instead propose the following assignments for these peaks. The 300 K peak is due to desorption of $HCOOCH_3$ on the fivefold Ti cation sites on the (101) surface, and the 230 K peak is due to desorption of $HCOOCH_3$ that has been displaced from the surface into the methanol multilayer. Note that the methanol doses used in this study were sufficient to produce a condensed layer of methanol. The TPD data clearly shows that this occurs for the 5 L and 10 L doses where a large, zero-order methanol peak appears at 195 K. The fact that the area of the 230 K $HCOOCH_3$ peak increases with increasing methanol dose, while the 300 K peak remains largely unchanged for constant UV exposure also supports this assignment. Thus it appears for the conditions used in this study, methanol from the multilayer can displace the photochemical reaction product, $HCOOCH_3$, from the fivefold coordinate Ti cations on the (101) surfaces, thereby allowing for multiple turnovers of the photochemical reaction to occur on these sites.

The data in Figure 4.10 also shows that for the 18 and 25 nm nanocrystals the $HCOOCH_3$ yield as a function of UV exposure goes through a maximum near 2 h and then starts to decrease at longer UV exposure times. We attribute this decrease in yield to photo-decomposition of a portion of the $HCOOCH_3$ product which remains on the surface after it is formed. The products of such a reaction pathway would likely be CO, CO_2, H_2O and methyl groups. Since CO and CO_2 would interact very weakly with the surface, these products would desorb once formed. Unfortunately our experimental set-up was not conducive to monitoring desorption products during UV illumination, so we have

not been able to confirm the production of CO or CO_2. There is ample evidence, however, for methyl group production, since as shown in Figure 4.6b, CH_4 was produced at 650 K for the UV exposed surfaces. The fact that this product results from a photochemical pathway is demonstrated in Figure 4.11 which shows that the CH_4 yield increases with increasing UV exposure. This proposed pathway involving two reactions in series, photochemical oxidation of methanol to $HCOOCH_3$ and photochemical decomposition of the $HCOOCH_3$, is also consistent with the trends in the yields of these products with UV illumination time (Figure 4.10 and Figure 4.11) which show that the CH_4 yield continues to grow even after the $HCOOCH_3$ yield starts to decrease.

The amount of CH_4 produced in the present study is much larger than that which could be attributed to reaction of methoxide only on the minority (001) exposed surfaces on the nanocrystals and therefore must be due to reaction of the (101) surfaces. We note, however, that the CH_4 product was not observed in Xu et al.'s study of methanol photo-oxidation on A-TiO_2(101) [76]. The origin of this discrepancy between the two studies is not clear. It is possible that it reflects a difference between the intrinsic photocatalytic activity of the nanocrystals and the macroscopic A-TiO_2(101) single crystal, or alternatively it may result from the different conditions (e.g. methanol coverage, UV exposures) that were used in the two studies.

The reaction pathway(s) responsible for the decrease in the CH_3OCH_3 yield from the (001) surface with increasing UV exposure (Figure 4.12) cannot be definitively determined from the results obtained in this study, but this methoxide also clearly undergoes photochemical reactions. It is likely that the methoxide on the (001) surface

can also undergo photo-oxidation to produce $HCOOCH_3$. The TPD data with an intermediate flash provide support for this, since CH_2O was detected as a significant product and photo-dissociation of methoxide to produce CH_2O (reaction 4.2) has been shown to be the rate limiting step in the pathway that produces $HCOOCH_3$ [78]. It is somewhat surprising, however, that for the conditions used in this experiment the CH_2O did not undergo further reaction to produce $HCOOCH_3$ (reaction 4.3) indicating that this latter reaction does not occur on the methoxide-covered (001) surface in the absence of molecularly adsorbed methanol (Figure 4.13). This is further supported by the fact that the rate of photoreaction of methoxide on this surface decreased significantly when the molecular methanol was removed. This suggests that reaction 4.3, which involves the photo-coupling of CH_2O with methoxide, actually requires molecular methanol as one of the reactants on the (001) surface.

Finally, while the catalytic activity of the A-TiO_2 nanocrystals exhibited no strong size effects, some subtle differences between the photocatalytic activity of the small and large nanocrystals was observed. This is most apparent in Figure 4.10 and Figure 4.11 which show that the normalized yield of $HCOOCH_3$ and CH_4 was consistently higher on the larger nanocrystals. The origin of this effect is difficult to discern. Since thin films of the nanocrystals were used, it may merely be due differences in the overall morphology of the films which effects how they scatter the light. Alternatively there may be an optimum crystallite size for light adsorption for the UV wavelength used in this study.

4.5 Conclusions

The results obtained in this study demonstrate that thin films of mono-disperse, well-defined, metal oxide nanocrystals are excellent model systems that can help bridge the materials gap between studies of single crystals and high surface area powders, and that studies of such systems can provide new insight into structure-activity relationships for both thermal- and photochemical catalytic reactions.

Two different modes of adsorption of methanol on the truncated, bi-pyramidal A-TiO_2 nanocrystals used in this study were observed. On the predominant A-TiO_2(101) surfaces methanol adsorbed only molecularly on fivefold coordinate surface Ti cations, which is consistent with what has been reported in the literature for single crystal A-TiO_2(101) by Herman et al.[27] In contrast, on the minority A-TiO_2(001) surfaces dissociative adsorption of methanol to produce adsorbed methoxide takes place and more complex chemistry was observed on this surface. Upon heating, methoxide underwent bimolecular coupling to produce CH_3OCH_3 at 630 K. Since the active site for this reaction has previously been shown to be a fourfold coordinate Ti cations which can accommodate both methoxide species, this result indicates that such sites must be present on the minority A-TiO_2(001) surfaces of the nanocrystals. This result is at odds with studies of the reactivity of A-TiO_2(001) single crystal surfaces where similar chemistry has not been observed.[31] This may be due to different reconstructions occurring on the nanocrystal and single crystal A-TiO_2(001) surfaces due to the different length scales. We will investigate this possibility in future studies in which we will employ TiO_2 nanocrystals with a platelet geometry that preferentially exposes the (001) surface.

The A-TiO_2 nanocrystals were found to be active for the photo-catalytic oxidation of methanol to $HCOOCH_3$. On the A-TiO_2(101) surface, this reaction proceeded in a stepwise photocatalytic pathway involving dehydrogenation of methanol to form methoxide and then CH_2O, followed by coupling of these latter two species to form $HCOOCH_3$. For conditions where multilayers of methanol were present on the (101) surface, the adsorbed $HCOOCH_3$ product could be displaced into the multilayer at low temperatures (160 K) allowing for multiple turnovers on each site. Photocatalytic decomposition of the $HCOOCH_3$ product was also observed producing adsorbed methyl groups and presumably CO and CO_2 which desorb at low temperature. The minority exposed A-TiO_2(001) surfaces in the nanocrystals were also found to be active for the photocatalytic oxidation of methanol. In this case, however, methoxide could be produced thermally and the reaction either proceeds only to CH_2O or requires molecular methanol rather than methoxide in the final step which produces methyl formate.

Finally, only subtle size effects were observed for the photo-catalyzed oxidation of methanol on the A-TiO_2 nanocrystals, with the most significant being an increase in the overall activity with increasing particle size. This effect may be due to how the nanocrystal films scatter the light or there being optimal crystallite size for adsorption of the UV wavelength used in this study.

Chapter 5. Shape-Dependence of the Thermal and Photochemical Reactions of Methanol on Nanocrystalline Anatase TiO_2[9]

Summary

This publication was a continuation of the TiO_2 project introduced in Chapter 4. Three sizes of platelet nanocrystals were studied, and the results were compared to the findings from the previous publication. This confirmed the previous active site assignments and allowed for investigation into shape-dependent activity trends. This publication featured a deeper exploration into the underlying photochemical processes and how they are affected by nanocrystal size and shape. Additionally, a link is observed between the activity of the etherification reaction and nanocrystal facet size, and the case is made for a possible facet-size-dependent surface reconstruction.

[9] This chapter was published as **Bennett, D. A.**; Cargnello, M.; Diroll, B. T..; Murray, C. B.; Vohs, J. M., *Surface Science* 654 (2016) 1-7

5.1 Introduction

Surface science studies of well-defined, single-crystal, model catalysts have made many important contributions to our understanding of the reactivity of a range of catalytic materials. Indeed, this approach has been invaluable in elucidating structure-activity relationships, and the identification of specific active sites, reaction pathways, and the structure of adsorbed intermediates [3, 20, 98, 99]. While this approach has been very successful, it still has its limitations since single crystals often do not contain the range of sites that occur in the analogous high surface area catalysts that are used in industrial practice. Recently studies have started to appear in the literature in which an effort has been made to bridge this so called "materials gap" [101-108]. One promising approach to achieving this goal is use thin films of well-defined nanocrystals as model catalysts. This approach has the advantage that the exposed crystal planes are still well-defined which can allow comparisons to be made to the single crystal literature, if available, while at the same time providing for a wider range of sites, such as those at edges and corners, whose concentration can be systematically controlled by varying the crystallite size and shape. Using well-defined nanocrystals may in many cases also allow one to systematically study the reactivity of individual exposed crystal planes for materials for which single crystals are not readily available, which is the case for many metal oxides.

A recent study by the Overbury group at Oak Ridge National Laboratory of the catalytic activity of ceria nanocrystals (octahedra, cubes, and nanowires) provides a good example of this type of study [107]. In this work it was found that ceria nanowires had higher activity than the octahedral nanocrystals for the conversion of acetaldehyde to

both decomposition and coupling products in a flow reactor. Furthermore, the wires and cubes were more selective for C-C bond scission to produce C_1 products, while octahedra were more selective for aldol condensation. This was attributed in part to the cerium cations with lower coordination numbers and a higher defect density on the surface of the nanowires and cubes.

We have also recently used this approach to study structure-activity relationships for both catalytic and photocatalytic reactions on anatase TiO_2 (A-TiO_2) using methanol as a prototypical oxygenate reactant [115]. This study made use of size-selected, A-TiO_2 nanocrystals with a truncated bipyramidal shape that were cast into thin films on oxidized silicon wafers. As shown in Figure 1, these A-TiO_2 crystals expose the {101} family of crystal planes on the sides of the pyramids and are capped by {001} planes. Temperature-programmed desorption (TPD) studies of the thermal and photo-oxidation of methanol were used to probe how the crystallite size affected reactivity. As will be discussed in more detail below, we observed that in the absence of UV illumination the nanocrystals were active for the coupling of adsorbed methoxide groups to produce dimethyl ether which occurred primarily on undercoordinated Ti cation sites located on the {001} planes. UV illumination caused methyl formate to also be produced which appeared to occur on sites located on the {101} planes. The relative yield of this photochemical product was also found to be dependent on the crystallite size.

In the work reported here we have extended our previous study to include the reactions and photoreactions of methanol over TiO_2 nanocrystals that have the platelet geometry shown in Figure 5.1. Note that this shape is just a more truncated version of the

bipyramids that were used is our previous study, but due to the different aspect ratio the area of the {001} planes relative to the {101} planes is much higher in the platelets compared to the bipyramids.

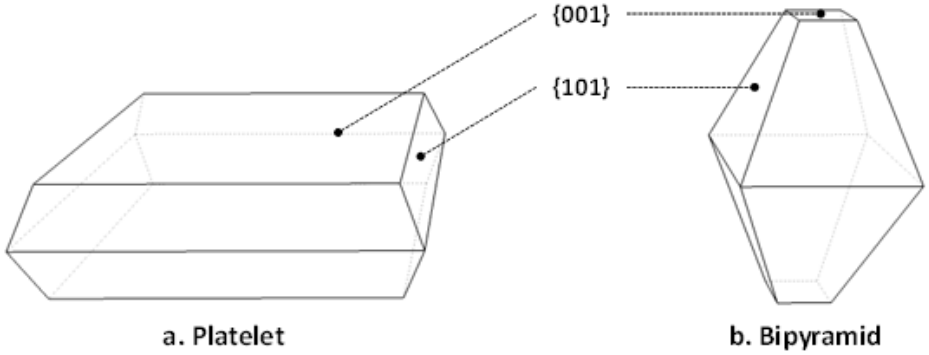

Figure 5.1 Schematic showing the shape and exposed crystal planes of the (a) platelet and (b) bipyramidal anatase nanocrystals. Both forms present exclusively {101} and {001} surfaces, but the {001} surfaces account for a larger fraction of the platelet nanocrystals.

5.2 Materials and Methods

A detailed description of the synthesis of the TiO_2 nanocrystals can be found in Gordon et al [87]. Briefly, a stock solution of TiF_4 and $TiCl_4$ was added to a cosurfactant (either oleylamine or 1-octadecanol) and heated to 563 K. After seed crystal formation, additional stock solution was delivered via syringe pump. Nanocrystal size was controlled by varying the amount of added stock solution. The nanocrystal shape was determined by the relative surface energies of the {101} and {001} facets. The {001} surface is stabilized in the presence of HF generated during hydrolysis of the TiF_4 precursor. Thus oleylamine, which moderates the amount of HF, favors the growth of the

{101} surfaces and leads to a bipyramidal shape, while 1-octadecanol promotes a higher fraction of exposed {001} surfaces, leading to a flatter, platelet shape (see Figure 1). In the current study three different sizes of platelet nanocrystals were used which had lateral dimensions of 14 nm, 18 nm, and 22 nm as determined by electron microscopy. (These values have an accuracy of ± 3 nm). We also compare to data obtained previously for bipyramidal nanocrystals which had long axes of 10 nm, 18 nm, and 25 nm [115]. To allow the use of traditional surface science analytical techniques, the nanocrystals were suspended in hexane and then spin-cast onto oxidized, single crystal Si substrates to produce thin films.

Transmission electron microscopy (TEM) was used to characterize the as-synthesized nanocrystals. For these experiments the nanocrystals were dispersed onto a 300 mesh C-coated Cu TEM grid and images were collected using a JEOL JEM1400 TEM operating at 120 kV. The thin film samples were also characterized by scanning electron microscopy (SEM) using a JEOL 7500F HRSEM. For these experiments the samples were not coated but a conducting tape was applied near the edge of the substrate to reduce sample charging. Imagines were collected in secondary electron imaging mode with a 5 kV beam.

Reactivity experiments were conducted in an ultra-high vacuum (UHV) chamber with a base pressure of 2×10^{-10} Torr. The chamber was equipped with a quadrupole mass spectrometer (Stanford Research Systems) which was used for temperature programmed desorption (TPD) experiments, and a dual-anode X-ray source (VG Microtech) and a hemispherical electron energy analyzer (Leybold-Heraeus) which were

used for x-ray photoelectron spectroscopy (XPS). The thin film samples were cut into pieces approximately 8 mm x 6 mm and mounted in Ta foil holders which were spot welded to an electrical feedthrough on the UHV chamber. Each sample was heated resistively by passing electrical current through the Ta foil and cooled by conduction from a liquid nitrogen reservoir in contact with the electrical feedthrough. The sample temperature was monitored by a type-K thermocouple which was fixed to the back of the Si substrate using ceramic adhesive (Aremco).

HPLC-grade methanol (Fisher Scientific) was used as the reactant and was subjected to multiple freeze-pump-thaw cycles before use. The methanol was stored in a glass vial and was admitted to the chamber through a variable leak valve (Varian) and directed onto the sample by a dosing needle positioned near the surface of the sample. The sample was held at 160 K during methanol dosing. The sample temperature was ramped upwards at 3 K s^{-1} during TPD experiments. Oxygen (Matheson, 99.997%) was used for sample cleaning and was admitted to the chamber in the same fashion as the methanol.

To study photochemical reactions the samples were illuminated with monochromatic UV light (365 nm) from a UV LED source (Prizmatix). This light was admitted into the chamber via a fiber optic cable and the sample was positioned in front of the end of this cable during UV illumination. The photon flux at the surface of the sample was 10^{15} cm^{-2} s^{-1} as determined by a photodiode detector (Thorlabs). The samples were held at 160 K during illumination to prevent desorption of surface species.

In order to allow quantitative comparison of the product yields from different thin film samples, desorption peak areas were scaled to account for mass spectrometer sensitivity factors and for exposed surface area. The latter was estimated using methanol TPD data as a function of methanol coverage to determine the point at which condensed methanol multilayers first form. The following masses were monitored during TPD experiments: 16 (CH_4), 18 (H_2O), 30 (CH_2O), 31 (CH_3OH), 45 (CH_3OCH_3), and 60 ($HCOOCH_3$).

5.3 Results

5.3.1 Catalyst Characterization

TEM micrographs of one size of each of the platelet and bipyramidal A-TiO_2 nanocrystals are displayed in Figure 5.2a and Figure 5.2b, respectively. In these images the bipyramidal crystallites are laying on one of the {101} planes while the platelets are situated with the {001} surfaces parallel to the image plane. SEM images of spin-cast films of each crystallite morphology are displayed in Figure 5.2c and Figure 5.2d. These images were obtained after the samples were annealed in UHV at 800 K. The crystallites in the films have a random orientation and the image of the platelet film (Figure 5.2d) shows that the crystallites in this particular sample have a thickness of ~ 4 nm. These images also show that in both instances the nanocrystals completely cover the substrate to a depth of at least several particles and that heating to 800 K does not result in any appreciable sintering of the particles.

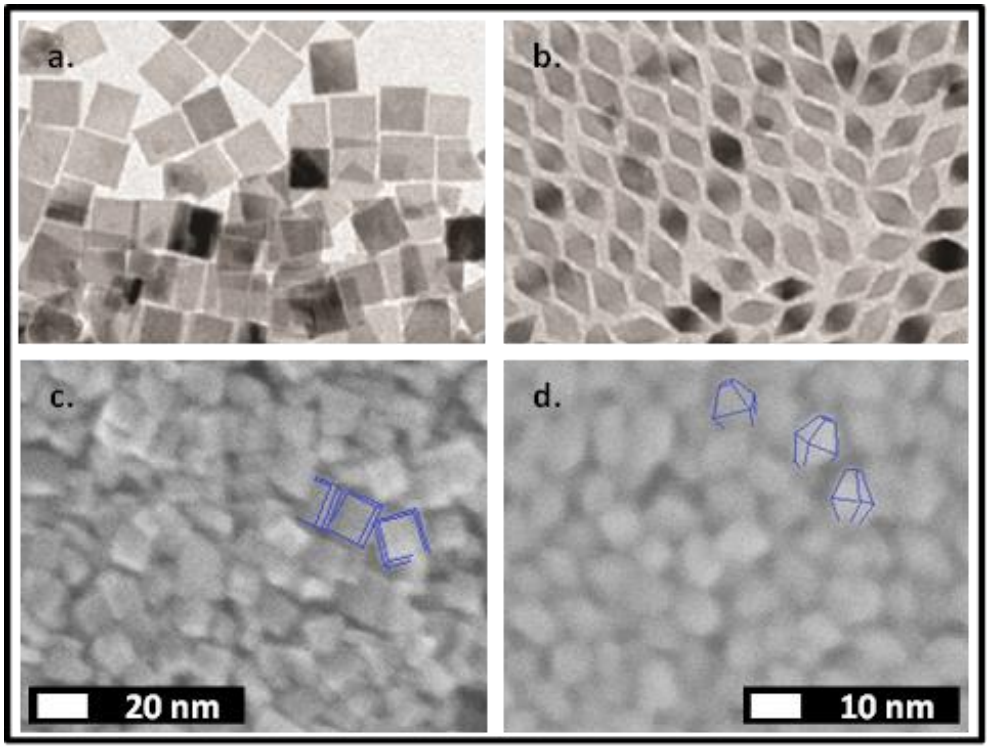

Figure 5.2 TEM micrographs of the as-synthesized (a) platelet and (b) bipyramidal anatase nanocrystals, and SEM micrographs of the (c) platelet and (d) bipyramidal nanocrystal thin films dispersed onto oxidized silicon substrates which were used in reactivity studies.

XPS analysis of freshly-prepared bipyramidal and platelet thin film samples showed that the surfaces of the nanocrystals were covered with both fluorine and carbon. The fluorine results from the use of TiF_4 as one of the precursors during synthesis. Chlorine was not detected via XPS. It was found, however, that both of the F and C impurities could be removed by annealing in 10^{-8} Torr of oxygen at 750 K. Ti(2p) XP spectra obtained after this treatment were indicative of Ti^{4+}. Representative XP spectra are provided in Figure 5.3.

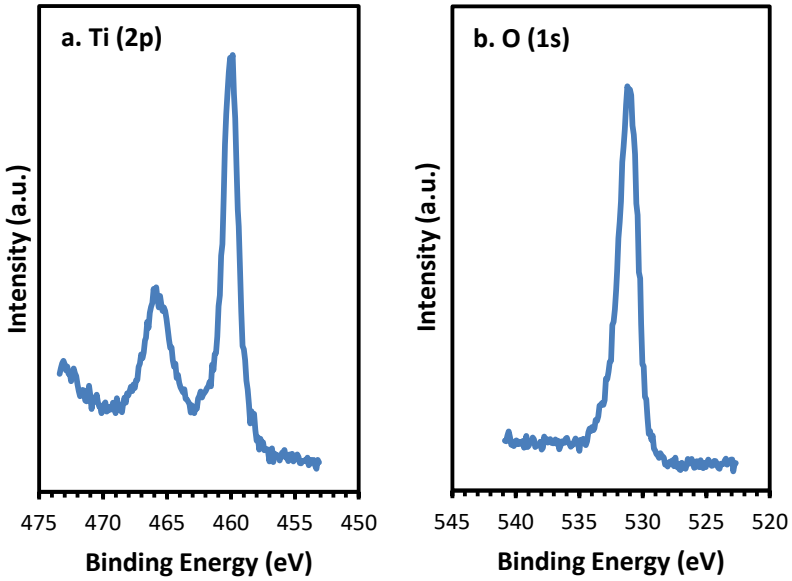

Figure 5.3 Ti (2p) (a) and O (1s) (b) XP spectra of a 14 nm platelet thin film sample.

5.3.2 Thermal Reactions

Representative TPD results for the platelet nanocrystals are given in Figure 5.4a. This dataset was obtained from a thin film of the 14 nm nanocrystals dosed with 2.5 L (1 Langmuir = 10^{-6} Torr·s) of methanol (CH_3OH), an exposure that was found to be sufficient to saturate the surface with methanol. The TPD data show that the majority of the methanol desorbs intact in a broad two-peak structure between 180 and 450 K. Two smaller methanol peaks are also present at 500 K and 620 K. The only reaction products detected were H_2O which desorbed at 320 K, and formaldehyde (CH_2O), methane (CH_4) and dimethyl ether (CH_3OCH_3) which were all produced near 640 K. The H_2O is likely a byproduct of deprotonation of a fraction of the adsorbed methanol to produce adsorbed

methoxide groups and surface hydroxyl groups which incorporate a surface lattice oxygen. There are two competing reaction pathways for these hydroxyl groups: (1) recombination with methoxide to produce methanol or (2) reaction to produce H_2O, both of which occur at 320 K [29, 43]. The methoxide groups that don't recombine to produce methanol remain on the surface and give rise to the higher-temperature products in the TPD.

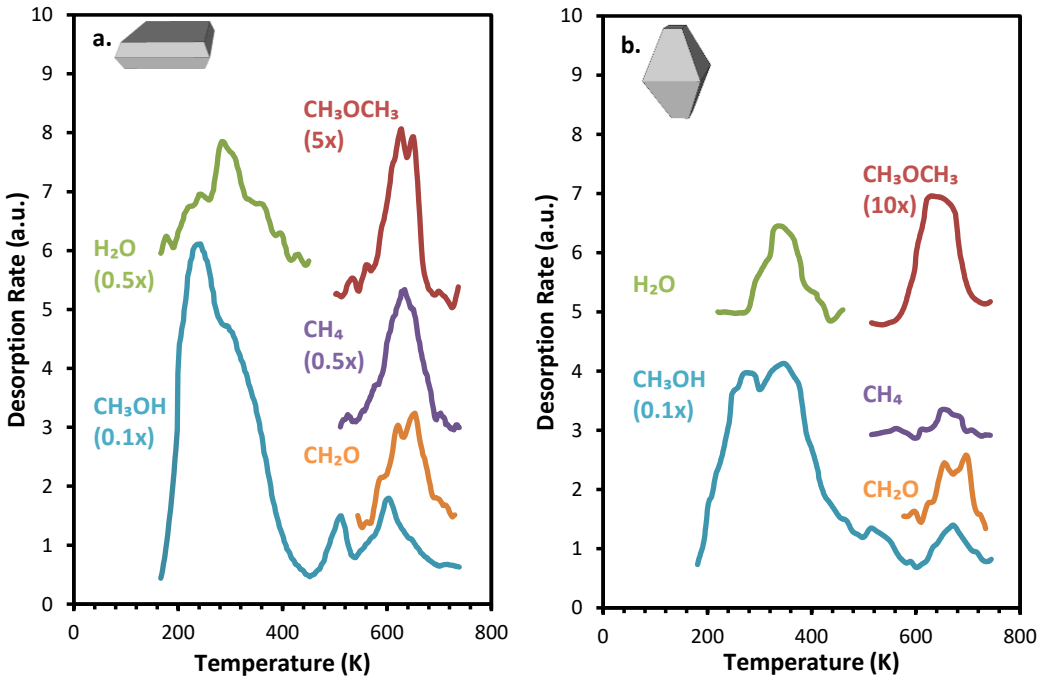

Figure 5.4 TPD results obtained from (a) 14 nm platelet and (b) 10 nm bipyramidal nanocrystal thin films dosed with 2.5 L of methanol at 160 K. Desorption intensities have been scaled to account for mass spectrometer sensitivity and difference in surface area.

The methanol and CH_2O products near 640 K can be attributed to a C-H bond scission in an adsorbed methoxide to produce formaldehyde with the resulting H reacting

with another methoxide to produce methanol [35]. In addition to this disproportionation reaction, coupling of adsorbed methoxide groups gives rise to the CH_3OCH_3 product at 640 K. As will be discussed below, for the reaction of methanol on rutile-TiO_2 (R-TiO_2) this pathway has been attributed to the reaction of two methoxides adsorbed on a common surface Ti cation [6]. Finally, deoxygenation of adsorbed methoxides produces CH_4, also near 640 K. TPD data for the 18 nm and 22 nm platelets were qualitatively similar to those in Figure 5.4a for the 14 nm platelets and relative product yields for all three crystallite sizes are given in Table 5.1.

Table 5.1 Product yields for 2.5 L methanol dose

Nanocrystal Size and Shape	**CH_3OCH_3**	**CH_2O**	**CH_4**	**High-temp CH_3OH**	**H_2O**
14 nm platelets	0.0039	0.018	0.040	0.025	0.053
18 nm platelets	0.0025	0.021	0.034	0.033	0.023
22 nm platelets	0.0022	0.019	0.039	0.027	0.025
10 nm bipyramids	0.0023	0.012	0.003	0.031	0.011
25 nm bipyramids	0.0020	0.029	0.008	0.043	0.032

It is useful to compare these results with what we have reported previously for the reaction of methanol on thin films of the bipyramidal nanoparticles [115]. Representative methanol TPD results obtained from 10 nm bipyramids are given in Figure 5.4b. The data

in both panels of Figure 5.4 have been scaled to account for differences in surface area, as described in the experimental section. The relative product yields for two sizes of pyramids are also given in Table 5.1. These data show that while there are some similarities for the two nanocrystal morphologies, there are also some differences. The similarities include the methanol desorption curves which contain broad two-peak structures between 200 and 400 K along with smaller peaks near 500 and 650 K, H_2O production at 320 K, and CH_3OCH_3 and CH_4 production at 640 K. The relative yields of both CH_3OCH_3 and CH_4 on the bipyramids, however, was significantly less than that on the platelets.

The data in Table 5.1 show that for the platelets the yield of both CH_4 and CH_2O does not change appreciably with platelet size, after accounting for differences in the surface area of each sample. However, the yield of CH_3OCH_3 shows some size dependence. Figure 5.5 compares the CH_3OCH_3 yield during methanol TPD for both the platelet and bipyramidal samples as a function of the crystallite size. Note that for the platelets the 14 nm crystallites produced markedly more CH_3OCH_3 than the larger crystallites. Also, a similar size dependency was not observed for the bipyramids.

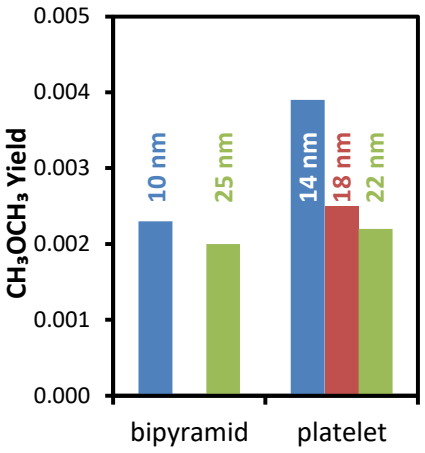

Figure 5.5 Dimethyl ether yield following a 2.5 L methanol dose as a function of nanocrystal size and shape. All yields have been normalized to account for differences in surface area.

5.3.3 Photochemical Reactions

Methanol TPD experiments were also used to investigate the photocatalytic activity of the A-TiO_2 nanocrystals. As described in the experimental section, for these experiments methanol-dosed samples at 160 K were exposed to 10^{15} cm^{-2} s^{-1} of 365 nm UV photons for a set time prior to each TPD run. Representative TPD results obtained following a 3 h UV exposure on both platelet (14 nm) and bipyramidal (10 nm) samples dosed with 2.5 L methanol are displayed in Figure 5.6a and Figure 5.6b, respectively. This data shows that the most significant change upon UV exposure is the production of the coupling product methyl formate ($HCOOCH_3$) which desorbs between 230 and 300 K. The yield of $HCOOCH_3$, however, is roughly the same on the 10 nm bipyramidal and 14 nm platelet nanocrystals following a 3 h illumination period. UV exposure also increases the CH_4 yield and attenuates the CH_3OCH_3 yield on the 10 nm bipyramids, but has little effect on the corresponding yields on the platelets.

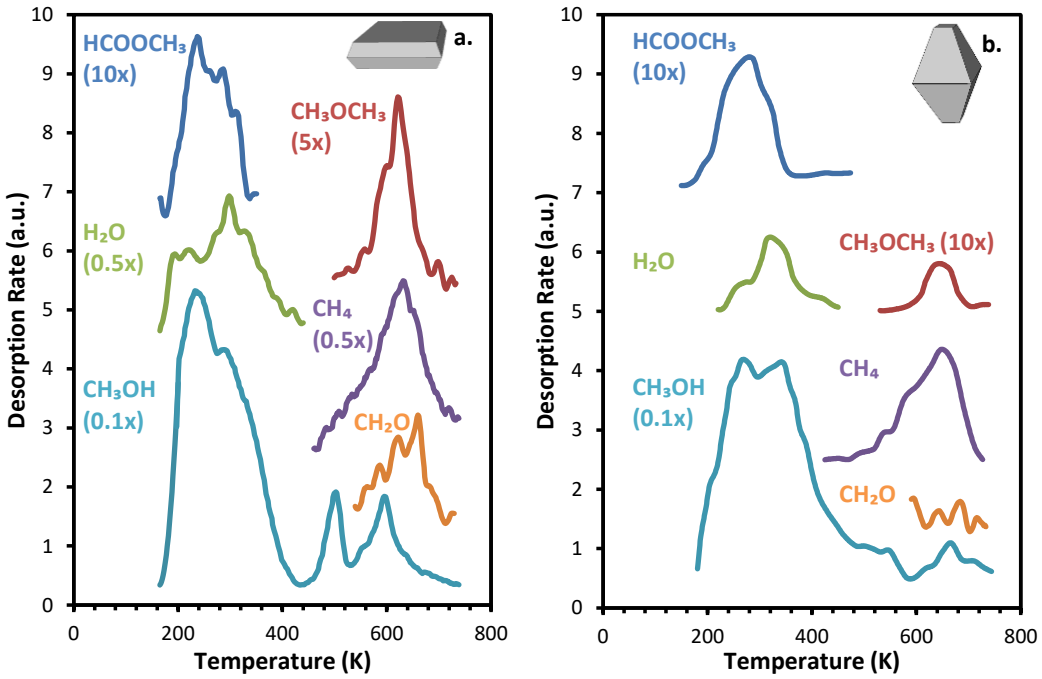

Figure 5.6 TPD results obtained from (a) 14 nm platelet and (b) 10 nm bipyramidal nanocrystal thin films dosed with 2.5 L of methanol at 160 K and exposed to 3 h of UV illumination. Desorption intensities have been scaled to account for mass spectrometer sensitivity and difference in surface area.

While the data in Figure 5.6 indicates that the $HCOOCH_3$ yield after a 3 h of UV exposure is roughly equivalent on the 10 nm bipyramids and on the 14 nm platelets, different trends in the production of this product as a function of the UV exposure were observed for the two crystallite morphologies. This is illustrated in Figure 5.7, which plots the $HCOOCH_3$ yield as a function of nanocrystal size versus UV exposure for the two different types of crystallites. For the platelets the $HCOOCH_3$ yield increases linearly with UV exposure. In contrast, for the bipyramids the yield initially increases with UV exposure, but after 2 h of UV exposure levels off or decreases. We have previously

attributed this decrease to photodecomposition of a portion of the $HCOOCH_3$ product [115]. Also note that the platelets, regardless of size, have a $HCOOCH_3$ yield that is similar to the 10 nm bipyramids, but much less than the 25 nm bipyramids.

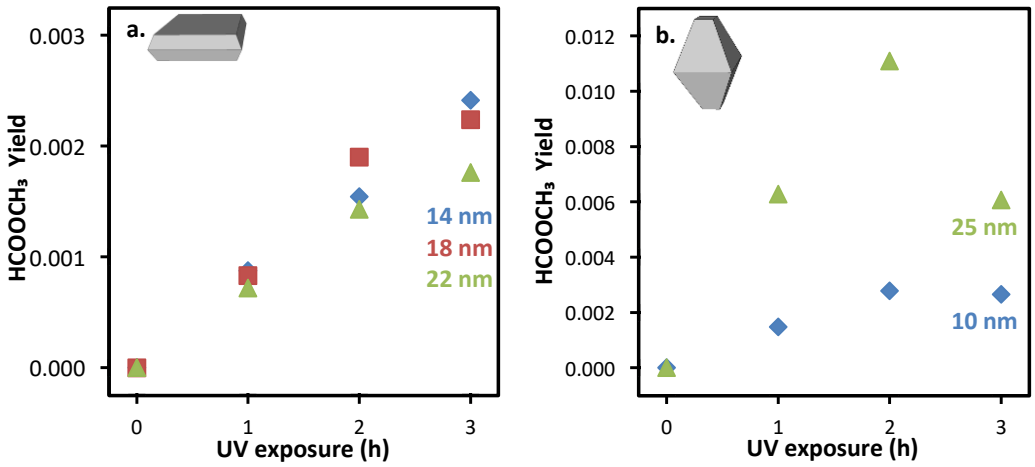

Figure 5.7 Methyl formate yield following a 2.5 L methanol dose from (a) platelet and (b) bipyramidal nanocrystal thin films as a function of UV exposure time and nanocrystal size and shape. All yields have been normalized to account for differences in surface area.

Analogous yield trends for CH_4 are given in Figure 5.8. As reported previously [115], a small amount of CH_4 is produced on the bipyramids in the absence of UV exposure, but the yield increases five- to ten-fold after 3 h of UV illumination. This suggests the existence of both thermal and photochemical pathways for CH_4 production on these nanocrystals. The platelets (Figure 5.8a), however, exhibit a much smaller increase in CH_4 yield with increasing UV exposure, suggesting the photochemical pathway is less significant on the platelets. On the other hand, CH_4 yields are still roughly comparable between the two shapes due to the much higher activity for the thermal

pathway on the platelets. Finally, photochemically-produced CH_4 yield does not change significantly with platelet size.

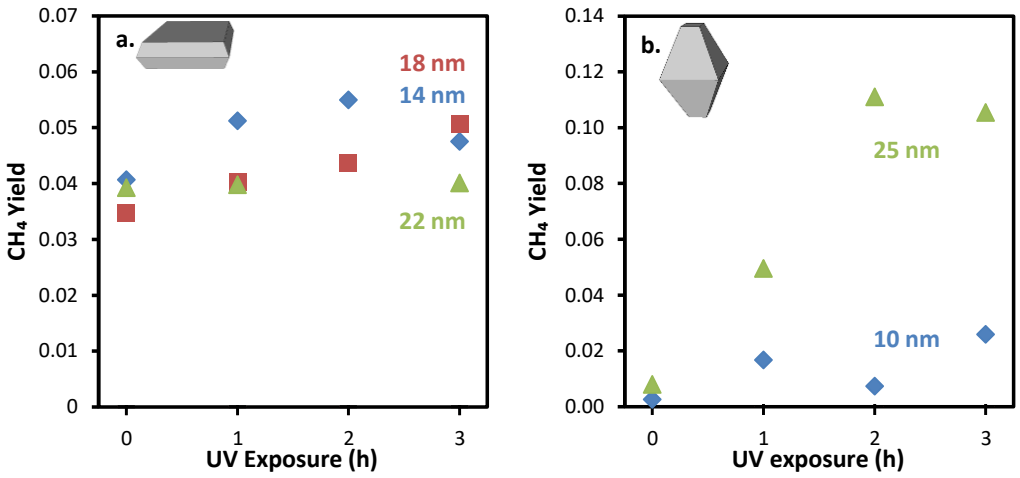

Figure 5.8 Methane yield following a 2.5 L methanol dose from the (a) platelet and (b) bipyramidal nanocrystal thin films as a function of UV exposure time and nanocrystal size and shape. All yields have been normalized to account for differences in surface area.

5.4 Discussion

To facilitate comparisons between the reactivity of the bipyramidal and platelet anatase nanocrystals, let us first review the results we reported previously for the bipyramidal system. Briefly, we found that the thermal and photochemical reactivity of methanol on the bipyramids which preferentially expose the {101} family of planes was similar to that reported for reaction on single crystal A-TiO_2(101) [115]. Methanol adsorbs molecularly on the fivefold coordinate Ti cations exposed on this surface and desorbs below 400 K without undergoing any detectible reactions. However, upon exposure to UV light a portion of the adsorbed methanol undergoes photo-oxidation and

coupling to produce $HCOOCH_3$ [76, 115]. As shown in Figure 5.4b, in addition to these pathways which can be attributed to the {101} surfaces, on the bipyramidal nanocrystals a small fraction of the methanol adsorbs dissociatively to produce methoxide groups which convert to CH_4 or undergo a coupling reaction near 640 K to produce CH_3OCH_3. The data indicated that these pathways occur primarily on sites located on the {001} capping planes.

While data for the reaction of methanol on single crystal A-TiO_2(001) surfaces is not available in the literature, the production of CH_4 and CH_3OCH_3 near 640 K during methanol TPD experiments has also been observed for {114}-faceted R-TiO_2(001) by Kim and Barteau [6]. Furthermore, these researchers demonstrated that the active site for CH_3OCH_3 production are exposed fourfold coordinate Ti cations and proposed that multiple coordination vacancies facilitate the coupling reaction by allowing two methoxide groups to bond to a common Ti site. As noted in the introduction, we have previously suggested that the active sites for CH_3OCH_3 production on the bipyramidal nanocrystals are located on the {001} capping planes. While fourfold coordinated Ti^{4+} cations are not present on the ideal A-TiO_2-(001) surface, this surface is unstable and undergoes a (1 x 4) reconstruction [8, 32]. The precise structure of this reconstruction is still subject to some debate [8, 30, 31, 33, 116], but a model proposed by Lazzeri and Selloni [34], in which TiO_3 species periodically replace rows of the bridging oxygens on the (1 x 1) surface, is the most energetically favorable and the most consistent with the available TPD data [31]. This reconstruction does contain fourfold coordinated Ti^{4+} but they are situated such that one of the coordination vacancies is not accessible to

adsorbates. Thus, one would not expect the A-TiO_2(001)-(4x1) surface to be active for the coupling of methoxide groups to produce CH_3OCH_3. Note, however, that the surface unit cell for this reconstruction spans 1.5 nm which is approaching the size of the {001} caps in the bipyramidal nanocrystals we have studied which vary from ~3-6 nm. We have suggested that the small size of the {001} surfaces relative to the length scale of this reconstruction may result in a different equilibrium structure for the {001} caps on the bipyramidal nanocrystals than that observed for bulk single-crystal surfaces and that this, yet to be determined, reconstruction exposes fourfold coordinated Ti^{4+} cations that are active for the coupling of methoxide groups to produce CH_3OCH_3 [6].

If this hypothesis is correct and the reconstruction of the (001) surface differs between very small facets (as on the caps of the bipyramids) and macroscopic single-crystalline anatase, one might expect the activity of the {001} facets in the nanocrystals to be crystallite-size dependent. As shown in Figure 5.5 this is indeed the case for the platelets where the yield of CH_3OCH_3 was found to decrease with increasing crystallite size. At first glance this conclusion may appear to be at odds with the bipyramid data in this figure, which does not show the same trend. Note, however, that these data are normalized to the total surface area of each nanocrystal film. If the yield data is instead normalized to the surface area of the {001} facets in each film and plotted versus the area of the (001) facet in each crystallite as is done in Figure 5.9, a strong dependence of CH_3OCH_3 yield during methanol TPD on the {001} facet size becomes apparent with the small {001} facets of the bipyramidal crystallites being much more active than those of the larger facets in the platelets. While we acknowledge that with only the limited data

presented here this conclusion is somewhat speculative, it does provide some support for the idea that reconstruction of oxide surfaces may in some cases depend on facet size. Of course other factors may also be playing a role here such as defect concentrations (e.g. oxygen vacancies) that vary with crystallite size and shape.

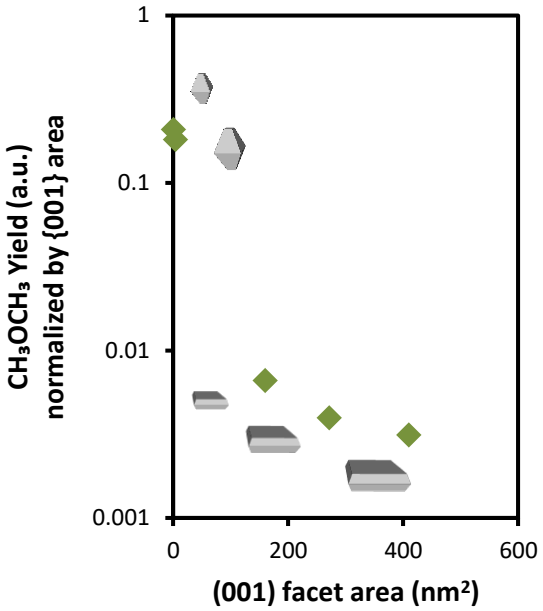

Figure 5.9 Dimethyl ether yield normalized by the available {001} surface area as a function of the area of a single (001) facet.

In contrast to the trends in CH_3OCH_3 production, the yield of thermally-produced CH_4 during methanol TPD is not very sensitive to particle size (see the 0 h points in Figure 5.8), but still depends on the nanocrystal shape with the platelets exhibiting higher yields than the bipyramids. Since the ratio of {001} to {101} surface area is roughly constant for a given nanocrystal shape, the most straightforward explanation for this trend

is that the thermal pathway for CH_4 production occurs on the {001} facets which are predominantly exposed on the platelets. A similar conclusion was obtained in our previous study of the reactivity of the bipyramids [115]. Also note that Kim and Barteau have proposed that CH_4 production on R-TiO_2 proceeds via deoxygenation of adsorbed methoxides on surface oxygen vacancies [6, 14, 43]. The fact that the oxygen vacancy formation energy is 0.3 eV less on the A-TiO_2(001) compared to the A-TiO_2(101) [117] provides further support that the reaction that produces CH_4 from methoxide groups on the A-TiO_2 nanocrystals proceeds primarily on sites on the exposed {001} surfaces. Finally CH_2O was produced via dehydrogenation of methoxide groups near 640 K during TPD on the both samples with the resulting hydrogen atoms reacting with remaining methoxides to re-form some methanol.

Differences are also observed in the photocatalytic activity of the platelets and bipyramids for the production of $HCOOCH_3$ from methanol. As noted in the introduction, our previous results for the bipyramidal nanoparticles [115] indicated that the active sites for photocatalytic production of $HCOOCH_3$ were located on the {101} facets. The data in Figure 5.7 show that the initial rate of $HCOOCH_3$ production on the platelets (regardless of size) during UV exposure is roughly 40% lower than that for the 10 nm bipyramids and 80% lower than that for the 25 nm bipyramids. Since the platelets expose a much lower fraction of {101} facets relative to the bipyramids, these data provide additional evidence that the active sites for photochemical production of $HCOOCH_3$ are on the exposed {101} surfaces.

In addition to the relative exposure of {101} and {001} surfaces affecting the amount of $HCOOCH_3$ produced, there are some more subtle differences in the photocatalytic activity of platelet and bipyramidal nanocrystals. Exposing the methanol-dosed bipyramidal nanocrystals to UV light also produced the following three trends in the TPD product distribution, each of which was less pronounced or nonexistent for the platelet nanocrystals: (1) photodecomposition of a portion of the $HCOOCH_3$ product as evidenced by the amount of $HCOOCH_3$ going through a maximum with UV exposure (see Figure 5.7), (2) an increase in CH_4 production with UV exposure, especially for larger crystallites (see Figure 5.8), and (3) a decrease in the CH_3OCH_3 and CH_2O yields with increasing UV exposure (compare Figure 5.4 and Figure 5.6). The first two trends may be due to the fact that the rate of photochemical production of $HCOOCH_3$ on the {101} surfaces of the bipyramids is greater than that on the corresponding surfaces of the platelets (see Figure 5.7). This would cause the concentration of $HCOOCH_3$ to saturate more quickly on the {101} surfaces of the bipyramids at which point photodecomposition of the $HCOOCH_3$, which produces adsorbed methyl groups, becomes the dominant reaction pathway. The faster rate of conversion of methanol to $HCOOCH_3$ on the {101} surfaces of the bipyramids compared to the platelets is likely related to the shape of the nanoparticles which causes photo-generated charge carriers in the bulk to have a higher probability of diffusing to a {101} surface on the bipyramids. The third trend, however, is more difficult to explain. By similar reasoning, one might expect that the rate of photodecomposition of the methoxide groups on {001} surfaces that react to produce

CH_3OCH_3 or CH_2O would be more rapid (at constant photon flux) on the platelets compared to the bipyramids, but just the opposite is observed.

We can only speculate as to the origin of this effect, but it is possible that the photocatalytic activity of the nanocrystals depends on cooperative effects between the {101} and {001} facets, in addition to individual contributions from each facet. A recent study by Liu et al. [83] provides some support for this possibility. In that study they measured the activity for photocatalytic water splitting for a series of truncated bipyramidal nanocrystals and found that the activity was highest on nanocrystals with ~15% exposed {001} facets, and decreased with higher or lower exposed fraction of these facets. Crystallites with platelet morphology similar to that used in the present study were found to be nearly inactive for the water splitting reaction. They argued that this trend was due to preferential migration of electrons and holes to separate facets on the TiO_2 nanocrystals, as has been reported in several other papers [42, 62, 81, 82]. Such separation of electrons and holes would reduce the rate of recombination resulting in an increase in quantum yield. This effect would be expected to be most pronounced when an electron-hole pair is generated in close proximity to a {101} – {001} intersection. Just based on the nanocrystal geometries, on average electron-hole pairs generated near a {001} facet on a bipyramid will be closer to one of these intersections than one near a {001} facet on a platelet. Thus, facet driven carrier separation may, on a per area basis, enhance the photochemical activity of the bipyramid {001} facets relative to those on the platelets. This may explain why photochemistry on the {001} caps of the platelets used in this study appears to be proportionally lower than that of the bipyramids.

In the studies of facet-driven charge carrier separation mentioned above [42, 62, 81-83], the {001} and {101} facets are reported as the primary destination of photo-generated holes and electrons, respectively. Since holes would be expected to participate in photo-oxidation reactions [9, 59], the {001} facets would provide the sites for this reaction. This is in contrast to what was observed in the present study where photo-oxidation of methanol to $HCOOCH_3$ was found to occur primarily on the {101} facets. It should be noted, however, that the assignment of photo-generated carrier destinations in the literature have been based, for the most part, on solution-phase photodeposition of metal ions [81, 82] which may not be applicable to the vacuum conditions used in the present study. While suspended in solution the surfaces of the A-TiO_2 nanocrystals are almost certainly –OH terminated, which is not the case for the vacuum-annealed samples used here. Indeed XPS studies of the electronic band structure of A-TiO_2 nanocrystals [118] correlated the abundance of {001} facets with a lower conduction band minimum, which suggests that, at least in vacuum, photo-generated electrons may preferentially segregate to this surface. Alternatively, an indirect photo-oxidation mechanism, such as that described by D'Arienzo et al. [62], may enable oxidation on the electron-rich facets. While some questions may still remain about the ultimate destination of the electrons and holes, the results of this and previous studies still indicate that preferential segregation of electrons and holes to different exposed facets occurs, and that this affects the overall photocatalytic activity.

Finally, we consider the effect of nanocrystal size on photocatalytic activity. As can be seen in Figure 5.7b and Figure 5.8b, the 25 nm bipyramids are considerably more

active than the 10 nm bipyramids for photochemical $HCOOCH_3$ and CH_4 production from methanol (or methoxide). Recall that these yields are normalized by the sample surface area. Since reactions occur on the surface but photon absorption occurs in the bulk, the normalized yield might be expected to scale with the volume-to-surface area ratio of the nanoparticles (at least until the nanocrystal size approaches the photon penetration depth). The size dependence of photocatalytic activity on the bipyramids follows this pattern closely enough to suggest that the volume-to-surface area ratio plays a role.

In contrast to the bipyramids, the platelets show no discernable size dependence for photochemical reactions. As discussed above, charge carriers generated further away from the photochemically active {101} surfaces (e.g., near the center of a platelet) are more likely to recombine prior to diffusing to this surface (precluding surface reactions) than those generated near this surface. For comparison, no point in the 25 nm bipyramid nanocrystal is further than ~6 nm from a {101} facet, while the center of even the smallest platelets is ~7 nm from one of these facets. It may even be that the volume near the center of the larger platelets is ineffective in providing photo-generated carriers to the {101} facets. In this case, the extra volume for photon absorption gained by the 18 nm and 22 nm platelets would be partially offset by the expanding 'dead volume' near the center. This would explain the lack of size effects for $HCOOCH_3$ production on the platelets. Alternatively, perhaps any size effects are too small to be observed over the ~3-fold volume increase from 14 nm to 22 nm platelets, while the ~15-fold volume increase from the 10 nm to 25 nm bipyramids makes these effects noticeable.

5.5 Conclusions

The results of this study of the reactivity of methanol on A-TiO_2 nanoparticles with platelet and bipyramidal morphology further demonstrate the crystal-plane dependent reactivity of A-TiO_2. In particular, we observed that the active sites for the production of CH_3OCH_3 from adsorbed methoxide groups are located on the {001} surfaces while those for the photochemical oxidation and coupling of adsorbed methanol and methoxide groups to produce $HCOOCH_3$ are located on the {101} surfaces. This causes the platelet nanocrystals to be more active for the production of CH_3OCH_3, and the bipyramidal nanocrystals to be more active for the photochemical reaction that produces $HCOOCH_3$. A dependence of the reactivity on the facet size was also observed with the smallest {001} facets being active for the coupling of methoxide groups to produce CH_3OCH_3 which is not observed on the extended (001) surfaces of macroscopic A-TiO_2 single crystals. This observation indicates that the complex reconstructions which occur on the A-TiO_2(001) surface may be facet-size dependent.

The bipyramidal nanocrystals were also found to be more active than the platelet nanocrystals for all photochemical reactions observed, including those occurring on the {001} planes, such as the depletion of methoxide precursors which would otherwise react to form CH_3OCH_3 on this surface. This points to a difference in the intrinsic photochemical activity of both morphologies, rather than a simple matter of active site abundance and is consistent with the idea that the ratio of exposed {101} and {001} surface area plays a key role in TiO_2 photocatalysis as suggested in several previous

studies [42, 62, 81-83]. Specifically, facet-driven charge carrier separation may play a role in enhancing the photocatalytic activity of bipyramidal nanocrystals relative to platelet nanocrystals. Thus the relative proximity of dissimilar planes may be an important parameter for the design of highly-active photocatalytic anatase nanoparticles. It was also shown that larger bipyramids have increased photocatalytic activity over smaller bipyramids, indicating that the ratio of volume to surface area is important. Thus, there may be an optimal particle size for any given photochemical reaction which balances higher photon absorption for larger sizes with the higher surface area and more active sites at lower sizes.

Finally this study highlights the utility of thin films of well-defined nanocrystallites as model catalysts in fundamental studies of structure-activity relationships for metal oxides and further demonstrates how this approach can help bridge the materials gap between studies of single crystals and high surface area catalytic materials.

Chapter 6. Exceptional Thermal Stability of Pd@CeO_2 Core-Shell Catalyst Nanostructures Grafted onto an Oxide Surface[10]

Summary

This publication is not directly related to the TiO_2 project which has been the focus of this thesis so far. It was the result of an early collaboration with members of the Raymond Gorte lab in the Chemical Engineering department who sought to demonstrate a technique for dispersing nanostructured core-shell catalyst particles onto a planar surface. These particles have considerable inherent thermal stability which makes them well-suited for high temperature applications such as solid oxide fuel cells, but they tended to agglomerate upon dispersal rather than form into thin, uniform films. The dispersal of nanostructured catalysts into thin films and subsequent analysis in UHV by TPD and XPS set the stage for the later TiO_2 project which forms the core of this thesis.

[10] This chapter was published as Adijanto, L.; **Bennett, D. A.**; Chen, C.; Yu, A. S.; Cargnello, M.; Fornasiero, P.; Gorte, R. J.; Vohs, J. M., *Nano Let.* 13 (2013) 2252-2257

6.1 Introduction

For many technologically important chemical processes which employ supported noble metal catalysts, loss of metal surface area due to sintering limits catalyst lifetime and efficiency. Encapsulating the metal nanoparticles in a thin porous oxide shell has been proposed as one means to alleviate this problem and improve catalyst lifetime [119-130], although methods to disperse these core-shell structures onto high surface area oxide supports still presents a challenge. In this study we demonstrate the growth of highly dispersed, monolayer films of catalytically active Pd@CeO_2 core-shell nanocomposites onto a planar, single crystal YSZ(100) (yttria stabilized zirconia) support using an alkyl-silane coupling agent, and that these films exhibit exceptional thermal stability with high Pd dispersion being maintained even after calcination in air at temperatures in excess of 1000 K. The general utility of this approach for the synthesis of dispersed core-shell catalysts on high surface area oxide supports is also demonstrated.

6.2 Materials and Methods

6.2.1 Materials

Triethoxy(octyl)silane (TEOOS, Sigma Aldrich 97.5 %), $Pd(NO_3)_2{\cdot}2H_2O$ (40 % as Pd), $(NH_4)_2Ce(NO_3)_6$ (99.99 %). n-Tetradecylphosphonic acid (TDPA, ≥97 %) was purchased from Strem Chemicals. Al_2O_3 Puralox TH100/150 (90 $m^2\ g^{-1}$) was purchased from Sasol and calcined at 1173 K for 24 h. Pd@CeO_2 structures (at 1:9 Pd/Ce weight ratios) were prepared according to the procedure described in detail elsewhere [128, 131]. YSZ(100) single crystal substrates with dimensions of 5 mm x 5 mm were purchased

from MTI corporation. All of the solvents were reagent grade from Sigma-Aldrich and used as received. The Pd@CeO_2 structures (1:9 Pd/Ce weight ratio) were synthesized using the procedure described in our previous publications [128, 131].

6.2.2 Preparation of samples

The YSZ(100) single crystal substrates (5 mm x 5 mm) were cleaned using an O_2 plasma treatment prior to surface modification. Functionalization of the YSZ(100) surface via reaction with triethoxy(octyl)silane (TEOOS) was performed using chemical vapor deposition (CVD) system. Prior to film deposition, the YSZ(100) substrate was further cleaned in the CVD reactor by heating to 673 K and exposure to 400 torr of O_2 for 1 min. The sample was functionalized with TEOOS using ten deposition cycles consisting of a 1 min exposure to 0.5 torr of TEOOS with the sample at 323 K. The Pd@CeO_2 particles were added (in excess of that required for a monolayer) to the clean and TEOOS-functionalized YSZ(100) surfaces using ten cycles of placing a 0.1 ml drop of the $1.5x10^{-3}$ M Pd@CeO_2/THF solution onto the YSZ(100), waiting 2 minutes, and then rinsing with THF. The samples were then calcined to 723 K in air for 4 hrs to remove the alkyl groups.

For the TEOOS treated sample, γ-Al_2O_3 powder (1 g) was mixed in 20 mL of toluene followed by addition of TEOOS (0.55 mL). The resulting solution was refluxed at 384 K for 6 hrs and the precipitate powder was recovered by centrifugation. For the TDPA-treated sample, γ-Al_2O_3 powder (1 g) was mixed in 30 mL of THF followed by addition of TDPA (0.20 g). The resulting solution was refluxed at 333 K for 6 hrs and the

precipitate powder was recovered by centrifugation. The powder was subsequently washed twice with toluene/THF to remove unreacted TEOOS/TDPA and byproducts and was dried overnight at 393 K.

The appropriate amount of $Pd@CeO_2$ structures was added to the hydrophobic γ-Al_2O_3 well dispersed in THF (15 mL). Although a complete adsorption occurred almost immediately when using loadings of Pd and ceria of 1 and 9 wt. % or less, respectively, the mixture was left stirring overnight. The solid residue was recovered by centrifugation and washed twice with THF. Finally, the powder was dried at 403 K overnight, ground to a particle size below 150 μm and calcined in air at 1123 K for 6 hrs using a heating ramp of 3 K min^{-1}.

6.2.3 Characterization techniques

The surface topography was measured in air using an AFM (Pacific Nanotechnology) operated in close-contact (tapping) mode. XPS and TPD measurements were conducted in an ultra-high vacuum (UHV) surface analysis chamber with a base pressure of 2 x 10^{-10} Torr. Sample heating in UHV was accomplished through conduction from a resistively heated tantalum foil sample holder, and the temperature was monitored using a type K thermocouple that was attached to the back surface of the YSZ crystal using a ceramic adhesive (Aremco). Samples were exposed to adsorbates through a dosing needle with the sample positioned directly in front to maintain a low base pressure. The hydrophobicity of the YSZ(100) substrate before and after TEOOS deposition was measured by pendant drop Tensiometry (Attension, Theta), and the

thickness of the TEOOS/Pd@CeO_2 layer was measured using an Alpha-SE ellipsometer (J.A. Woollam).

6.2.4 Catalytic tests

Methane oxidation experiments were performed in a 6.4 mm diameter, tubular quartz reactor, using ~0.10 g of catalyst. The reactants (0.5 % CH_4, 5 % O_2, balance N_2) at 1 atm were flowed over the catalyst at a rate 120 mL/min. The CH_4 conversion was kept below 10% so that differential conditions could be assumed. Products were analyzed using an on-line gas chromatograph. Prior to measuring rates, each catalyst was pressed into wafers, heated to 693 K under flowing He and cleaned under a flow of 20%O_2/80%He at 120mL/min for 30min.

6.3 Results and Discussion

Pd@CeO_2 nanostructures were chosen as the subject of this investigation because synergistic interactions between Pd and CeO_2 are known to enhance catalytic activity for industrially important reactions ranging from water gas shift to hydrocarbon oxidation. The Pd@CeO_2 nanostructures consisted of a 2 nm diameter Pd core surrounded by a 3 nm thick, porous CeO_2 shell, and were synthesized in THF solution using the procedure developed by Cargnello et al. [127, 128, 131]. The surface of the Pd@CeO_2 particles was functionalized with dodecanoic acid in order to both control particle size during synthesis and inhibit particle agglomeration in solution. Unfortunately, this hydrophobic alkyl

capping layer is repelled by the hydrophilic surface of most oxide supports, including the YSZ(100) single crystal and high surface area γ-Al_2O_3 supports used here. Due to this repulsive particle-surface interaction, the core-shell particles assemble into large agglomerates when they are deposited by incipient wetness onto high surface area metal oxide powders or by drop casting onto planar supports. We have overcome this problem by functionalizing the surface of the oxide support with hydrophobic long-chain alkyl groups via deposition of a monolayer of triethoxy(octyl)silane (TEOOS) or n-tetradecylphosphonic acid (TDPA) as described in the supporting information (characterization data for the silanated YSZ(100) surface is also provided in the supporting information). As will be shown below, monolayer films of Pd@CeO_2 particles can be grafted onto the alkyl-functionalized oxide surfaces.

Figure 6.1 provides an overview of the preparation of the planar Pd@CeO_2/YSZ(100) samples used in this study. Following CVD of a TEOOS layer, the Pd@CeO_2 nanostructures were added to the YSZ(100) surface using several deposition cycles consisting of placing a 0.1 ml drop of the $1.5x10^{-3}$ M Pd@ CeO_2/THF solution onto the YSZ(100), waiting 2 minutes, and then rinsing with THF to remove weakly adsorbed particles. The sample was then calcined at 723 K in air for 4 hrs in order to oxidatively remove the alkyl groups on both the support and core-shell particles. A Pd@CeO_2/YSZ(100) sample for which the YSZ(100) substrate was not functionalized with TEOOS prior to deposition of the nanoparticles was also prepared in a similar manner. For comparison purposes, a sample consisting of Pd nanoparticles without a CeO_2 shell supported on YSZ(100) was also prepared. The synthesis procedure for this

sample was identical to that of the Pd@CeO_2/YSZ(100) sample except dodecanethiol-capped 2 nm Pd particles were used.

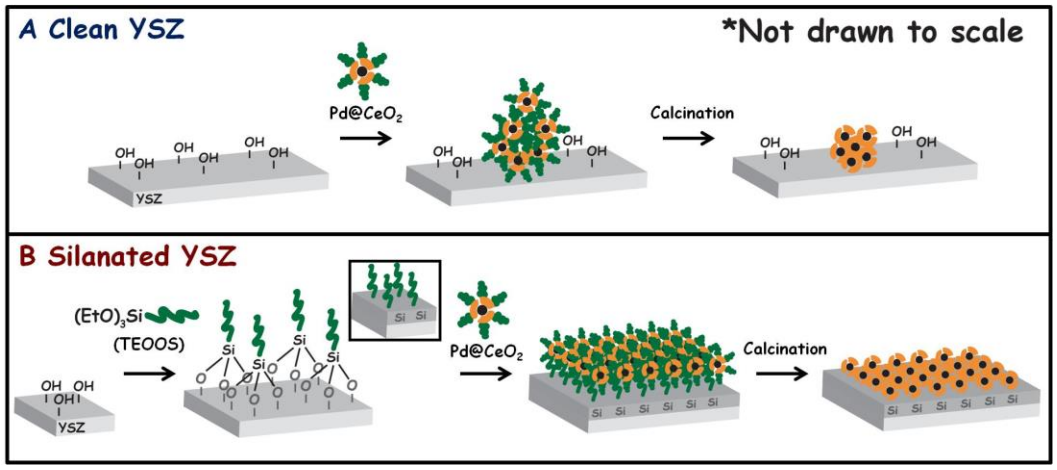

Figure 6.1 Overview of the deposition of Pd@CeO2 nanostructures on (A) clean YSZ(100) and (B) alkyl-siloxane functionalized YSZ(100). On clean YSZ the hydrophobic, alkyl-capped Pd@CeO_2 particles are repelled by the hydrophobic OH-terminated YSZ surface, resulting in the formation of agglomerates during deposition, with further agglomeration occurring upon calcination in air. On the alkyl-siloxane functionalized YSZ surface, the Van der Waals interactions between the capping alkyl groups on the surface and the core-shell particles directs the formation of a monolayer film of the Pd@CeO_2 particles. This Pd@CeO_2 layer is highly stable and remains higher dispersed upon calcination in air.

AFM was used to characterize the distribution of the Pd@CeO_2 structures that were deposited onto the pristine and functionalized YSZ(100) surfaces. As a base case for comparison, the interaction of the Pd@CeO_2 nanostructures with the pristine YSZ(100) surface will initially be considered. A 5 μm by 5 μm topographic AFM image of the surface of this sample, along with several representative line scans are shown in Figure 6.2A. Note that the image is relatively free of features except for several randomly distributed, large structures that are 0.5 to 1.5 μm in lateral dimension and 20 to 50 nm in

height. These features were not observed prior to exposure to the Pd@CeO_2/THF solution and are much larger than an individual Pd@CeO_2 particle; we, therefore, attribute them to large agglomerates of the Pd@CeO_2 particles. This result is consistent with repulsive interactions between hydrophobic alkyl-group capped Pd@CeO_2 particles in the deposition solution and the hydrophilic YSZ(100) surface, and illustrates the difficulty in obtaining a high dispersion of metal-metal oxide, core-shell catalysts on an oxide support using standard infiltration techniques.

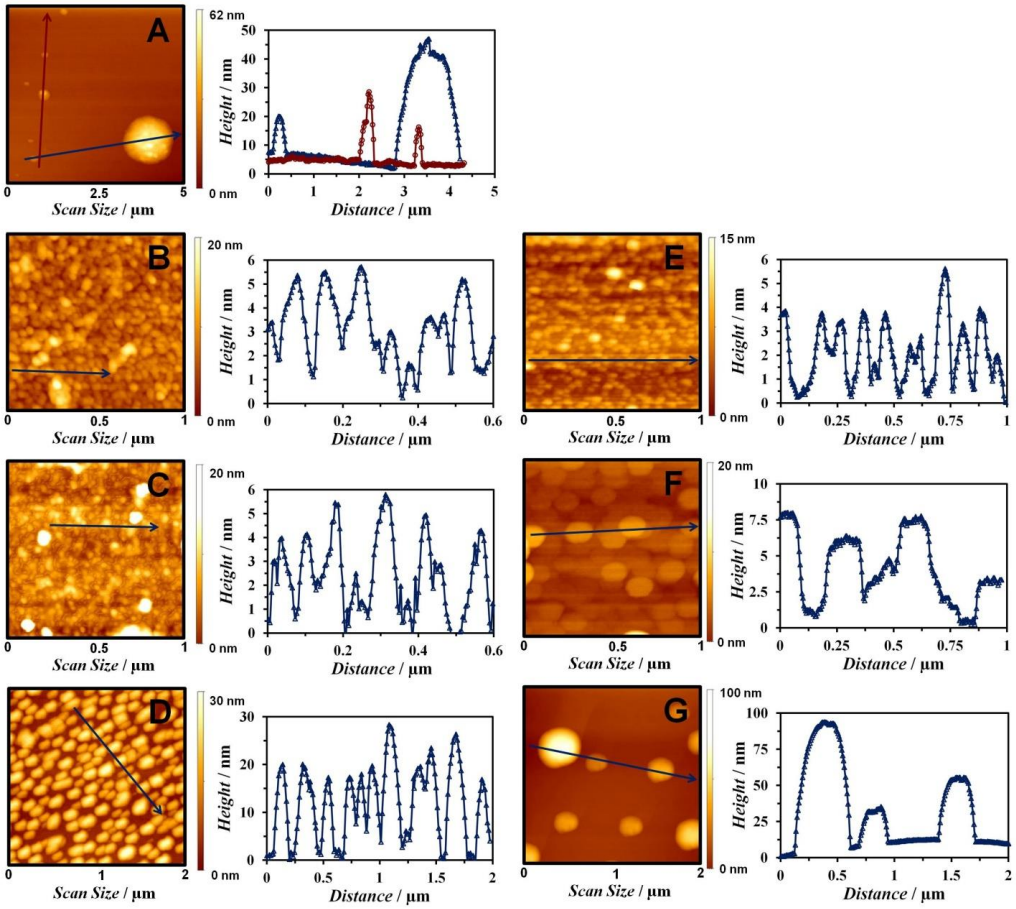

Figure 6.2 AFM topography images with representative line scans for Pd@CeO2 and Pd nanoparticles deposited on clean and alkyl-silanated YSZ(100) Panel A corresponds to $Pd@CeO_2$ deposited on pristine YSZ(100) calcined in air at 723 K. Panels B, C, and D correspond to $Pd@CeO_2$ desposited on alkyl-siloxane functionalized YSZ(100) after calcination in air at (B) 723 K, (C) 973 K, and (D) 1373 K. Panels E, F, and G correspond to Pd nanoparticles deposited on pristine YSZ(100) after calcination in air at (E) 723 K, (F) 973 K, and (G) 1373 K. Comparison of the images for the $Pd@CeO_2$ and Pd nanoparticles clearly demonstrates the high thermal stability of the $Pd@CeO_2$nanoparticles.

As shown by the 1 µm by 1 µm AFM image in Figure 6.2B, significantly different results were obtained for the TEOOS-treated YSZ(100) surface. For this sample following calcination at 723 K in air to remove the alkyl groups, the AFM image contains a relatively uniform, well-dispersed layer of nanoparticles. Analysis of the line scans

shows that the height of the particles is between 4-6 nm, which compares favorably with the diameter of the Pd@CeO_2 nanostructures of ~8 nm as determined by high-angle annular dark field, scanning transmission electron microscopy (STEM) and X-Ray Diffraction (XRD) [127], demonstrating that the majority of the surface is covered by a single layer of the particles, although a few small agglomerates are also present in the image. (Note that the apparent lateral dimension of the particles in the AFM image represents a convolution of the diameter of each particle and that of the AFM tip and is therefore not representative of the actual particle diameter.) The thickness of the core-shell particle film was also estimated to be 7 nm by ellipsometry (see supporting information), further corroborating this conclusion. These AFM results clearly show that the dodecanoic acid-capped Pd@CeO_2 nanostructures can be grafted onto the octyl-siloxane coated YSZ(100) surface, and that the distribution of the nanostructures can be maintained upon calcination in air at 723 K.

To investigate the thermal stability of the dispersed Pd@CeO_2 layer, the sample in Figure 6.2B was annealed in air to a series of successively higher temperatures and reexamined by AFM. The 1 μm by 1 μm image in Figure 6.2C was obtained after calcining in air at 973 K for 4 hrs. The features in this image are similar to those in the image of the 723 K calcined sample. There is no evidence of significant agglomeration of the Pd@CeO_2 particles and the line scans still give an average particle diameter of ~5 nm. As shown by the 2 μm by 2 μm AFM image in Figure 6.2D, calcination in air at 1373 K did cause some changes in the structure of the Pd@CeO_2 film. For this severe calcination temperature, the line scans indicate that the surface is covered with structures

that are approximately 15 to 25 nm in height. Assuming that the individual Pd@CeO_2 particles retain their shape (~5 nm per particle), these structures consist of agglomerates containing 5 to 8 Pd@CeO_2 particles. It is noteworthy that while some agglomeration of the Pd@CeO_2 particles has clearly occurred, the overall dispersion of the Pd remains high.

The exceptional thermal stability of the Pd@CeO_2 nanostructures and their resistance to sintering on TEOOS-treated surfaces becomes readily apparent when one compares the AFM images of the Pd@CeO_2/YSZ(100) sample in Figure 6.2B-D to those obtained from the TEOOS-treated YSZ(100) surface on which Pd nanoparticles without a ceria coating were deposited, Figure 6.2E-G. Note that for the latter sample after calcining in air at 723 K to remove the capping alkyl groups, the surface is covered with a high dispersion of particles that are ~3 nm in height (Figure 6.2E). The as-synthesized Pd particles are only 2 nm in diameter so the larger size observed here is either due to a volume expansion that occurs upon oxidation of the Pd or to partial sintering upon heating to 723 K. Extensive sintering of the Pd particles is observed, however, upon heating to 973 K (Figure 6.2F), where the average Pd particle size has increased to ~6 nm in height with a lateral dimension approaching 0.25 μm, indicating the agglomeration of the as-deposited, 2 nm diameter Pd nanoparticles into extended two-dimensional raft structures. Note that for these conditions little to no sintering of the Pd@CeO_2 particles was observed. Upon calcining to 1373 K additional sintering of the Pd particles is readily apparent with the 2 μm by 2 μm AFM image in Figure 6.2G showing only a few particles that are 0.25 to 0.5 μm in diameter.

The chemical and thermal stability of the ceria shell in the Pd@CeO_2 particles was also investigated using x-ray photoelectron spectroscopy (XPS). C(1s) and Ce(3d) XP spectra of a Pd@CeO_2/YSZ(100) sample calcined in air at 723 K and 973 K, and then subsequently annealed in ultra-high vacuum (UHV) at 700 K were collected. No C(1s) signal was detected, confirming the oxidative removal of the capping alkyl groups. The Ce(3d) spectra in Figure 6.3 contains peaks labeled u and v which correspond to the $3d_{3/2}$ and $3d_{5/2}$ spin-orbit states of the cerium cations, respectively, with the u'''/v''' doublet being due to the primary photoemission from Ce^{4+} cations, and the associated u/v and u''/v'' doublets being shakedown features resulting from transfer of electrons during photoemission from filled O(2p) orbitals to empty Ce(4f) orbitals [132]. Ce^{3+} cations give rise to the u'/v' (primary photoemission) and u^o/v^o (shakedown) doublets. The spectrum of the 723 K, air calcined sample (Figure 6.3A) contains a mixture of Ce^{3+} and Ce^{4+}. Based on the reported thermodynamic properties of bulk and polycrystalline ceria, for the conditions used in these experiments the CeO_2 would be expected to be fully oxidized (i.e. Ce^{4+}) [133-135]. The appearance of both Ce^{3+} and Ce^{4+} in the spectrum of this sample, therefore, indicates that the nano-structured ceria shells in the Pd@CeO_2 particles in this sample are more reducible than normal catalytic forms of CeO_2. In contrast, the XP spectrum of the 973 K, air calcined sample (Figure 6.3B) contains primarily Ce^{4+}, demonstrating that this treatment makes the ceria less reducible and more bulk like. This result is noteworthy since reactivity studies of supported Pd@CeO_2 catalysts have shown that high oxidation activity is obtained only after calcining in air to temperatures in excess of 1123 K [127]. More study is needed to determine the origin of this effect, but it

may be due to a change from an amorphous to more crystalline ceria shell upon high-temperature air calcination.

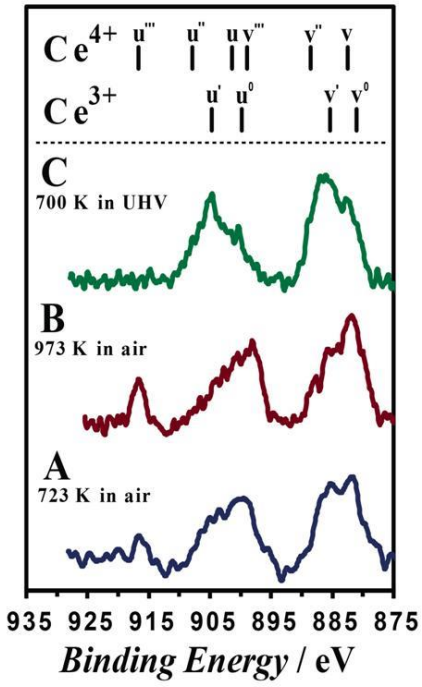

Figure 6.3 Ce(3d) XP spectra obtained from Pd@CeO2 deposited on alkyl-siloxane functionalized YSZ(100) after calcination under different conditions. The sample was calcined in air at 723 K (A) and 973 K (B), and in ultra-high vacuum at 700 K (C).

While the 973 K air-calcined sample appears to be less reducible than the 723 K air-calcined sample, it is still more easily reduced than that of bulk CeO_2. This is demonstrated by the spectrum in Figure 6.3C which shows that heating this sample to 700 K in UHV was sufficient to reduce all the Ce^{4+} to Ce^{3+} (i.e. reduction of CeO_2 to Ce_2O_3) in spite of the fact that under UHV conditions, bulk CeO_2 is thermodynamically stable at this temperature [133-135]. Furthermore, CO temperature-programmed

desorption (TPD) measurements indicate that significant structural rearrangement of the oxide shell occurs upon reduction. CO desorption spectra obtained from the 973 K air calcined and 700 K UHV annealed samples dosed with 50 L of CO at 260 K are shown in Figure 4. For the air calcined sample, CO and a smaller amount of CO_2 (not shown in the figure) desorb at 440 K, which is the expected temperature for CO desorption from Pd [136]. In contrast, CO was found not to adsorb on the 700 K vacuum annealed sample. This demonstrates that the metal is not accessible in this sample and suggests that, upon reduction, the ceria shell losses its porosity and completely encapsulates the underlying Pd nanoparticle as shown schematically in Figure 6.4. This result is in concordance with previous studies of CO adsorption on high surface area supported $Pd@CeO_2$ catalysts [129].

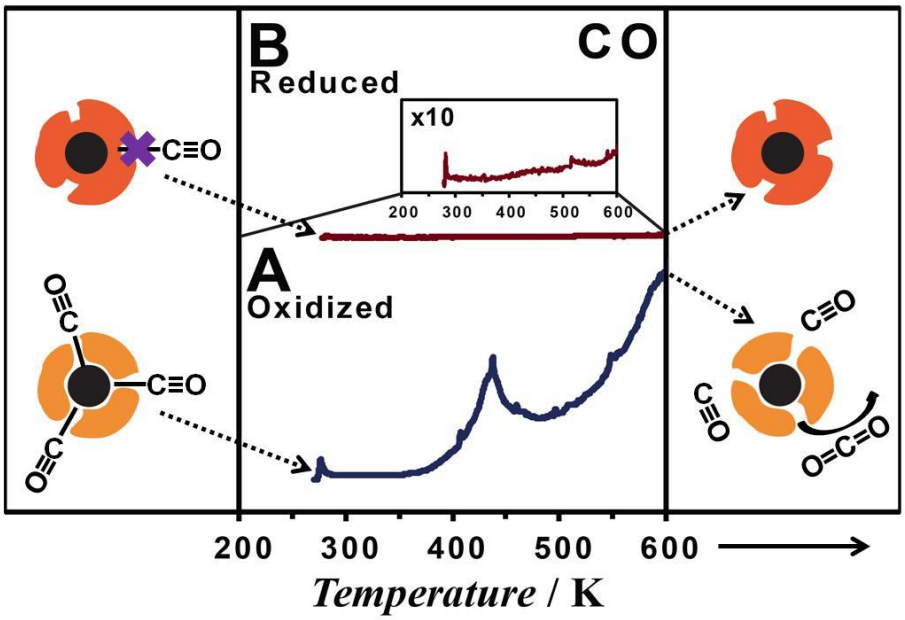

Figure 6.4 CO-TPD data and schematic representation of changes in shell morphology for oxidized and reduced Pd@CeO2/YSZ(100) catalysts. The CO-TPD results obtained after 50 L CO dose at 260 K on Pd@CeO2 deposited on silanated YSZ(100) calcined at (A) 973 K in air and (B) 700 K in vacuum. The y-axis in the figure corresponds to the m/e 28 mass spectrometer signal in arbitrary units. The two spectra have been offset to facilitate comparison.

While the AFM results presented above vividly demonstrate the high thermal stability of Pd@CeO_2 particles grafted onto a TEOOS-coated YSZ(100) surface, one must recognize that this method for dispersing the particles results in a siloxane interlayer between the support and the core-shell particles that may alter catalytic properties. For example, Rocchini et al. have shown that Si impurities can significantly enhance the reducibility of ceria [137]. For some applications, such as electrodes in solid oxide fuel cells, the siloxane layer may also interfere with other properties such as oxygen ion transport through the electrolyte [138-140]. In order to investigate the influence of the SiO_x layer on catalytic properties, we compared the rates of methane oxidation over

catalysts consisting of Pd@CeO_2 particles grafted onto a high surface area γ-Al_2O_3 support that was pre-treated with either TEOSS or TDPA. Like TEOSS, TDPA reacts with hydroxyl groups on the oxide surface to form a hydrophobic, alkyl-functionalized phosphonate layer onto which the Pd@CeO_2 particles can be grafted; however, unlike the siloxane linkage, the phosphate group is removed upon calcination in air at 1123 K resulting in the Pd@CeO_2 particles being directly adsorbed on the γ-Al_2O_3 surface. Figure 6.5 shows rate data for CH_4 oxidation over the Pd@CeO_2/TEOSS/Al_2O_3 and Pd@CeO_2/TDPA/Al_2O_3 samples that had previously been calcined in air at 1123 K. Note that similar rates were obtained for both samples indicating that the siloxane layer does not influence the catalytic properties of the supported Pd@CeO_2 particles and is also not required to maintain their high dispersion. Thus, it appears that direct interaction of CeO_2 shell with the support, possibly through the formation of Al-O-Ce linkages is sufficient to prevent sintering upon high-temperature calcination. It is also noteworthy that, consistent with previous reports for Pd@CeO_2, the rates from these catalysts were found to be an order of magnitude higher than that obtained from a conventional 1 wt. % Pd/CeO_2 catalyst [127].

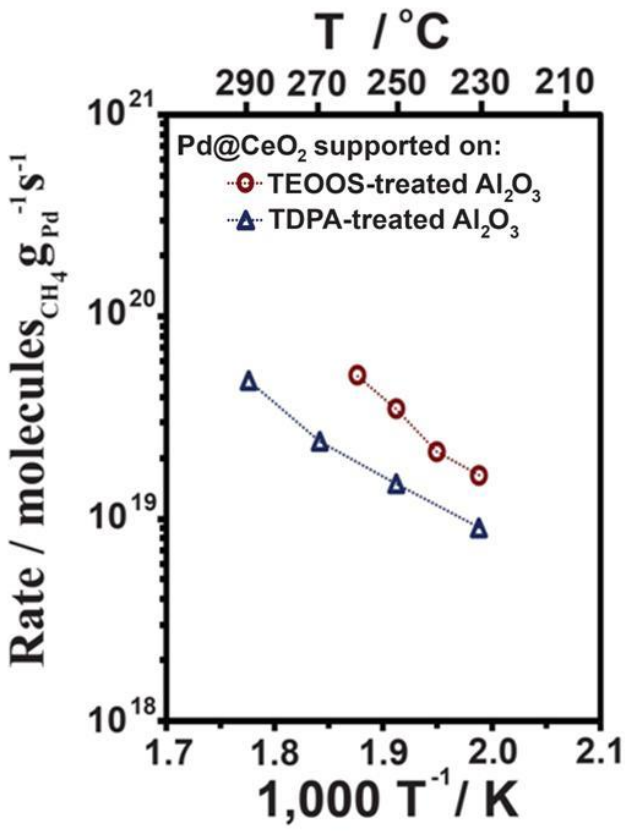

Figure 6.5 Reaction rate data for CH4 oxidation. Pd@CeO2 core-shell catalyst supported on (◯) TEOOS-treated □-Al2O3 and (Δ) TDPA-treated □-Al2O3 calcined in air at 1123 K for 6 hrs prior to rate measurements. The Pd weight loading in each catalyst was 1 %.

6.4 Conclusion

In conclusion, the results of this study demonstrate that monolayer films of $Pd@CeO_2$ core-shell, nanocomposites can be produced on a planar YSZ(100) support using alkyl coupling agents, and that these films exhibit exceptionally high thermal stability and resistance to sintering compared to bare Pd particles on the same support. The AFM images provide a direct measure of dispersion and show little to no sintering of the $Pd@CeO_2$ particles occurs for temperatures up to 973 K, with only moderate sintering

at temperatures as high as 1373 K. The high activity of Pd@CeO_2 nanostructures grafted onto γ-Al_2O_3 following calcination to 1123 K also demonstrates that this stability is maintained even when high surface area supports are employed. Additionally it was shown that the ceria shells in these nanostructures have unique properties being more reducible than bulk ceria which may play a role in the high activity of these materials for some reactions, such as methane combustion.

Chapter 7. Conclusions

7.1 Summary

This project has demonstrated the viability of using thin films of well-defined nanocrystals to help bridge the materials gap in heterogeneous catalysis and to contribute towards new structure-activity relationships. Methanol reactivity on the TiO_2 nanocrystals could be understood, to some extent, within the framework of the single-crystal literature. In other words, nanocrystals exposing primarily {101} surface area behaved roughly like A-(101) single crystals. However there were several more subtle thermal- and photochemical trends which required considering the effects of nanocrystal size and shape. (1) The platelet nanocrystals were more selective towards the bimolecular coupling product dimethyl ether. This is consistent with the assignment of fourfold coordinate cations on the {001} surfaces as the active sites for this reaction. (2) If this active site assignment is correct, then the activity for dimethyl ether production is not constant across all {001} surfaces, but is in fact higher on the smallest facets. This suggests that the form of the (1 x 4) surface reconstruction may be size-dependent. (3) UV exposure decreased dimethyl ether yields, but the extent of this effect is highly sensitive to nanocrystal shape. It was proposed that cooperative effects between the {101} and {001} facets account for the higher photoactivity on the {001} facets of the bipyramids. (4) Methyl formate was produced on all size and shapes of nanocrystals, but selectivity was higher on the bipyramids. This agrees with the assignment of {101} surfaces as the active site of this reaction. (5) Methyl formate production was much

higher on the large bipyramids, likely due to the increased volume with which to absorb photons (6) Methyl formate yields were observed to decrease at longer exposure times, indicating photodecomposition of the adsorbed species. This pathway was more significant on the large bipyramids. (7) Lastly, methane production occurred through two parallel channels. A non-photochemical pathway was attributed to dissociative adsorption on the {001} surfaces and was the dominant pathway for methane production on the platelets. (8) The photochemical channel was more significant on the bipyramids. The source of this methane is not entirely clear, but it most likely originates as surface methyl groups left over from photodecomposition of methyl formate and the precursors of dimethyl ether.

Admittedly, many of those structure-activity relationships are specific to these nanocrystals, at least when taken at face value. However, broader implications about the reactivity of oxygenates on TiO_2 nanoparticles may still be gleaned from these conclusions. For instance, it is clear that there is an optimal particle size for any given photocatalytic process which balances photon absorption and surface sites abundance. It also appears that the ratio of surface areas of different facets is a key determiner of photoactivity, and that facets that play no direct role in the surface chemistry for a certain reaction may still play a part in the over photocatalytic process. Lastly, the idea that the form of the surface reconstruction may depend on facet size has implications for the application of model catalyst studies to industrial catalysts. These findings may guide the process of applying fundamental knowledge from the vast body of single-crystal TiO_2 literature onto commercially-relevant systems. In a broader sense, this project

demonstrates the viability of surface science studies of well-defined, nanostructured metal-oxide materials to bridge the materials gap in catalysis.

7.2 Project Continuation

As is usual in the course of research, any new knowledge brings a collection of new questions. There are a few questions in particular that would provide valuable insight into the reaction mechanisms of methanol on these TiO_2 nanocrystals. Specifically, it was observed that all of the photochemical pathways observed during these experiments were most active on the 25 nm (largest) bipyramids, indicating a strong dependence on nanoparticle size. These photochemical trends (including those occurring on the {001} facets) were less active on the platelets, indicating a shape-dependence as well. Interestingly, the platelet photoactivity showed no strong size effects (in stark contrast to the bipyramids). Simply identifying these trends on their own is useful for catalyst design, but exploring the underlying mechanisms would provide insight into the nature of photocatalysis itself.

We developed tentative mechanisms for all of the observed trends based on the available literature on TiO_2 photocatalysis (section 5.4). These hypotheses were not testable with the surface science techniques available to us. However, transient absorption spectroscopy would allow us to probe the nature of the excited state in each of these types of nanocrystals. These techniques work by irradiating the sample with a pair of pulses of light mere femptoseconds apart. The first pulse, called the pump, generates an excited state in the sample. The interaction between this excited state and the second

pulse, called the probe, as a function of wavelength and delay between pulses gives information on the energetics and the time-evolution of the excited state. This technique alone would provide a wealth of information on the photochemical trends observed in this thesis. As a simple example, the lifetime of the excited state could be quantified for each type of nanocrystalline film. If the enhanced photoactivity of the largest bipyramids is primarily a function of harvesting more photons per surface site, then the lifetime of the excited state should not change significantly. On the other hand, if spatial confinement of the electron-hole pair plays a role in recombination as suggested by Cargnello et al [84], then one would expect the lifetime to increase in larger nanocrystals. Additionally, the existence of shape-driven charge-carrier separation would be evident as a difference in the lifetime of the excited state on different nanocrystal morphologies. More subtle effects could also be explored, such as the relative contributions of bulk and surface recombination events. Such a study would lend additional credence to the photochemical trends observed in these nanocrystals and assist efforts to apply the findings of these studies to more complex photocatalytic systems.

Furthermore, this project has demonstrated the potential of thin-films of well-defined nanocrystals as a model catalytic system. This paradigm may be applied to other systems, such as CH_3CHO – TiO_2 or CH_3COOH – TiO_2. Both of these reagents have an even richer range of chemical and photochemical pathways on TiO_2 [29, 56] than methanol, including C-C bond formation reactions (aldol reaction for CH_3CHO and bimolecular ketonization for CH_3COOH) which are of interest to both academia and industry.

References

[1] C.H. Bartholomew, R.J. Farrauto, Fundamentals of Industrial Catalysis Processes, 2 ed., Wiley - Interscience, Hoboken, NJ, 2006.

[2] Recognizing the Best in Innovation: Breakthrough Catalyst, in: R&D Magazine, 2005.

[3] J.M. Vohs, Chem. Rev., 113 (2013) 4136-4163.

[4] M.R. Hoffmann, S.T. Martin, W.Y. Choi, D.W. Bahnemann, Chem. Rev., 95 (1995) 69-96.

[5] G. Ertl, M. Weiss, S.B. Lee, Chem. Phys. Lett., 60 (1979) 391-394.

[6] K.S. Kim, M.A. Barteau, Surf. Sci., 223 (1989) 13-32.

[7] K.J.J. Mayrhofer, M. Arenz, B.B. Blizanac, V. Stamenkovic, P.N. Ross, N.M. Markovic, Electrochim. Acta, 50 (2005) 5144-5154.

[8] U. Diebold, Surf. Sci. Rep., 48 (2003) 53-229.

[9] M.A. Henderson, Surf. Sci. Rep., 66 (2011) 185-297.

[10] T. Feng, J.M. Vohs, J. Catal., 208 (2002) 301-309.

[11] A.L. Linsebigler, G.Q. Lu, J.T. Yates, Chem. Rev., 95 (1995) 735-758.

[12] D.A.H. Hanaor, C.C. Sorrell, J Mater Sci, 46 (2011) 855-874.

[13] H. Perron, C. Domain, J. Roques, R. Drot, E. Simoni, H. Catalette, Theor. Chem. Acc., 117 (2007) 565-574.

[14] V.S. Lusvardi, M.A. Barteau, W.E. Farneth, J. Catal., 153 (1995) 41-53.

[15] N.A. Deskins, M. Dupuis, J. Phys. Chem. C, 113 (2009) 346-358.

[16] N.A. Deskins, M. Dupuis, Phys. Rev. B, 75 (2007).

[17] P.C. Angelome, L. Andrini, M.E. Calvo, F.G. Requejo, S.A. Bilmes, G.J.A.A. Soler-Illia, J. Phys. Chem. C, 111 (2007) 10886-10893.

[18] M. Inagaki, R. Nonaka, B. Tryba, A.W. Morawski, Chemosphere, 64 (2006) 437-445.

[19] J. Augustynski, Electrochim. Acta, 38 (1993) 43-46.

[20] M.A. Barteau, Chem. Rev., 96 (1996) 1413-1430.

[21] Q.Q. Hao, Z.Q. Wang, X.C. Mao, C.Y. Zhou, D.X. Dai, X.M. Yang, Chinese J Chem Phys, 29 (2016) 105-111.

[22] R.F. Strickland-Constable, Kinetics and Mechanism of Crystallization, Academic Press, 1968.

[23] R. Patel, Q. Guo, I. Cocks, E.M. Williams, E. Roman, J.L. deSegovia, J Vac Sci Technol A, 15 (1997) 2553-2556.

[24] M. Li, W. Hebenstreit, U. Diebold, Phys. Rev. B, 61 (2000) 4926-4933.

[25] M. Li, W. Hebenstreit, L. Gross, U. Diebold, M.A. Henderson, D.R. Jennison, P.A. Schultz, M.P. Sears, Surf. Sci., 437 (1999) 173-190.

[26] M. Lazzeri, A. Vittadini, A. Selloni, Phys. Rev. B, 63 (2001).

[27] G.S. Herman, Z. Dohnalek, N. Ruzycki, U. Diebold, J. Phys. Chem. B, 107 (2003) 2788-2795.

[28] L.E. Firment, Surf. Sci., 116 (1982) 205-216.

[29] K.S. Kim, M.A. Barteau, J. Catal., 125 (1990) 353-375.

[30] G.S. Herman, M.R. Sievers, Y. Gao, Phys. Rev. Lett., 84 (2000) 3354-3357.

[31] R.E. Tanner, Y. Liang, E.I. Altman, Surf. Sci., 506 (2002) 251-271.

[32] R. Hengerer, B. Bolliger, M. Erbudak, M. Gratzel, Surf. Sci., 460 (2000) 162-169.

[33] Y. Liang, S.P. Gan, S.A. Chambers, E.I. Altman, Phys. Rev. B, 63 (2001).

[34] M. Lazzeri, A. Selloni, Phys. Rev. Lett., 87 (2001).

[35] M.A. Henderson, S. Otero-Tapia, M.E. Castro, Faraday Discuss., 114 (1999) 313-329.

[36] M.A. Henderson, S. Otero-Tapia, M.E. Castro, Surf. Sci., 412-13 (1998) 252-272.

[37] A. Sasahara, T.C. Droubay, S.A. Chambers, H. Uetsuka, H. Onishi, Nanotechnology, 16 (2005) S18-S21.

[38] A. Sasahara, H. Uetsuka, H. Onishi, J. Phys. Chem. B, 105 (2001) 1-4.

[39] I.D. Cocks, Q. Guo, R. Patel, E.M. Williams, E. Roman, J.L. deSegovia, Surf. Sci., 377 (1997) 135-139.

[40] A. Gutierrez-Sosa, P. Martinez-Escolano, H. Raza, R. Lindsay, P.L. Wincott, G. Thornton, Surf. Sci., 471 (2001) 163-169.

[41] J.R. McManus, E. Martono, J.M. Vohs, Catal. Today, 237 (2014) 157-165.

[42] W. Chen, Q. Kuang, Q.X. Wang, Z.X. Xie, Rsc Adv, 5 (2015) 20396-20409.

[43] K.S. Kim, M.A. Barteau, W.E. Farneth, Langmuir, 4 (1988) 533-543.

[44] H. Onishi, Y. Yamaguchi, K. Fukui, Y. Iwasawa, J. Phys. Chem., 100 (1996) 9582-9584.

[45] K.S. Kim, M.A. Barteau, J. Mol. Catal., 63 (1990) 103-117.

[46] K.S. Kim, M.A. Barteau, Langmuir, 6 (1990) 1485-1488.

[47] F. Gonzalez, G. Munuera, J.A. Prieto, J Chem Soc Farad T 1, 74 (1978) 1517-1529.

[48] T.N. Pham, T. Sooknoi, S.P. Crossley, D.E. Resasco, ACS Catal., 3 (2013) 2456-2473.

[49] D.C. Grinter, M. Nicotra, G. Thornton, J. Phys. Chem. C, 116 (2012) 11643-11651.

[50] R.E. Tanner, A. Sasahara, Y. Liang, E.I. Altman, H. Onishi, J. Phys. Chem. B, 106 (2002) 8211-8222.

[51] F. Xiong, Y.Y. Yu, Z.F. Wu, G.H. Sun, L.B. Ding, Y.K. Jin, X.Q. Gong, W.X. Huang, Angew. Chem. Int. Ed., 55 (2016) 623-628.

[52] V.S. Lusvardi, M.A. Barteau, W.R. Dolinger, W.E. Farneth, J. Phys. Chem., 100 (1996) 18183-18191.

[53] K.S. Kim, M.A. Barteau, Langmuir, 4 (1988) 945-953.

[54] S.C. Luo, J.L. Falconer, J. Catal., 185 (1999) 393-407.

[55] S.C. Luo, J.L. Falconer, Catal. Lett., 57 (1999) 89-93.

[56] H. Idriss, K.S. Kim, M.A. Barteau, J. Catal., 139 (1993) 119-133.

[57] H. Idriss, K.S. Kim, M.A. Barteau, Surf. Sci., 262 (1992) 113-127.

[58] T. Ohsawa, I.V. Lyubinetsky, M.A. Henderson, S.A. Chambers, J. Phys. Chem. C, 112 (2008) 20050-20056.

[59] C.M. Friend, Chem. Rec., 14 (2014) 944-951.

[60] N.Q. Wu, J. Wang, D. Tafen, H. Wang, J.G. Zheng, J.P. Lewis, X.G. Liu, S.S. Leonard, A. Manivannan, J. Am. Chem. Soc., 132 (2010) 6679-6685.

[61] P. Salvador, J. Phys. Chem. C, 111 (2007) 17038-17043.

[62] M. D'Arienzo, J. Carbajo, A. Bahamonde, M. Crippa, S. Polizzi, R. Scotti, L. Wahba, F. Morazzoni, J. Am. Chem. Soc., 133 (2011) 17652-17661.

[63] A. Valdes, Z.W. Qu, G.J. Kroes, J. Rossmeisl, J.K. Norskov, J. Phys. Chem. C, 112 (2008) 9872-9879.

[64] X. Li, J.G. Yu, J.X. Low, Y.P. Fang, J. Xiao, X.B. Chen, J Mater Chem A, 3 (2015) 2485-2534.

[65] M.M. Shen, M.A. Henderson, J. Phys. Chem. Lett., 2 (2011) 2707-2710.

[66] A. Migani, D.J. Mowbray, A. Iacomino, J. Zhao, H. Petek, A. Rubio, J. Am. Chem. Soc., 135 (2013) 11429-11432.

[67] M. Shen, D.P. Acharya, Z. Dohnalek, M.A. Henderson, J. Phys. Chem. C, 116 (2012) 25465-25469.

[68] M.M. Shen, M.A. Henderson, J. Phys. Chem. C, 116 (2012) 18788-18795.

[69] Q. Guo, C.B. Xu, Z.F. Ren, W.S. Yang, Z.B. Ma, D.X. Dai, H.J. Fan, T.K. Minton, X.M. Yang, J. Am. Chem. Soc., 134 (2012) 13366-13373.

[70] Q. Guo, C.B. Xu, W.S. Yang, Z.F. Ren, Z.B. Ma, D.X. Dai, T.K. Minton, X.M. Yang, J. Phys. Chem. C, 117 (2013) 5293-5300.

[71] X.C. Mao, Z.Q. Wang, X.F. Lang, Q.Q. Hao, B. Wen, D.X. Dai, C.Y. Zhou, L.M. Liu, X.M. Yang, J. Phys. Chem. C, 119 (2015) 6121-6127.

[72] C.B. Xu, W.S. Yang, Q. Guo, D.X. Dai, M.D. Chen, X.M. Yang, J. Am. Chem. Soc., 135 (2013) 10206-10209.

[73] C.B. Xu, W.S. Yang, Z.F. Ren, D.X. Dai, Q. Guo, T.K. Minton, X.M. Yang, J. Am. Chem. Soc., 135 (2013) 19039-19045.

[74] C.Y. Zhou, Z.F. Ren, S.J. Tan, Z.B. Ma, X.C. Mao, D.X. Dai, H.J. Fan, X.M. Yang, J. LaRue, R. Cooper, A.M. Wodtke, Z. Wang, Z.Y. Li, B. Wang, J.L. Yang, J.G. Hou, Chem Sci, 1 (2010) 575-580.

[75] Q. Yuan, Z.F. Wu, Y.K. Jin, L.S. Xu, F. Xiong, Y.S. Ma, W.X. Huang, J. Am. Chem. Soc., 135 (2013) 5212-5219.

[76] C.B. Xu, W.S. Yang, Q. Guo, D.X. Dai, M.D. Chen, X.M. Yang, J. Am. Chem. Soc., 136 (2014) 602-605.

[77] O.I. Micic, Y.N. Zhang, K.R. Cromack, A.D. Trifunac, M.C. Thurnauer, J. Phys. Chem., 97 (1993) 13284-13288.

[78] K.R. Phillips, S.C. Jensen, M. Baron, S.C. Li, C.M. Friend, J. Am. Chem. Soc., 135 (2013) 574-577.

[79] A. Kafizas, X.L. Wang, S.R. Pendlebury, P. Barnes, M. Ling, C. Sotelo-Vazquez, R. Quesada-Cabrera, C. Li, I.P. Parkin, J.R. Durrantt, J. Phys. Chem. A, 120 (2016) 715-723.

[80] Y. Ma, X.L. Wang, C. Li, Chinese J Catal, 36 (2015) 1519-1527.

[81] N. Murakami, Y. Kurihara, T. Tsubota, T. Ohno, J. Phys. Chem. C, 113 (2009) 3062-3069.

[82] T. Ohno, K. Sarukawa, M. Matsumura, New J. Chem., 26 (2002) 1167-1170.

[83] C. Liu, X.G. Han, S.F. Xie, Q. Kuang, X. Wang, M.S. Jin, Z.X. Xie, L.S. Zheng, Chem-Asian J, 8 (2013) 282-289.

[84] M. Cargnello, T. Montini, S.Y. Smolin, J.B. Priebe, J.J.D. Jaen, V.V.T. Doan-Nguyen, I.S. McKay, J.A. Schwalbe, M.M. Pohl, T.R. Gordon, Y.P. Lu, J.B. Baxter,

A. Bruckner, P. Fornasiero, C.B. Murray, P Natl Acad Sci USA, 113 (2016) 3966-3971.

[85] H.Z. Zhang, B. Chen, J.F. Banfield, PCCP, 11 (2009) 2553-2558.

[86] J.F. O'Hanlon, A User's Guide to Vacuum Technology, 2 ed., Wiley-Interscience, New York, 1989.

[87] T.R. Gordon, M. Cargnello, T. Paik, F. Mangolini, R.T. Weber, P. Fornasiero, C.B. Murray, J. Am. Chem. Soc., 134 (2012) 6751-6761.

[88] N. Auparay, Room Temperature Seebeck Coefficient Measurement of Metals and Semiconductors, in: Physics, Oregon State University, 2013.

[89] Yield Strength - Strength (Mechanics) of Materials, in, Engineers Edge, 2016.

[90] G. Attard, C. Barnes, Surfaces, Oxford University Press, 1998.

[91] S.J. Garrett, Temperature Programmed Desorption, in, 1997.

[92] E.I. Ko, J.B. Benziger, R.J. Madix, J. Catal., 62 (1980) 264-274.

[93] A. Savitzky, M.J.E. Golay, Anal. Chem., 36 (1964) 1627-&.

[94] Operating Manual and Programming Reference, Models RGA100, RGA200, and RGA300 Residual Gas Analyzer, Stanford Research Systems, Sunnyvale, CA, 2009.

[95] C.D. Wagner, W.M. Riggs, L.E. Davis, J.F. Moulder, Handbook of X-ray Photoelectron Spectroscopy, Perkin-Elmer Corporation, Eden Prairie, MN.

[96] Peak Fitting in XPS, in, CasaXPS, 2006.

[97] R. Smart, S. McIntyre, M. Bancroft, I. Bello, X-ray Photoelectron Spectroscopy, in, Molecular Materials Research Center, Beckman Institute, Caltech.

[98] M.A. Barteau, J. Vac. Sci. Technol., A, 11 (1993) 2162-2168.

[99] H. Idriss, M.A. Barteau, Adv. Catal., 45 (2000) 261-331.

[100] M.A. Barteau, J.E. Lyons, I.K. Song, J. Catal., 216 (2003) 236-245.

[101] G. Centi, R. Passalacqua, S. Perathoner, D.S. Su, G. Weinberg, R. Schlogl, PCCP, 9 (2007) 4930-4938.

[102] G. Centi, S. Perathoner, Coord. Chem. Rev., 255 (2011) 1480-1498.

[103] T. Ressler, B.L. Kniep, I. Kasatkin, R. Schlogl, Angew. Chem. Int. Ed., 44 (2005) 4704-4707.

[104] H.X. Mai, L.D. Sun, Y.W. Zhang, R. Si, W. Feng, H.P. Zhang, H.C. Liu, C.H. Yan, J. Phys. Chem. B, 109 (2005) 24380-24385.

[105] S.R. Zhang, L. Nguyen, Y. Zhu, S.H. Zhan, C.K. Tsung, F. Tao, Acc. Chem. Res., 46 (2013) 1731-1739.

[106] H.J. Freund, N. Ernst, T. Risse, H. Hamann, G. Rupprechter, Phys. Status Solidi A, 187 (2001) 257-274.

[107] A.K.P. Mann, Z.L. Wu, F.C. Calaza, S.H. Overbury, ACS Catal., 4 (2014) 2437-2448.

[108] S. Agarwal, L. Lefferts, B.L. Mojet, Chemcatchem, 5 (2013) 479-489.

[109] A. Selloni, Nat. Mater., 7 (2008) 613-615.

[110] K.L. Lv, B. Cheng, J.G. Yu, G. Liu, PCCP, 14 (2012) 5349-5362.

[111] M.C. Biesinger, L.W.M. Lau, A.R. Gerson, R.S.C. Smart, Appl. Surf. Sci., 257 (2010) 887-898.

[112] R.L. Kurtz, Surf. Sci., 177 (1986) 526-552.

[113] E.-H. Kong, J. Lim, J.H. Lee, W. Choi, H.M. Jang, Appl. Catal., B, 176 (2015) 76-82.

[114] A.Y. Ahmed, T.A. Kandiel, I. Ivanova, D. Bahnemann, Appl. Surf. Sci., 319 (2014) 44-49.

[115] D.A. Bennett, M. Cargnello, T.R. Gordon, C.B. Murray, J.M. Vohs, PCCP, 17 (2015) 17190-17201.

[116] U. Diebold, N. Ruzycki, G.S. Herman, A. Selloni, Catal. Today, 85 (2003) 93-100.

[117] M.V. Ganduglia-Pirovano, A. Hofmann, J. Sauer, Surf. Sci. Rep., 62 (2007) 219-270.

[118] J. Pan, G. Liu, G.M. Lu, H.M. Cheng, Angew. Chem. Int. Ed., 50 (2011) 2133-2137.

[119] K. Bakhmutsky, N.L. Wieder, M. Cargnello, B. Galloway, P. Fornasiero, R.J. Gorte, Chemsuschem, 5 (2012) 140-148.

[120] J.S. Kim, N.L. Wieder, A.J. Abraham, M. Cargnello, P. Fornasiero, R.J. Gorte, J.M. Vohs, J. Electrochem. Soc., 158 (2011) B596-B600.

[121] L. De Rogatis, M. Cargnello, V. Gombac, B. Lorenzut, T. Montini, P. Fornasiero, Chemsuschem, 3 (2010) 24-42.

[122] C.M.Y. Yeung, K.M.K. Yu, Q.J. Fu, D. Thompsett, M.I. Petch, S.C. Tsang, J. Am. Chem. Soc., 127 (2005) 18010-18011.

[123] K. Tedsree, T. Li, S. Jones, C.W.A. Chan, K.M.K. Yu, P.A.J. Bagot, E.A. Marquis, G.D.W. Smith, S.C.E. Tsang, Nat Nanotechnol, 6 (2011) 302-307.

[124] S.H. Joo, J.Y. Park, C.K. Tsung, Y. Yamada, P.D. Yang, G.A. Somorjai, Nat. Mater., 8 (2009) 126-131.

[125] J.N. Park, A.J. Forman, W. Tang, J.H. Cheng, Y.S. Hu, H.F. Lin, E.W. McFarland, Small, 4 (2008) 1694-1697.

[126] P.M. Arnal, M. Comotti, F. Schuth, Angew. Chem. Int. Ed., 45 (2006) 8224-8227.

[127] M. Cargnello, J.J.D. Jaen, J.C.H. Garrido, K. Bakhmutsky, T. Montini, J.J.C. Gamez, R.J. Gorte, P. Fornasiero, Science, 337 (2012) 713-717.

[128] M. Cargnello, N.L. Wieder, T. Montini, R.J. Gorte, P. Fornasiero, J. Am. Chem. Soc., 132 (2010) 1402-1409.

[129] N.L. Wieder, M. Cargnello, K. Bakhmutsky, T. Montini, P. Fornasiero, R.J. Gorte, J. Phys. Chem. C, 115 (2011) 915-919.

[130] K. Yoon, Y. Yang, P. Lu, D.H. Wan, H.C. Peng, K.S. Masias, P.T. Fanson, C.T. Campbell, Y.N. Xia, Angew. Chem. Int. Ed., 51 (2012) 9543-9546.

[131] M. Cargnello, T. Montini, S. Polizzi, N.L. Wieder, R.J. Gorte, M. Graziani, P. Fornasiero, Dalton T, 39 (2010) 2122-2127.

[132] A. Fujimori, Phys. Rev. B, 27 (1983) 3992-4001.

[133] G. Zhou, J. Hanson, R.J. Gorte, Appl Catal a-Gen, 335 (2008) 153-158.

[134] G. Zhou, P.R. Shah, T. Montini, P. Fornasiero, R.J. Gorte, Surf. Sci., 601 (2007) 2512-2519.

[135] G. Zhou, P.R. Shah, T. Kim, P. Fornasiero, R.J. Gorte, Catal. Today, 123 (2007) 86-93.

[136] X.C. Guo, J.T. Yates, J. Chem. Phys., 90 (1989) 6761-6766.

[137] E. Rocchini, A. Trovarelli, J. Llorca, G.W. Graham, W.H. Weber, M. Maciejewski, A. Baiker, J. Catal., 194 (2000) 461-478.

[138] T.S. Zhang, J. Ma, Y.Z. Chen, L.H. Luo, L.B. Kong, S.H. Chan, Solid State Ionics, 177 (2006) 1227-1235.

[139] M. Lankin, Y.H. Du, C. Finnerty, J Fuel Cell Sci Tech, 8 (2011).

[140] A. Hauch, S.H. Jensen, J.B. Bilde-Sorensen, M. Mogensen, J. Electrochem. Soc., 154 (2007) A619-A626.